PATTERNED QUANTUM DOT AND INVERSE QUANTUM DOT ACTIVE LAYERS FOR OPTOELECTRONICS APPLICATIONS

BY

VARUN BOEHM VERMA

DISSERTATION

Submitted in partial fulfillment of the requirements
for the degree of Doctor of Philosophy in Electrical and Computer Engineering
in the Graduate College of the
University of Illinois at Urbana-Champaign, 2009

Urbana, Illinois

Doctoral Committee:

Professor James J. Coleman, Chair
Professor Kent Choquette
Professor Shun-Lien Chuang
Assistant Professor Xiuling Li
Assistant Professor Lynford Goddard

ABSTRACT

The use of semiconductor quantum dots (QDs) in photonic devices has become widespread in recent years and QDs themselves have received a considerable amount of attention from the photonics community. Not only do they offer many potential advantages in lasers, but they have also become interesting from an applied physics perspective as tools for exploring strong coupling in nanoscale cavities, as single photon emitters, and possibly as elements of quantum information circuits. To a great extent many of the promises made about the advantages QDs would bring to photonic devices remain unfulfilled, largely due to the size inhomogeneity and random placement inherent with the self-assembled growth technique. The work in this document demonstrates that it is possible to create patterned QDs with precisely engineered properties such as diameter, thickness, material composition, position, and emission wavelength, while simultaneously maintaining the high optical quality of the material necessary for incorporation into optoelectronic devices. These QDs are fabricated using electron beam lithography combined with wet-etching and regrowth techniques.

We also present a detailed theoretical analysis of a novel structure which can only be formed by patterning techniques known as the nanopore or inverse quantum dot structure. This structure is the electronic analogue of a photonic crystal. We show that the perturbation of an ordinary quantum well by a periodic two-dimensional lattice of energy barriers leads to the introduction of intraband energy gaps. The predicted results show excellent agreement with experimental data obtained from devices fabricated by selective area epitaxy. In addition, we have explored the use of the wet-etching technique for the fabrication of this nanostructure. The wet-etching technique is shown to provide a higher degree of flexibility and repeatability than the selective area epitaxy process. The experimental results suggest a significant reduction in

intersubband scattering rates resulting in a drastic modification of the interband optical properties, which may be useful for the utilization of the nanopore structure in intersubband devices. This observation is supported by analytical calculations of the electron-phonon scattering rates in the nanopore structure.

To Vinny

ACKNOWLEDGMENTS

The work outlined in this document would not have been possible without the support of numerous individuals, in particular my adviser Jim Coleman, who provided me with the opportunity to learn about so many different aspects of this field as well as the freedom to pursue many of my own research interests.

I am also indebted to Tonia Siuts, our secretary who was very patient with the never-ending list of chemicals, wafers, etc., that needed to be ordered on a daily basis and that I needed to keep my research going.

There are also the numerous grad students from this group who influenced me greatly in my first few years, namely Kirk Price and Victor Elarde. My research was built on the hard work and foundation left by those who were here before me. I would also like to thank those students who joined the group towards the end of my work including Uttam Reddy, Neville Dias, Jonathan Young and Akash Garg.

Finally, thanks to my parents who encouraged me to never stop learning and to my brothers for their support.

TABLE OF CONTENTS

CHAPTER 1 – INTRODUCTION 1
1.1 Self-Assembled QDs 3
1.2 Patterned QDs 4
1.3 Selective Area Epitaxy by MOCVD 5

CHAPTER 2 – QUANTUM DOTS FABRICATED BY WET ETCHING 7
2.1 Substrate Preparation for Electron Beam Lithography 7
2.1.1 Epitaxial growth of base structure 7
2.1.2 Sample preparation for electron beam lithography 8
2.2 QD Patterning 9
2.2.1 Hydrogen silsesquioxane (HSQ) process 10
2.2.2 Polymethylmethacrylate (PMMA) process 11
2.3 Wet Etching of Patterned QDs 12
2.4 Processing Steps for Photoluminescence Characterization 14
2.5 Photoluminescence Results 15
2.6 Wet-Etched Patterned QD Laser Fabrication 17
2.7 Figures 21

CHAPTER 3 –THE PATTERNED QUANTUM DOT MOLECULE LASER 24
3.1 Device Processing 25
3.2 Simulation 27
3.3 Characterization and Results 31
3.4 Figures 33

CHAPTER 4 – ANALYSIS OF THE NANOPORE ACTIVE LAYER 38
4.1 Derivation of Analytical Model 39
4.1.1 The general approach 39
4.1.2 Detailed mathematical solution 42
4.2 Simulation Results 47
4.2.1 Bandstructure 47
4.2.2 Density of states 47
4.2.3 Selection rules 48
4.2.4 Gain spectrum 49
4.3 Comparing Analysis with Experiment 50
4.4 Valence Band Mixing Model 54
4.4.1 The Pikus-Bir Hamiltonian 54
4.4.2 Mathematical methods 57
4.5 Intersubband Transitions 70
4.5.1 Intersubband physics in a nanopore array 71
4.5.2 Polarization dependence of intersubband absorption 76
4.5.3 Sum rule 77
4.5.4 Conclusion 81
4.5.5 Numerical expressions 83
4.6 Parametric Analysis and Optimization of the Nanopore Active Layer 85

4.6.1 Unit cell geometry....85
4.6.2 Lattice pitch and nanopore diameter....86
4.6.3 Material system parameters....89
4.6.4 Temperature effects....92
4.7 Carrier Scattering Mechanisms....93
4.7.1 Review of scattering in a quantum well....95
4.7.2 Polar LO phonon scattering....98
4.7.3 Acoustic phonon scattering....101
4.8 Broadening....103
4.9 Table and Figures....106

CHAPTER 5 – NANOPORE LASERS FABRICATED BY WET ETCHING....132
5.1 Fabrication....133
5.1.1 Base structure growth....133
5.1.2 Quantum well patterning....133
5.1.3 Regrowth and laser processing....135
5.2 Characterization and Results....137
5.3 Figures....142

CHAPTER 6 – CONCLUSION....150

APPENDIX A – CODE LISTING FOR NANOPORE ANALYSIS....152

REFERENCES....174

CHAPTER 1 – INTRODUCTION

Self-assembled quantum dots (QDs) have received considerable attention over the past 20 years as the active elements in photonic devices. Much of this interest is the result of their many predicted benefits such as low threshold current density, narrow gain bandwidth, and increased characteristic temperature [1]. Unfortunately, many of these benefits proved elusive to the photonics community primarily due to the inhomogeneous broadening resulting from the large variation in QD size in typical self-assembled QD arrays. In addition to applications in lasers, QDs are also beginning to find applications in the applied physics community as efficient single photon generators and as the fundamental components of experiments in cavity quantum electrodynamics (QED). This area of research typically requires the patterning of a photonic crystal nanocavity around a single QD, which has proven difficult with self-assembled QDs due to poor control of their position and density.

The work presented in this document can be divided roughly into two parts. The first is primarily experimental in nature and describes a new fabrication process for creating patterned QDs and QD lasers. This technique differs from the previous work that was performed in this group on QDs patterned using selective area epitaxy in that it is a top-down rather than a bottom-up approach to fabrication, and has certain advantages which will be discussed in Chapters 2 and 3. Although QDs fabricated by the selective area growth technique allowed for the definition of the position and size of a high-density array of QDs, those QDs were limited to large sizes of greater than 80 nm and the emission wavelengths were unpredictable due to growth enhancement effects. For cavity-QED experiments and future applications in quantum information systems, it is desirable

to be able to accurately predict the QD emission wavelength, as well as to have a QD small enough that it behaves like an atomic system. The objective of this work was to design a QD fabrication process which allows the definition of the size and position of individual quantum dots with predictable emission wavelengths, with QD sizes below about 50 nm. The primary application of this technology would be the ability to pattern individual QDs inside of nanoscale cavities for cavity-QED experiments as well as future quantum information systems. QDs fabricated in this way could also potentially be used in VCSELs or even edge-emitting lasers. Photoluminescence results will be presented in Chapter 2. The successful use of two layers of patterned QDs in an edge-emitting laser will be presented in Chapter 3, which demonstrates that a process has been successfully developed which achieves the goals put forth above.

The second part of the document is primarily analytical in nature, and focuses on the theory and characterization of a novel device which has been called a nanopore or inverse quantum dot laser [2]. Chapter 4 describes a detailed analytical model that has been developed for this structure, which shows excellent agreement with experimental results. The nanopore laser is unique in the sense that it has QD-like properties, which is desirable for achieving a low-threshold laser with high differential quantum efficiency, while at the same time providing a larger gain volume and lower sensitivity to process variations than patterned QDs. After comparing analysis with experiment, a method will be presented for enhancing the QD-like properties of the nanopore laser and suppressing the quantum well-like properties. The physics of intersubband transitions and possible applications will also be discussed, along with an analysis of intersubband scattering rates. Chapter 5 covers the application of the wet-etching technique to nanopore laser

fabrication. The details of the fabrication process will be given, as well as the experimental results and a comparison with theoretical analyses.

1.1 Self-Assembled QDs

There are three modes of heteroepitaxial crystal growth: Frank van der Merwe, Volmer-Weber, and Stranski-Krastanow. These three names are used to reference layer-by-layer, island, and layer-by-layer plus island growth, respectively. The growth mode for a given system depends on the lattice mismatch and the interface energies of the system. In a lattice matched system, the growth mode is determined by the surface energies. If the sum of the epilayer surface energy and the interface energy is lower than the substrate surface energy, Frank van der Merwe or layer-by-layer growth will result. A change in the sum of the epilayer and interface energies may drive a system into the Volmer-Weber or island growth mode. Finally, for a strained system initial growth may occur layer-by-layer, but at some critical thickness the large strain energy of the system can be reduced by forming isolated islands in which the strain is relaxed. The result is coherently strained three-dimensional islands which are referred to as self-assembled quantum dots (QDs) when embedded in a barrier material. The term *self-assembled* refers to the fact that these QDs form with no external influences other than the strain energy of the system. The term has also come to signify a disordered system in which the QDs form in random positions and with a random size distribution.

Initial studies of self-assembled QDs were performed in the InAs/GaAs material system [3-6]. These QDs were grown by MBE, typically at temperatures ranging between 480 ºC and 530 ºC. Formation of the QDs was found to occur above some critical layer thickness d_c, and typically took place on top of a thin layer of InAs called the wetting

layer which is significantly thinner than the QDs. The formation of self-assembled QDs was also found to occur using metalorganic chemical vapor deposition (MOCVD). Initial experiments were performed at 450 ºC [7-11]. No QD formation was found below 33% indium composition. For higher indium concentrations the 2D-3D transition was found to occur at smaller critical thicknesses. MOCVD QDs can now be grown defect-free, with typical densities of 10^{10}-10^{11} cm^{-2}. Linewidths typically range between 50 and 80 meV, although recent improvement in growth techniques has yielded linewidths as small as 20 meV [12-15].

1.2 Patterned QDs

Numerous fabrication techniques have been explored in order to fully realize the potential advantages offered by QDs by controlling the size and position of each QD in an array. These techniques include MOCVD or MBE regrowth using a patterned SiO_2 growth inhibition mask [16, 17], pre-patterning of InGaAs thin films [18, 19], growth in inverted pyramid shaped recesses [20], the preparation of preferential growth facets via selective area epitaxy [21, 22], manipulation of the local crystal plane step edge density [23, 24], and etching of an existing quantum well or multiple quantum well structure [25-30]. Two techniques — selective area regrowth and, more recently, wet etching — have been used to make a functional laser device [31, 32].

There are advantages as well as disadvantages to each of these techniques, and at the present time there is no “best” method for creating patterned QDs. To a large extent the best method depends on the particular application. Many of the methods mentioned above such as MOCVD regrowth using a growth inhibition mask, and etching of an existing quantum well or multiple quantum well structure, rely on electron beam

lithography for the definition of each individual QD. This process can be prohibitively expensive, especially for applications requiring a large array of QDs such as edge-emitting lasers. However, the fact that these techniques have been used successfully to make lasers proves that they can be used to make high-density and high optical quality arrays of QDs for applications in optoelectronics. Other techniques such as growth in inverted pyramid shaped recesses have the advantage of significantly reduced cost due to the use of standard photolithography techniques, but at the cost of reduced QD density which is necessary in order to make a functional laser device.

1.3 Selective Area Epitaxy by MOCVD

Selective area epitaxy by MOCVD is a process which utilizes a patterned growth inhibition mask, typically silicon nitride or silicon dioxide, in order to selectively grow crystalline material in well-defined areas of a substrate. Growth occurs in the unmasked regions, and is typically accompanied by an enhancement in film thickness near the edges of the mask due to lateral diffusion of precursor molecules. Ternary and quaternary compounds will also experience a composition enhancement due to the different molecular weights and diffusion constants of the precursor molecules. In the case of $In_xGa_{1-x}As$, an enhancement in indium composition will occur.

Selective area epitaxy has been used extensively in the fabrication of laser devices with integrated passive waveguide components for photonic integrated circuits [33-37]. More recently, it has been used for the fabrication of patterned semiconductor nanostructures such as QDs and inverse quantum dots [2, 31, 38]. Selective area epitaxy for the fabrication of nanostructures has the advantage of maintaining high optical quality of the regrown semiconductor material. Other methods of creating nanostructures which

rely on patterning, such as dry etching, have been shown to result in high nonradiative recombination rates due to surface-induced etch damage. However, the selective area epitaxy method has the disadvantages of growth enhancement as well as indium enhancement. In a large array of patterned QDs, for instance, the thickness and indium content of each QD will vary across the array. Since the thickness of the QD is much smaller than the lateral QD dimensions, even small changes in the relative thickness of each QD can result in a large variation in emission energy. The emission energy of each QD is also highly sensitive to the indium content. Thus any advantages gained from patterning to achieve a higher degree of uniformity in QD lateral dimensions may be counteracted by the deleterious effects mentioned above. These disadvantages motivated the work which will be covered in this thesis in Chapters 2, 3, and 5. Selective area epitaxy was also used in the fabrication of the nanopore laser discussed in Chapter 4. Growth enhancement and indium enhancement will be important in explaining the observed spectral behavior of the nanopore laser device.

CHAPTER 2 – QUANTUM DOTS FABRICATED BY WET ETCHING

As discussed in Chapter 1, QDs have many potential advantages when incorporated into photonic devices. However, many of these advantages remain unrealized due to the difficulty in controlling the properties of individual QDs in a large array, such as their positions and dimensions. In this chapter, we present a wet-etch fabrication process for patterned quantum dots which allows control of individual QD properties. This process differs from previous work performed in this research group primarily in the sense that it is a top-down instead of a bottom-up approach to QD fabrication. As will be discussed in the remainder of the chapter, a top-down approach has a few advantages over a bottom-up approach such as fewer total regrowth steps, as well as a significant improvement in QD compositions and dimensions over large arrays. The improvement in uniformity is the result of elimination of growth enhancement and composition enhancement effects which are unavoidable with selective area epitaxy. The end result is a decrease in inhomogeneous broadening and therefore an increase in peak gain, which is highly desirable for creating low-threshold lasers. The characterization of the QDs will be divided into two sections. The first will discuss the photoluminescence properties of these QDs, and the second will discuss their incorporation into a laser device.

2.1 Substrate Preparation for Electron Beam Lithography

2.1.1 Epitaxial growth of base structure

The base structure consists of all epitaxial layers necessary in order to begin patterning of the QDs. This structure can be used both for QD photoluminescence as well as laser fabrication. The structure is grown on an N+ (100) GaAs substrate, and consists

of a 100 nm Si-doped n+ GaAs buffer layer, 2 μm of Si-doped n-type $Al_{0.75}Ga_{0.25}As$, 100 nm of intrinsic GaAs, an 8.6 nm $In_{0.21}Ga_{0.79}As$ quantum well, and a 2 nm intrinsic GaAs cap as shown in Fig. 2.1. The structure is grown at 800 °C through the $Al_{0.75}Ga_{0.25}As$ layer and a high growth rate is used to reduce carbon incorporation which can compensate the Si dopant. At the beginning of the GaAs lower barrier growth, the temperature is then ramped down to 625 °C for the growth of the $In_{0.21}Ga_{0.79}As$ quantum well and GaAs cap layers.

The $Al_{0.75}Ga_{0.25}As$ lower cladding provides both carrier confinement due to its high bandgap energy relative to that of GaAs, as well as modal confinement due to its lower refractive index relative to GaAs. The top 100 nm of intrinsic GaAs serves as the lower core of the laser structure which efficiently confines carriers close to the quantum well and acts as the central portion of the laser waveguide with highest refractive index. Finally, the $In_{0.21}Ga_{0.79}As$ quantum well, which will eventually be patterned to form QDs, provides the gain for the laser device. The structure is capped with a 2 nm GaAs layer to protect the quantum well from subsequent processing steps as well as to prevent indium segregation at the surface during the cool-down from 625 °C to room temperature.

2.1.2 Sample preparation for electron beam lithography

After growth, the base structure wafer is coated with 50 nm of PECVD SiO_2 and cleaved into 12 mm x 16 mm pieces for further processing. AZ-5214E photoresist is then spun on each sample at 3000 rpm for patterning of the alignment targets, image reversal, and development in AZ-327. After patterning, the samples are placed in an evaporation tool for evaporation of 100 Å Ti which promotes adhesion to the SiO_2, followed by 1500

Å Au. The samples are then placed in acetone to promote liftoff of the metals in regions outside of the alignment targets.

After liftoff, the samples are coated with another 50 nm layer of PECVD SiO_2. Photolithography is performed again in order to define encapsulation regions surrounding the metal alignment targets. AZ-5214E is spun onto the samples at 4500 rpm, then exposed with the encapsulation mark pattern and developed in AZ-327. The underlying 100 nm of PECVD SiO2 is then etched away using a buffered hydrofluoric acid solution for 30 s. The end result of this process is Ti/Au alignment targets which are completely encapsulated in SiO_2, with 50 nm of SiO_2 on top and bottom. The SiO_2 helps to preserve the integrity of the targets during the subsequent regrowth steps and prevents contamination of the sample with gold from the targets. The layout of the alignment targets is shown in Fig. 2.2.

2.2 QD Patterning

The electron beam lithography for this work was done on a JEOL JBX-6000FS series electron beam lithography tool. There were two methods explored for QD patterning. The first method utilized hydrogen silsesquioxane (HSQ), a negative tone electron beam resist, as a wet etch mask. The second method utilized a standard polymethylmethacrylate (PMMA) positive tone electron beam resist followed by the evaporation of a thin titanium layer and subsequent liftoff. Both methods will be described in detail in this section.

2.2.1 Hydrogen silsesquioxane (HSQ) process

HSQ is a negative tone electron beam resist which becomes a SiO_2-like material wherever it is exposed to an electron beam. It has the advantage of a higher ultimate resolution compared to PMMA, at the expense of being more sensitive to environmental factors such as humidity which in turn leads to less reproducible results.

The HSQ patterning process begins with the deposition of 5 nm of PECVD SiO_2. This step was found to be necessary to promote adhesion of the HSQ which does not adhere well to a bare GaAs surface. The sample is then baked at 200 °C for 1 min. After the bakeout, a solution of FOX-14 HSQ diluted 1:5 in MIBK is spun on the sample at 4000 rpm, yielding a 30 nm-thick HSQ layer. This is followed by a second baking step at 90 °C for 1 h in an N_2 ambient oven to remove most of the solvent. After the bake, the sample is loaded immediately into the electron beam lithography tool. As HSQ is extremely sensitive to the presence of oxygen and water vapor, every effort was made to decrease its exposure to the environment after spinning. The HSQ is then patterned in the e-beam system with a triangular array of dots with the doses carefully calibrated to provide the desired QD diameter. After exposure, the sample is immediately developed in 25% TMAH developer for 7 s, followed by a 2 s rinse in DI water and another 5 min rinse under the DI water faucet.

After development, the sample is cleaned in an O_2 plasma for 10 min to ensure complete removal of any remaining HSQ residue on the surface. The HSQ pattern is then transferred into the underlying layer of PECVD oxide with a 17 s etch in a Freon-14 plasma. At this point the sample is ready for wet-etching in order to transfer the dot pattern into the quantum well.

2.2.2 Polymethylmethacrylate (PMMA) process

The PMMA process was developed some time after the HSQ process as a method of avoiding the additional pattern transfer necessary from the HSQ into the underlying oxide adhesion layer. It was also desirable to eliminate the Freon-14 plasma etch as this process step has conclusively been shown to lead to a degradation in material quality and photoluminescence intensity. PMMA also has the advantage of being considerably easier to work with due to its insensitivity to environmental factors. In addition, larger dot diameters can be achieved with PMMA compared to HSQ at significantly lower e-beam doses, resulting in a reduction in total write time and cost.

The PMMA process begins with a 2 min bakeout at 200 °C. The sample is then spin-coated with 2% PMMA diluted in anisole at 4000 rpm, which yields a PMMA layer approximately 60 nm thick. This is followed by a 2 min softbake at 200 °C. The sample is then loaded into the e-beam tool and exposed to the dot pattern with carefully calibrated doses to yield the desired dot sizes.

After exposure, the sample is developed in 1:2 MIBK:IPA for 3 min at a reduced temperature of 10 °C. The development temperature is reduced in order to improve contrast at the expense of reduced sensitivity. Development is followed by a 30 s rinse in IPA, after which the sample is carefully blown dry with N_2.

After development, the sample is immediately loaded into the metal evaporation tool for the evaporation of 100 Å Ti. The sample is then soaked in a solution of 1:1 methylene chloride : methanol for at least 3 h for metal liftoff. The resulting pattern of Ti dots is then ready for wet etching into the quantum well in order to form quantum dots.

2.3 Wet Etching of Patterned QDs

Dry etching would be the ideal method to transfer the dot pattern into the quantum well due to the fact that it is to a large extent an anisotropic process. However, dry etching has been shown to cause significant damage to the substrate and thereby degrade the optical quality of the material. Therefore it is unfortunately incompatible with the top-down approach to QD fabrication. Reluctantly, we are forced to rely on wet etching, which results in far less damage to the semiconductor material at the cost of undercutting resulting from the isotropy of the etch. Undercutting refers to the reduction in lateral feature sizes which occurs when wet etching. To a good approximation, the reduction in QD diameter will be twice the etch depth. Therefore it is important that the initial mask dimensions be significantly larger than the final desired QD size.

It is important to understand the limitations imposed by the initial etch mask pattern on the pitch and size of the final QD arrays after etching. For example, in order to transfer the HSQ or metal dot pattern into the quantum well we must etch a minimum of 10 nm (2 nm GaAs cap plus 8 nm InGaAs QW). This results in a reduction in diameter of about 20 nm of any features on the etch mask after etching into the QW. Thus, in order to obtain a final QD diameter of 30 nm, we must design the dots on the metal or HSQ mask to have a diameter of at least 50 nm. The large dot size necessary on the etch mask in turn limits the pitch and therefore the QD density which can be no smaller than the dot diameter. However, as we will show later, it is possible to obtain arrays of 15-20 nm diameter QDs at pitches as small as 70 nm using this process.

Physically, wet etching proceeds by an oxidation-reduction reaction, and consists of an oxidizing agent and a reducing agent. The oxidizer first oxidizes the semiconductor surface. The resulting semiconductor oxide is then dissolved away by the reducing agent.

As the wet etch is only 10-15 nm deep, the process is extremely delicate, and careful control of the etch chemistry and conditions are required in order to successfully transfer the mask pattern into the quantum well.

Since buffered hydrofluoric acid is later used to strip the HSQ or Ti etch mask, photolithography is performed on the sample to cover the alignment targets with photoresist and protect them during the subsequent etching steps. The etch begins with the removal of the native oxide on the GaAs surface. Although this layer is only ~1 nm thick, it can result in an effect known as micromasking in which a weblike pattern appears on the surface after the etch. There are two common solutions which can be used to etch away the native oxide: dilute sulfuric acid and dilute HCl. For the HSQ process, it was found that the standard solution of 1:1 $HCl:H_2O$ for 15 s caused the HSQ/oxide mask pattern to lose adhesion to the GaAs surface. To avoid this problem with HSQ, a solution of 1:20 $H_2SO_4:H_2O$ for 30 s was used as an alternative to the 1:1 $HCl:H_2O$. For the Ti metal mask, 1:1 $HCl:H_2O$ was used successfully without disturbing the mask pattern.

Immediately after removal of the native oxide, the sample is etched in 50:1 $C_6H_8O_7:H_2O_2$ for approximately 30 s to achieve an etch depth of 15 nm. The sample is slightly overetched by 5 nm in order to assure that the pattern is fully transferred into the quantum well. As small variations in H_2O_2 concentration can have a large impact on etch rate, the etch rate was calibrated using a stripe pattern and profilometer measurement immediately before etching the QD sample. It was found that after etching, spots the size of a few nanometers would appear on the surface in the etched regions of the sample when viewed under an SEM. It was initially believed that these spots were due to areas of the sample which had been oxidized and not reduced by the reducing agent. In order to

remove these dots from the surface, the sample was dipped in H_2O_2 for 15 s in order to completely oxidize the surface, rinsed, and then etched again in 1:1 HCl:H_2O for 15 s to remove this layer of oxide. The resulting surface was found to be pristine after performing these additional steps. Finally, the HSQ/oxide or Ti etch mask is etched for 1 min in buffered hydrofluoric acid. The photoresist protecting the alignment targets is then stripped in acetone and the sample is cleaned with methanol and IPA. The sample is then inspected by SEM to characterize the final QD sizes.

2.4 Processing Steps for Photoluminescence Characterization

The first experiments with the wet-etched QD process were conducted using HSQ as the wet-etch mask. It was desirable to characterize the success or failure of the process before making lasers due to the expense of patterning laser samples using e-beam lithography. In order to do this, small regions of a sample were patterned with QDs which could then be analyzed using photoluminescence measurement techniques.

After transferring the mask pattern into the QW, the subsequent processing steps are relatively straightforward, consisting of one regrowth, a lithography step, and a metallization step. Note that by incorporating the quantum well into the base structure, we have reduced the number of regrowth steps by one compared to the selective area growth method of forming patterned QDs. This is highly desirable due to the possibility of surface contamination or poor interface quality at the regrown surface.

The regrowth consists of a 50 nm GaAs cap layer, a 20 nm $Al_{0.75}Ga_{0.25}As$ diffusion barrier, and a 5 nm GaAs cap. The GaAs cap layer acts as the top potential barrier for the InGaAs quantum dots. During photoluminescence, most of the pump light is absorbed in this layer of the structure, as well as in the lower GaAs layer below the

QDs. The 20 nm $Al_{0.75}Ga_{0.25}As$ diffusion barrier acts as a potential barrier to carriers generated in the GaAs core of the structure, and prevents their diffusion toward the free surface where Fermi level pinning can lead to a high nonradiative recombination rate. The final layer of GaAs prevents the $Al_{0.75}Ga_{0.25}As$ from oxidizing, which could potentially lead to poor metal adhesion in the subsequent evaporation step. The entire regrowth is performed at 600 °C after a 15 s 1:1 $HCl:H_2O$ native oxide removal with no bakeout step in order to prevent thermal reformation of the QDs.

After the regrowth, AZ-5214E photoresist is spun on the sample at 3000 rpm and exposed with an array of 60 µm x 60 µm squares which coincide with the positions of the QD-patterned regions of the sample. After image reversal and development, the sample is loaded into an evaporation tool for evaporation of 100 Å Ti for adhesion and 1500 Å Au. The metal covering the squares is then lifted off in acetone to form apertures over the QD-patterned regions. This metal mask serves both as a method of restricting pump light to the regions of the sample containing QDs, as well as a method of identifying the positions of those regions.

2.5 Photoluminescence Results

Photoluminescence was performed at 77 K using a liquid nitrogen cryostat. The QD-patterned areas of the sample were pumped under CW conditions with the 488 nm line of an Ar-ion laser focused to a spot size of approximately 100 µm. Luminescence from the sample was collected with a 0.5 numerical aperture microscope objective and dispersed using a 1 m monochromator at a resolution of 2 nm. The signal was measured using a liquid nitrogen cooled Ge photodetector and lock-in amplifier.

Measurements were taken from the array of 40 nm diameter QDs shown in Fig. 2.3 at various pump intensities. Figure 2.4 shows the QD spectrum measured at five different pump intensities, as well as the quantum well (QW) spectrum measured at the lowest pump intensity. The QD emission is blueshifted relative to the QW emission by approximately 18 nm or 26 meV at the lowest measured pump power. The blueshift is consistent with an increase in carrier energy due to three-dimensional quantum confinement. Figure 2.5 shows the peak wavelength and full width at half maximum (FWHM) of the QD emission measured at 13 pump powers ranging between 1.1 kW/cm^2 and 4.4 kW/cm^2. A FWHM as small as 24 meV was obtained at the lowest pump power. This result is comparable to the best linewidths achieved to date with self-assembled QDs [12-15]. As the pump power is increased, the peak wavelength blueshifts, which is accompanied by a simultaneous increase in the FWHM of the emission.

To understand the source of the blueshift and broadening with increasing pump power, simulations of the QDs were carried out using the partial function expansion method assuming a perfectly cylindrical QD and a simplified strain model [39-41]. Simulations performed for an 8.6 nm thick, 40 nm diameter $In_{0.21}Ga_{0.79}As$ QD predict ground state emission at 924 nm, or a blueshift relative to the quantum well of 23.4 meV. This number is in good agreement with the experimentally obtained value of 26 meV considering the simplifying assumptions made in the model. From SEM images of the QD array, we estimate a standard deviation in QD diameter of approximately 5 nm. This deviation leads to a shift in the ground state emission energy of only 1.2 meV. From this observation we conclude that the broadening observed with increasing pump power has only a small contribution from size inhomogeneity, which is in contrast to the spectra

obtained from QDs grown by the self-assembly method in which this type of inhomogeneity dominates the observed broadening. For a 40 nm diameter QD, simulations predict six confined states lying between 36 meV and 65 meV above the conduction band edge. Thus, for QDs of this size, we conclude that bandfilling effects are the dominant cause of the broadening observed with increasing pump power.

2.6 Wet-Etched Patterned QD Laser Fabrication

The use of a Freon-RIE etch close to the active layer in the HSQ wet-etched QD process was undesirable but found to be a necessity due to poor adhesion of HSQ to the GaAs surface. It has been shown in previous work that the use of a plasma-based etch can cause significant damage to the material, thereby reducing the efficiency of the radiative recombination process. For the purpose of making lasers, it was highly desirable to reduce nonradiative recombination processes as much as possible in order to ensure lasing. In an effort to circumvent the use of a Freon-RIE etch in the QD fabrication process, a new process was developed utilizing a combination of PMMA e-beam resist followed by evaporation of a thin titanium layer and liftoff in order to define the wet-etch mask pattern. Titanium was found to exhibit excellent adhesion properties to the GaAs surface during the etch, making an underlying PECVD oxide layer unnecessary. The laser fabrication process begins with the procedures outlined in Sections 2.2.2 and 2.3. It should be noted that unlike the selective area growth process in which QW control lasers could be fabricated on the same sample as the QD devices, the wet-etched QD process makes this difficult due to the fact that the QW is being etched everywhere except underneath the Ti metal dot pattern. Although it is possible to pattern a stripe instead of QDs by e-beam, this process would be prohibitively time-consuming and expensive due

to the large area which would need to be written. Therefore an unetched base structure sample was processed in parallel with the QD sample with all regrowth, etching, and photolithography performed in parallel in order to minimize variations between the two samples.

The laser structure used in the wet-etched QD laser process is known as a buried heterostructure laser, and is the same structure used in the QD lasers formed by selective area growth [2]. This structure has proven to be ideal for patterned QDs due to its excellent lateral modal and carrier confinement properties, which compensate for the low gain available from the QD gain medium. The buried heterostructure laser typically consists of a core which is then etched to form a ridge waveguide. After etching, the upper cladding is regrown so that the ridge waveguide is effectively buried under the cladding material. The fact that the core material has a higher refractive index and lower bandgap than the cladding material results in the aforementioned modal and carrier confinement properties of the structure.

After transferring the QD pattern to the QW, the processing proceeds with the regrowth of the upper core of the laser. After a 1:1 $HCl:H_2O$ native oxide removal for 15 s, the sample is loaded into the MOCVD reactor for regrowth. The temperature is ramped to 600 ºC and the growth started immediately with no bakeout step in order to minimize thermal reformation of the QDs. After the growth of 90 nm of GaAs, the sample is then removed from the reactor for further processing.

Photolithography is then performed on the sample in order to form 4 μm wide ridge waveguides. The mask pattern consists of 20 μm stripes with 4 μm gaps. The photolithography is performed so as to open windows in the 20 μm stripes which will

then be etched away in the following etching step. After spinning AZ-5214E photoresist on the sample, the sample is exposed with the mask pattern. After image reversal and development for 50 s in AZ-327, the sample is etched for 20 s in 1:8:80 H_2SO_4:H_2O_2:H_2O. The photoresist is then stripped in acetone for 10 min, then methanol and IPA for 2 min each.

After a 10 min O_2 plasma descum and native oxide removal step in 1:1 HCl:H_2O, the sample is returned to the reactor for regrowth of the $Al_{0.75}Ga_{0.25}As$ upper cladding and p+ GaAs contact layers. The entire growth is performed at 600 ºC with a 10 min bakeout step prior to the beginning of the growth. The growth consists of 10 nm of intrinsic GaAs to complete the upper core, followed by 1.5 μm of carbon-doped p-type $Al_{0.75}Ga_{0.25}As$ and 100 nm of Zn-doped p+ GaAs which forms the contact layer. After the regrowth, the sample is removed from the reactor for contact processing, lapping and polishing, and metallization.

Contact processing begins with etching of the p+ GaAs cap layer with a 3 μm stripe pattern aligned with the underlying 4 μm wide ridge waveguides. This step provides for lateral current confinement by preventing current spreading in the highly conductive contact layer. After photolithography of the 3 μm stripe pattern, the sample is etched in 4:1 $C_6H_8O_7$:H_2O_2 for 45 s. After stripping the photoresist, the sample is cleaned in an O_2 plasma for 10 min. The next processing step consists of definition of contact vias, which provides for additional lateral carrier confinement. This step begins with the deposition of a 100 nm layer of PECVD oxide. Photolithography is again performed to define 2 μm stripe windows aligned to the 4 μm wide ridge waveguides. After development, the oxide in the 2 μm stripe regions is etched in a Freon-14 plasma for 5

min. The photoresist is again stripped in acetone, methanol, and IPA, and the sample is cleaned in an O_2 plasma for 10 min. The native oxide is removed in 1:1 HCl:H_2O for 15 s immediately prior to loading the sample into the evaporator to eliminate any contact resistance added by the thin oxide layer.

P-side metallization is then performed which consists of 100 Å Ti to promote adhesion, 100 Å Pt which serves as a Au diffusion barrier, and 2500 Å of Au. After evaporation, the substrate is lapped to a thickness of approximately 100 μm to facilitate cleaving and dicing as well as reduce contact resistance. After backside polishing, the sample is then returned to the evaporator for evaporation of n-side metals which consist of 200 Å Ge, 500 Å Au, 300 Å Ni, and 500 Å Au. The contacts are then annealed in an H_2 ambient for approximately 20 s at 350 ºC. The sample is then cleaved into 1 mm bars and diced into individual devices for testing and further characterization. Figure 2.6 shows the spectrum obtained from a wet-etched PQD laser with 40 nm diameter QDs along with the spectrum from a quantum well control laser for comparison. The wet-etched PQD laser appears to be lasing on both the GaAs core at 850 nm as well as the QDs at 948 nm at a current of 100 mA. The QD emission is blueshifted by 20 nm compared to the quantum well emission, which is consistent with quantum confinement and strain effects predicted by simulation.

2.7 Figures

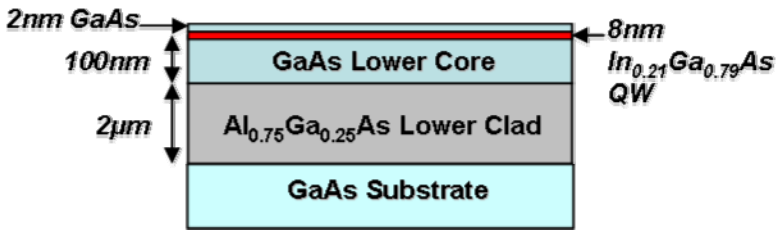

Fig. 2.1 Base structure for fabrication of wet-etched patterned quantum dot lasers.

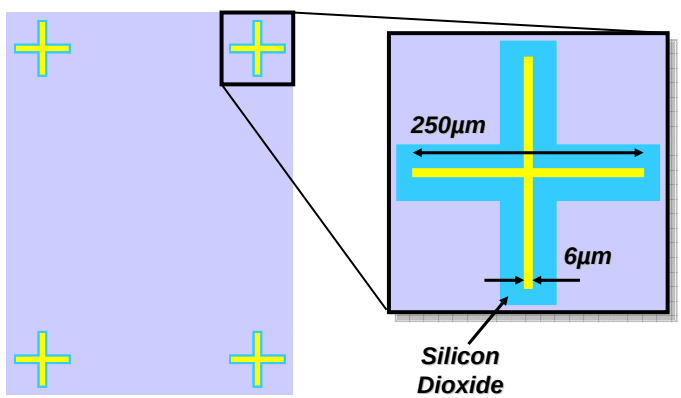

Fig. 2.2 Layout of alignment marks for electron beam system calibration and registration.

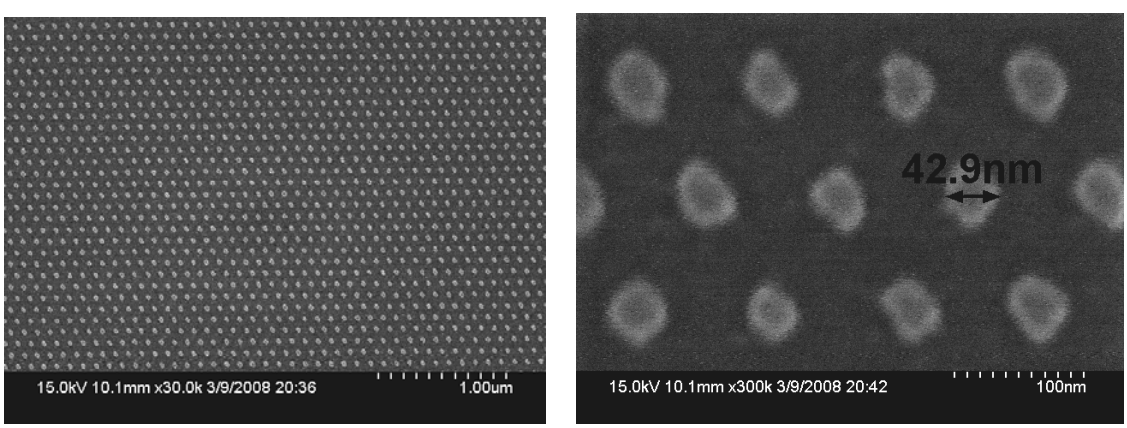

(a) (b)

Fig. 2.3 Patterned QD array after etching and stripping of the HSQ/oxide etch mask at a magnification of (a) 30k and (b) 300k.

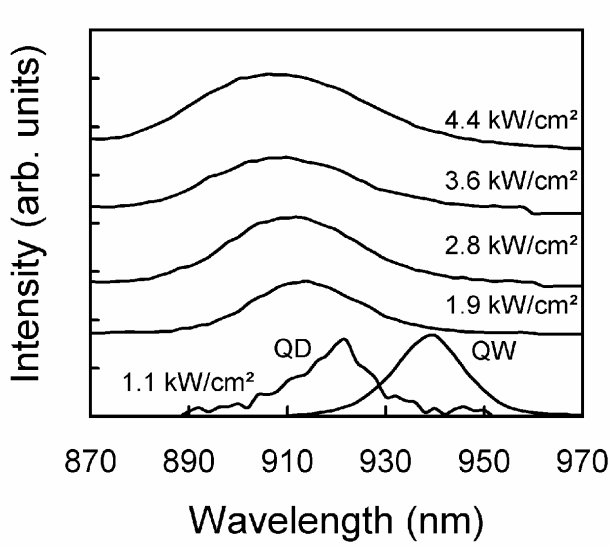

Fig. 2.4 QD spectra measured at 5 different pump powers. The peak at 940 nm is the quantum well (QW) spectrum measured at 1.1 kW/cm^2, while the peak at 922 nm is the QD emission measured at the same pump intensity. The QD emission at 1.1 kW/cm^2 has been enhanced by 30 dB and the QW emission reduced by -10 dB for clarity.

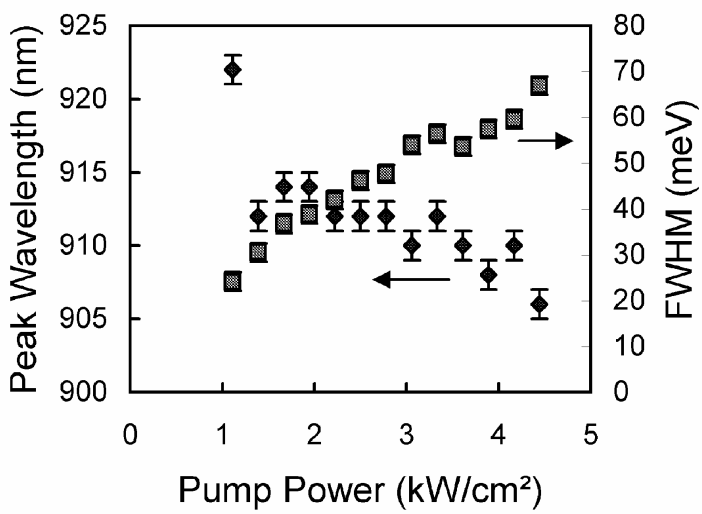

Fig. 2.5 Peak wavelength and full width at half maximum (FWHM) of the QD emisison as a function of pump power.

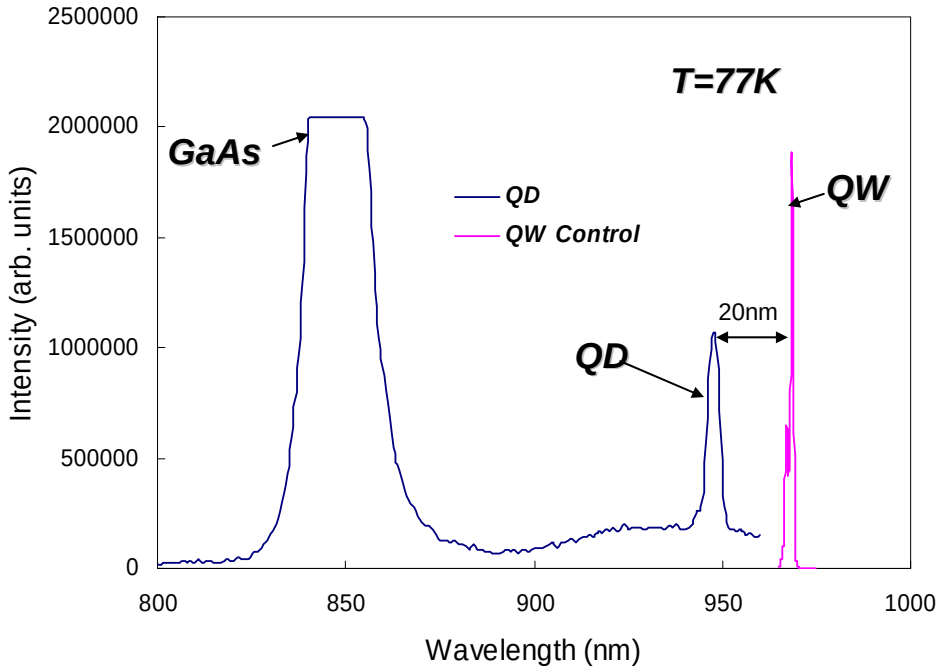

Fig. 2.6 Wet-etched patterned QD laser emission spectrum and quantum well control laser spectrum for comparison.

CHAPTER 3 – THE PATTERNED QUANTUM DOT MOLECULE LASER

As shown in Chapter 2, the lack of sufficient gain from a single layer of QDs resulted in lasing on both the GaAs core as well as the InGaAs QDs. This is clearly an undesirable property which can only be eliminated by increasing the available QD gain. The obvious solution which has been used in QD lasers for many years is to stack multiple layers of QDs. Due to strain fields created by the first QD layer, the QDs in subsequently grown layers tend to self-align with QDs in the first layer, resulting in vertical electronic coupling of the QD layers for small spacer layer thicknesses [42-44]. The result is effectively an array of QD "molecules," which have also been proposed as potential elements of solid state quantum information processing networks [45-47].

Although this is fairly simple to accomplish with self-assembled QDs, creating a patterned QD laser with multiple layers poses significant technical challenges. QDs fabricated using the selective area epitaxy technique typically have a pyramidal shape resulting from the significantly faster growth rate on the (100) plane compared to the (111) planes. Thus, using this process would result in significantly smaller quantum dots in the second layer in comparison to the first layer, which would result in an unacceptable level of inhomogeneous broadening.

The wet-etching technique presented in Chapter 2, however, lends itself nicely to the fabrication of multiple layers of QDs by incorporating two or more quantum wells into the base structure and etching through both wells. This creates self-aligned QDs which are vertically coupled quantum mechanically to form a QD "molecule." In this chapter we present the fabrication process for the proposed QD molecule laser and discuss the simulation and experimental results.

3.1 Device Processing

The base structure growth is virtually identical to that discussed in Section 2.1.1, with the exception of the quantum well layers. In this case two identical 6 nm thick $In_{0.21}Ga_{0.79}As$ QWs are grown with a 6 nm GaAs spacer layer and 2 nm GaAs cap. The spacer layer is thin enough to provide for significant quantum mechanical coupling between the two QW layers.

After a 2 min dehydration bake at 200 °C, electron beam resist consisting of a 2% solution of polymethylmethacrylate (PMMA) in anisole was spun on the sample to obtain a resist thickness of approximately 60 nm. This was followed by a 2 min softbake of the resist at 200 °C. The resist was exposed in a JEOL JBX-6000-FS series electron beam lithography tool with a series of stripes which are 3 mm long and 10 μm wide. Each stripe consists of a triangular array of dots on a 140 nm pitch, yielding a dot density of 6×10^{9} cm^{-2}. Two additional stripes were intentionally overdosed to create rectangular open areas to act as quantum well control devices. Alignment features were also patterned during this step using the electron beam for subsequent optical lithography steps. After exposure, the resist was developed at 10 °C in a solution of 1:2 methylisobutylketone (MIBK):IPA for 3 min, followed by a 30 s rinse in IPA and N_2 dry.

After the evaporation of a 20 Å layer of titanium, liftoff was performed in acetone for 1 h followed by 15 min of ultrasonication to ensure complete removal of the titanium between the dots in the patterned regions. The titanium dots serve as the wet etch mask for the two underlying quantum wells of the base structure.

Wet etching was performed in a solution of 1:4:495 H_3PO_4:H_2O_2:H_2O immediately after removal of the native surface oxide using a solution of 1:10 NH_4OH:H_2O. The target etch depth was 25 nm to ensure complete etching through both

quantum well layers. After etching, the titanium was stripped in buffered hydrofluoric acid for 1 min. Figure 3.1 shows a scanning electron micrograph of the patterned QDs after etching. Note that the alignment features are also transferred into the sample during this wet-etching step.

After a solvent clean in acetone, methanol, and isopropanol (IPA), the sample was cleaned in an O_2 plasma at 300 W for 3 min. Regrowth of the upper core of the laser structure was performed at 100 mbar at 625 °C in an AIX 200/4 MOCVD reactor. The upper core consists of 90 nm of intrinsic GaAs grown at a slow growth rate of 0.2 nm/s and a V/III ratio of 50. Immediately before loading the sample into the MOCVD reactor, a native oxide removal step was performed in a nitrogen-purged loadlock with a 1:10 NH_4OH:H_2O solution for 30 s, followed by a 10 s rinse in H_2O and a 20 s rinse in IPA.

Ridge waveguides of 4 μm width were then patterned over the 10 μm wide stripes containing the buried QDs using standard optical lithography techniques. The ridge waveguides were etched to a depth of 125 nm in 1:8:80 H_2SO_4:H_2O_2:H_2O. The photoresist was then removed in acetone followed by a 10 min clean in an O_2 plasma at 300 W.

Regrowth of the upper cladding and contact layers was performed at atmospheric pressure in a Thomas Swan MOCVD reactor. A native oxide removal step was performed immediately prior to loading the sample. The final regrowth consists of 10 nm of intrinsic GaAs followed by a 1.5 μm p-type $Al_{0.75}Ga_{0.25}As$ upper cladding and a 100 nm p+ GaAs contact layer, which completes the buried heterostructure laser structure shown in Figure 3.2.

Following the upper cladding and contact layer regrowth, 3 μm wide stripes aligned over the buried 4 μm wide waveguides were etched into the p+ GaAs contact layer to reduce current spreading. A 100 nm layer of SiO_2 was then deposited by plasma enhanced chemical vapor deposition (PECVD), followed by optical lithography to define 2 μm wide vias over the 3 μm wide p+ GaAs stripes. The via pattern was transferred into the underlying SiO_2 using a Freon-14 reactive ion etch. P-side metals were then evaporated, followed by lapping and polishing of the substrate to a thickness of approximately 150 μm to facilitate cleaving. Finally, n-side metals were deposited and annealed, and the devices were cleaved into 3 mm long bars for testing. The laser facets were left uncoated.

3.2 Simulation

The technique used to analyze the quantized energy states of the QDs is known as the partial function expansion method, in which the wavefunctions are expanded as the superposition of orthogonal partial functions:

$$\psi(r,\varphi,z) = \sum_{n,m,l} A_{nml}\psi_{nml}(r,\varphi,z)\,, \tag{3.1}$$

where ψ_{nml} are the orthogonal partial functions which are given by

$$\psi_{nml}(r,\varphi,z) = R_{nm}(r)Z_l(z)\Phi(\varphi) \tag{3.2}$$

$$\Phi_m(\varphi) = \frac{1}{\sqrt{2\pi}}e^{im\varphi} \tag{3.3}$$

$$R_{nm}(r) = \frac{\sqrt{2}}{\rho_0 J_{m+1}(k_n\rho_0)}J_m(k_n r) \tag{3.4}$$

$$Z_l(z) = \sqrt{\frac{2}{H}}\sin l\pi\left(\frac{1}{2}-\frac{z}{H}\right). \tag{3.5}$$

The QD is assumed to be embedded in a large boundary cylinder of height H and radius ρ_0 where the wavefunction is zero by design of the partial functions. Inside the QD, the particle has effective mass $m^*(r,z) = m_w$, and the potential has the value $V(r,z) = 0$. In the matrix material occupying the region between the QD and boundary cylinder, the particle has effective mass $m^*(r,z) = m_b$ and the potential has the value $V(r,z) = V_0$. Using (1.1) in the Schrödinger equation

$$-\frac{\hbar^2}{2}\nabla \cdot \frac{1}{m^*(r,z)}\nabla \psi + V(r,z)\psi = E\psi \tag{3.6}$$

yields an equation of the form

$$-\frac{\hbar^2}{2}\nabla \cdot \frac{1}{m^*(r,z)}\nabla \sum_{n,m,l} A_{nml}\psi_{nml} + V(r,z)\sum_{n,m,l} A_{nml}\psi_{nml} = E\sum_{n,m,l} A_{nml}\psi_{nml} \,. \tag{3.7}$$

Multiplying both sides of the equation by $\psi^*_{n'm'l'}$ and integrating over the three-dimensional boundary cylinder yields a matrix equation of the form

$$\sum_{n,m,l} A_{nml} M_{nmln'm'l'} = EA_{n'm'l'} \,. \tag{3.8}$$

Spatial variations of the effective mass and potential are taken into account by dividing the integration into parts in which the effective mass and potential are constant. Further details have been outlined in [39-41]. For simplicity we assumed perfectly cylindrical QD shape for our calculations.

Strain-induced band edge shifts were calculated using commercial three-dimensional finite element analysis software (ABAQUS). Figure 3.3 shows the finite element mesh used for the analysis. The model consists of two 6 nm thick, 55 nm diameter cylindrical quantum dots with a 6 nm GaAs spacer layer embedded in 50 nm thick GaAs layers. The central QD/spacer region and the upper and lower GaAs barrier

layers were each created as separate parts. A tied contact condition was used between the barrier layers and the central QD/spacer layer to model rigid contact between the three pieces of the model. A 6-node linear triangular prism element was used to create the mesh, with a higher mesh density used in the QD/spacer region of the model. All displacement components for nodes on the base of the model were constrained, while for the vertical faces the normal component of motion was constrained to model the periodicity of the structure. Orthotropic elasticity tensors were used for both the GaAs and $In_{0.21}Ga_{0.79}As$ materials. The strain induced due to lattice mismatch was simulated by assigning a thermal expansion coefficient of $\alpha_T = (a - a_0)/a = 0.015$ to the $In_{0.21}Ga_{0.79}As$ material and raising the model temperature by 1 K, where a_0 is the lattice constant of the GaAs substrate and a is the lattice constant of the $In_{0.21}Ga_{0.79}As$. This effectively results in an expansion of the $In_{0.21}Ga_{0.79}As$ material in the simulation and contributes to the force vector in the finite element equations. The band-edge shifts are computed from the various components of the strain tensor produced by the simulation using the following equations:

$$\Delta E_c = a_c(\varepsilon_{xx} + \varepsilon_{yy} + \varepsilon_{zz}) \tag{3.9}$$

$$\Delta E_{HH} = -P - \mathrm{sgn}(Q)\sqrt{|Q|^2 + |R|^2 + |S|^2} \tag{3.10}$$

$$P = -a_v(\varepsilon_{xx} + \varepsilon_{yy} + \varepsilon_{zz}) \tag{3.11}$$

$$Q = -\frac{b}{2}(\varepsilon_{xx} + \varepsilon_{yy} - 2\varepsilon_{zz}) \tag{3.12}$$

$$R = \frac{\sqrt{3}}{2}b(\varepsilon_{xx} - \varepsilon_{yy}) - id\varepsilon_{xy} \tag{3.13}$$

$$S = -d(\varepsilon_{xz} - i\varepsilon_{yz}) . \tag{3.14}$$

Using this model, we computed a conduction band edge shift of ΔE_c = 123 meV which is uniform throughout the majority of the QD volume except at the edges of the QD where ΔE_c increases to 126 meV. The 123 meV shift represents an increase of 14 meV relative to the conduction band shift of 109 meV in a double $In_{0.21}Ga_{0.79}As/GaAs$ quantum well. The computed shift in the HH band edge was ΔE_{HH} =16.5 meV at the center of the QD and decayed to $\Delta E_{HH} \approx 0$ close to the edges. This shift represents a decrease of 15.5 meV relative to a double quantum well for which ΔE_{HH} = 32 meV. Thus, the expected blueshift in emission wavelength of the stacked QDs relative to a stacked QW, due strain effects alone, amounts to 30.5 meV or 20 nm. Physically, this shift can be attributed to an increase in hydrostatic strain or a decrease in QD volume caused by the GaAs barrier material acting on the vertical sidewalls of the QD.

For the calculation of the electron and heavy hole confined energies, we assumed that the band edge energies were constant throughout the QD volume, which is a good approximation considering most of the variation occurs very close to the edges of the QD and the variations are much smaller than the potential barrier height. It was found that in stacked QDs with 55 nm diameter, the increase in electron energy relative to a stacked quantum well is only 0.8 meV, while the increase in the heavy hole energy is approximately 0.2 meV. Thus, the blueshift due to quantum size effects is negligible compared to the blueshift due to strain-induced shifts in the band edges for QDs of this diameter.

3.3 Characterization and Results

The QD lasers were tested under pulsed operation in a liquid nitrogen cryostat at 77 K with a 2 μs pulse width and 0.3% duty cycle. Figure 3.4 shows amplified spontaneous emission spectra collected from the laser facet at a current of 10 mA from a QD laser and a QW control laser. The band edge of the QD emission is blueshifted relative to that of the QW emission by approximately 20 nm, which is in good agreement with the theoretical predictions of the strain-induced blueshift. Figure 3.5 shows the evolution of the amplified spontaneous emission spectrum for a PQD laser with increasing current along with the theoretically predicted joint density of states. The clear presence of excited states in the amplified spontaneous emission spectra close to threshold provides evidence for the three-dimensional confinement of carriers in these QDs.

Figure 3.6 shows the amplified spontaneous emission linewidth as a function of current, while Fig. 3.7 shows the integrated power as a function of current. The drastic decrease in linewidth and increase in integrated power above 36 mA determine the onset of lasing, corresponding to a threshold current density of 307 A/cm^2. This value is higher than the threshold for the double quantum well control device which demonstrated a threshold current of 20 mA corresponding to a threshold current density of 171 A/cm^2. We suspect the increase in threshold in the QD laser device is due to a combination of the low peak gain provided by the relatively sparse QD array, as well as possible processing-induced damage related to the wet-etching and regrowth of the barrier layers.

Figure 3.8 shows the QD and QW laser emission spectra with both devices biased just above threshold. Note that although the spontaneous emission band edges are separated by 20 nm (30 meV) at low currents as shown in Fig. 3.4, the QD device lases

on an excited state at 880 nm where the density of states is largest as shown in Fig. 3.5, resulting in a 30 nm (46 meV) blueshift of the QD laser emission relative to the QW laser emission.

Figure 3.9 presents the evolution of the QD laser emission spectrum as a function of current between currents of 50 mA and 300 mA. As the current is increased, multiple excited states appear in the spectra due to gain saturation of the low energy states.

3.4 Figures

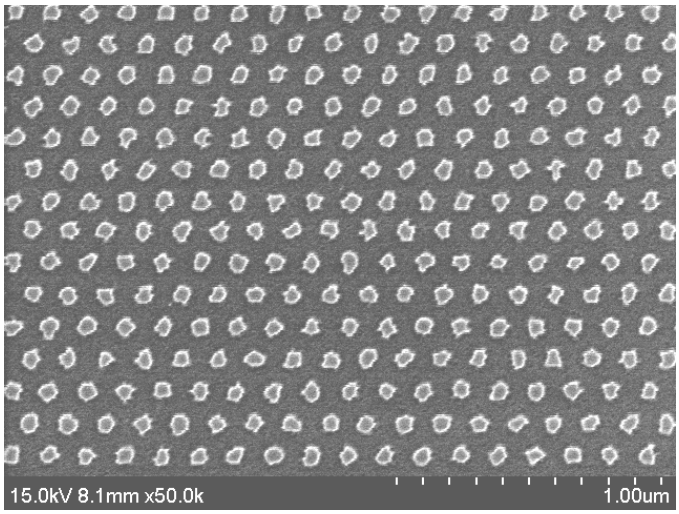

(a)

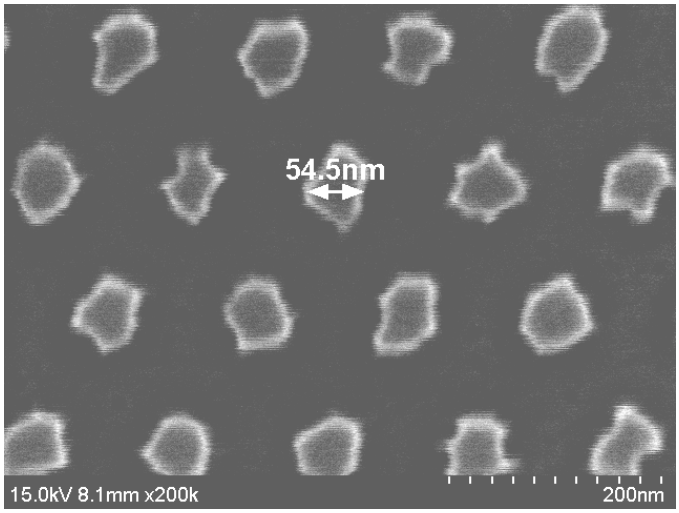

(b)

Fig. 3.1 SEM micrograph of the stacked QD array after wet etching and removal of the titanium etch mask at a magnification of (a) 50k and (b) 200k.

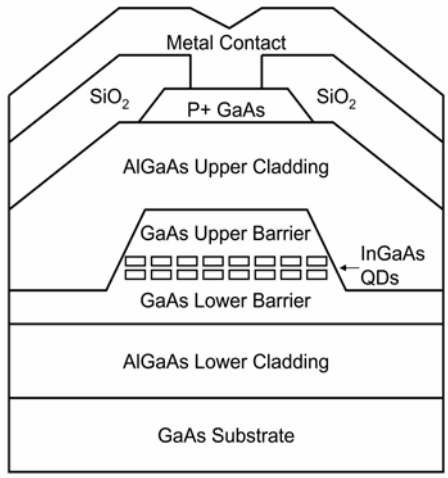

Fig. 3.2 Cross section diagram of the buried heterostructure laser.

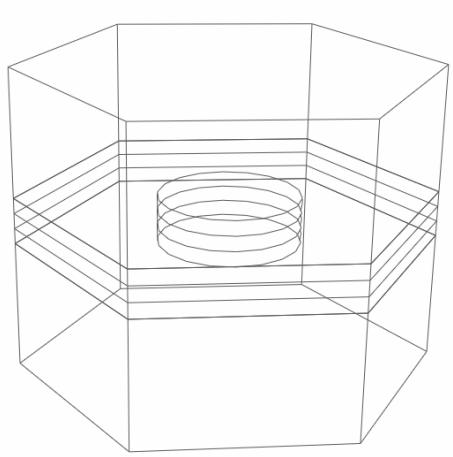

Fig. 3.3 Finite element model of a quantum dot molecule used for modeling the strain-induced shifts in the conduction and valence band edges.

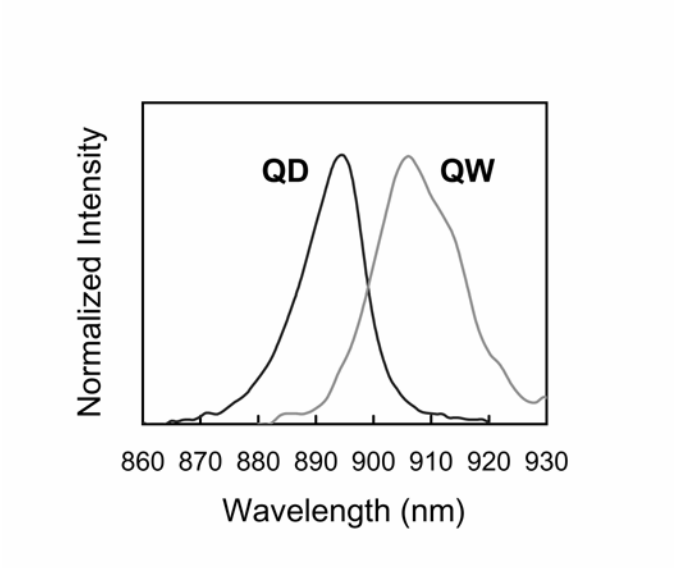

Fig. 3.4 Comparison of QD and QW amplified spontaneous emission spectra at a current of 10 mA.

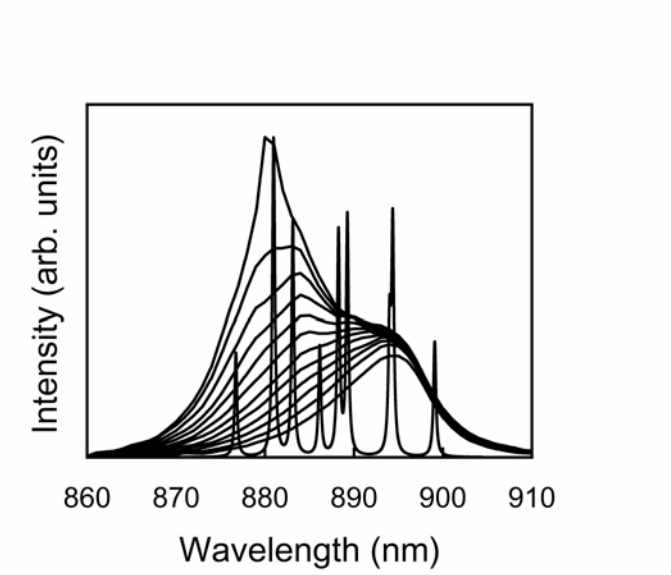

Fig. 3.5 Evolution of the amplified spontaneous emission spectrum of the QD laser below threshold between currents of 10 mA and 32 mA in 2 mA steps. The computed joint density of states is also shown.

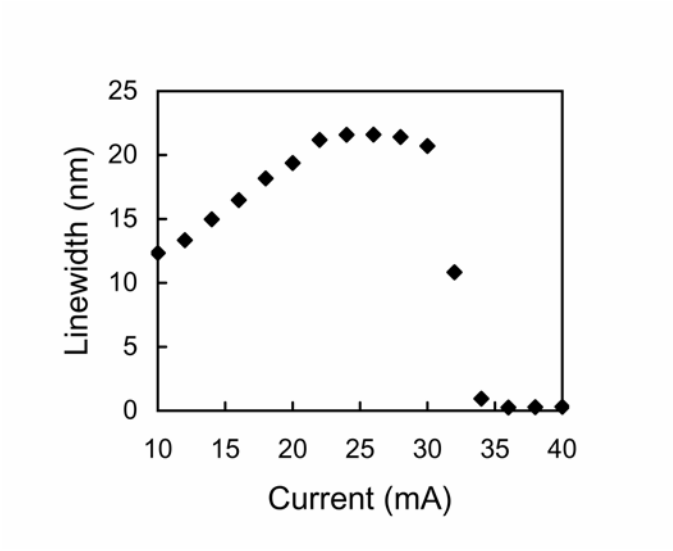

Fig. 3.6 Emission linewidth as a function of current.

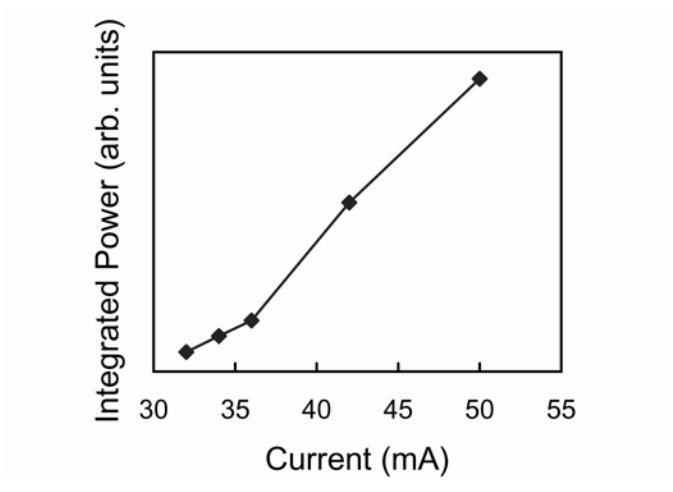

Fig. 3.7 Integrated power as a function of current.

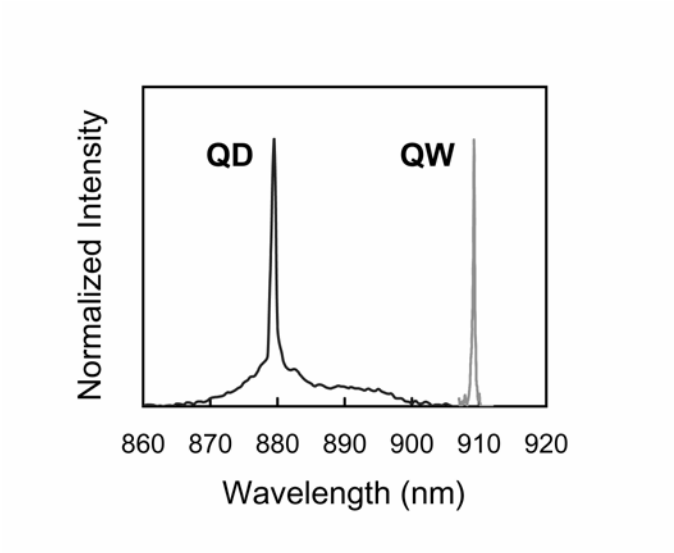

Fig. 3.8 Comparison of QD and QW lasers with each laser biased just above threshold.

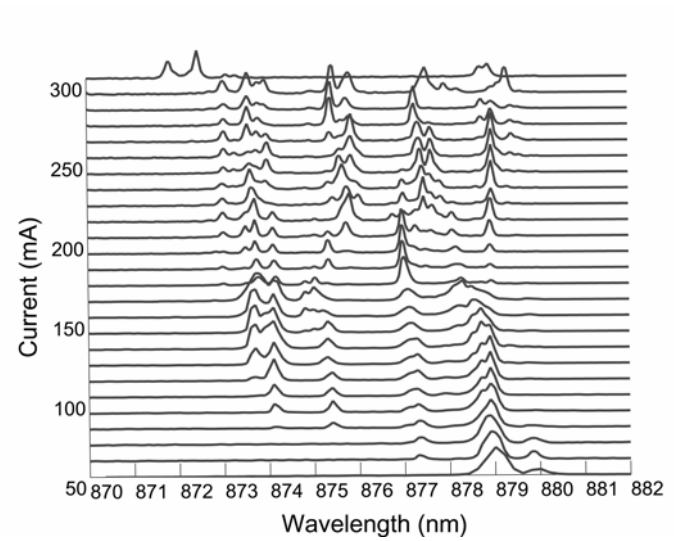

Fig. 3.9 Evolution of QD emission spectrum as a function of current above threshold.

CHAPTER 4 – ANALYSIS OF THE NANOPORE ACTIVE LAYER

The use of direct-write electron beam lithography combined with selective area epitaxial regrowth by metalorganic chemical vapor deposition has recently been explored as a viable method for creating novel semiconductor nanostructures. This process has been successfully used in the fabrication of semiconductor laser diodes with patterned quantum dot and, more recently, inverse quantum dot or "nanopore" active layers [38, 48-50]. Although the properties of semiconductor quantum dots and quantum dot lasers are well understood [51-57], the fundamental properties of the nanopore active layer have not been explored in great detail due to the difficulties involved in fabricating an ordered structure at the scale of tens of nanometers. Properties of the nanopore active layer such as the density of states, selection rules, and gain spectrum must be accurately determined in order to gain insight into the experimentally obtained spectra.

In this chapter we present a three-dimensional model of the nanopore active layer, showing excellent agreement between experiment and theory. The salient features of the mathematical model are outlined in Section 4.1. Beginning with the physical structure of the nanopore active layer, the Schrödinger equation is solved for the periodic potential. In Section 4.2, after determination of the bandstructure and selection rules, the density of states is computed numerically. From the density of states, the gain spectrum is computed. Section 4.3 compares theory with experiment, and discusses the spectral behavior of the nanopore laser as a function of injected current. The observed behavior is explained in terms of the density of states and device physics. In Section 4.4, we discuss a valence band mixing model in order to better understand the bandstructure of excited valence subbands. Section 4.5 outlines the unique nature of the intersubband selection

rules. In Section 4.6, we present a parametric analysis of the effect of the nanopore geometry, material parameters, and temperature on the spectral characteristics of these devices. Section 4.7 discusses the carrier scattering mechanisms in an ordered nanopore array. Finally, Section 4.8 discusses the effects of inhomogeneous broadening. Details of the device fabrication can be found in [38].

4.1 Derivation of Analytical Model

4.1.1 The general approach

The nanopore active layer consists of an ordinary quantum well perturbed by a periodic lattice of energy barriers, as shown in Fig. 4.1. In most respects the structure can be considered to be the electronic analogue of a photonic crystal. The special case of a triangular lattice will be considered here in order to directly correlate the simulation results with experimental data obtained from the fabricated devices.

Numerous numerical methods exist to calculate the allowed energies and wavefunctions in semiconductor nanostructures, including the finite element method and partial function expansion method. Both of these methods have been used in the simulation of quantum dots [58-62]. Methods of simulating the bandstructure of semiconductor crystals as well as photonic crystals are also well developed, the most common being the plane wave expansion method [63-69]. In the following analysis, we use a combination of the partial function expansion and plane wave expansion methods to solve for the bandstructure and wavefunctions of the nanopore active layer.

To begin the analysis, consider the real space unit cell shown in Fig. 4.2. The unit cell has sides of length a equal to the pitch of the triangular lattice, and height H. Inside the quantum well, the particle effective mass is taken to be m_w^*, and the potential V is

taken to be zero. In the barrier regions, we take the effective mass to be m_b^*, and the potential $V = V_0$.

Let us define unit vectors $\hat{\mathbf{u}}$ and $\hat{\mathbf{v}}$ parallel to the edges of the unit cell. The reciprocal space basis vectors $\mathbf{u}^*$ and $\mathbf{v}^*$ are related to the real space unit vectors according to

$$\mathbf{u}^* \cdot \hat{\mathbf{u}} = 2\pi \tag{4.1}$$

$$\mathbf{u}^* \cdot \hat{\mathbf{v}} = 0 \tag{4.2}$$

$$\mathbf{v}^* \cdot \hat{\mathbf{v}} = 2\pi \tag{4.3}$$

$$\mathbf{v}^* \cdot \hat{\mathbf{u}} = 0\,. \tag{4.4}$$

We can express any reciprocal space vector $\mathbf{G}$ or in-plane particle momentum wavevector $\mathbf{k}_t$ as a linear combination of reciprocal space basis vectors as

$$\mathbf{G} = n\mathbf{u}^* + m\mathbf{v}^*, \tag{4.5}$$

$$\mathbf{k}_t = k_n\mathbf{u}^* + k_m\mathbf{v}^*, \tag{4.6}$$

where n, m are integers and k_n, k_m are real numbers. Similarly, any position in two-dimensional real space may be represented as a linear combination of real space basis vectors

$$\boldsymbol{\rho} = u\hat{\mathbf{u}} + v\hat{\mathbf{v}}\,. \tag{4.7}$$

With the coordinate system and basis vectors established, we would like to solve the Schrödinger equation

$$-\frac{\hbar^2}{2m^*}\nabla^2\psi(u,v,z) + V(u,v,z)\psi(u,v,z) = E\psi(u,v,z) \tag{4.8}$$

for the periodic potential of the nanopore active layer. Normalizing to the quantity $\hbar^2/(m_e a^2)$ where m_e is the mass of the electron and a is the pitch of the triangular lattice, one obtains the simplified form

$$-\frac{1}{2m_r^*}\nabla^2\psi(u,v,z)+V(u,v,z)\psi(u,v,z)=E\psi(u,v,z)\,, \tag{4.9}$$

where the potential V and the energy E are now in units of $\hbar^2/(m_e a^2)$, all lengths are normalized to the lattice pitch a, and $m_r^* = m^*/m_e$ is the ratio of the particle effective mass to the free space mass of the electron.

Bloch's theorem allows one to express the in-plane wavefunction as a plane wave modulated by an envelope function having the same periodicity as the real space lattice

$$\begin{aligned}\psi(u,v,z) &= e^{i\mathbf{k}_t\cdot\boldsymbol{\rho}}u_{\mathbf{k}_t}(u,v,z)\\ &= e^{i2\pi(uk_n+vk_m)}u_{\mathbf{k}_t}(u,v,z),\end{aligned} \tag{4.10}$$

where $\mathbf{k}_t$ and $\boldsymbol{\rho}$ refer to the in-plane wavevector and in-plane position vector, respectively. The function $u_{\boldsymbol{k}}$ $(u,\ v,\ z)$ can be expanded in a Fourier series as the sum of reciprocal lattice vector plane waves as

$$\begin{aligned}u_{\mathbf{k}_t}(u,v,z) &= \sum_{i,j} a_{i,j}(\mathbf{k}_t)e^{i\mathbf{G}_i\cdot\boldsymbol{\rho}}f_j(z)\\ &= \sum_{i,j} a_{i,j}(\mathbf{k}_t)e^{i2\pi(n_i u+m_i v)}f_j(z),\end{aligned} \tag{4.11}$$

where $a_{i,j}$ are the Fourier coefficients of the expansion, $\mathbf{G}_i$ represents a reciprocal lattice vector, and $f_j(z)$ is a normalized function of the z-coordinate only.

Note that periodic boundary conditions on the vertical faces of the unit cell are implicitly enforced in the reciprocal space plane wave expansion of the wavefunction. On the top and bottom faces of the unit cell we enforce zero boundary conditions, which is a good approximation provided H is chosen to be sufficiently large. Since the nanopore potential is a simple quantum well in the transverse dimension, it is reasonable to choose a sinusoidal basis with

$$f_j(z)=\sqrt{\frac{2}{H}}\sin j\pi\left(\frac{1}{2}-\frac{z}{H}\right). \tag{4.12}$$

Using (4.10-4.12) in (4.9), one obtains the final form of the Schrödinger equation written in terms of the complete set of basis vectors. The solution of (4.9) then proceeds by multiplying both sides of the equation by $e^{-i\mathbf{G}_{i'}\cdot\boldsymbol{\rho}} f_{j'}(z)$ and integrating over the volume of the unit cell. Utilizing orthonormality of the basis vectors, the resulting equation takes the form of a simple eigenvalue problem of the form

$$\sum_{i,j} a_{i,j}\left(\mathbf{k}_t\right) M_{i,j,i',j'} = E a_{i',j'}\left(\mathbf{k}_t\right). \tag{4.13}$$

The solution to this equation yields the energy eigenvalues and particle wavefunctions at a single point in the Brillouin zone.

Note that the integration over the volume of the unit cell is complicated by the position dependence of the effective mass. The integral can be easily performed, however, by dividing the integral into sections in which the effective mass is a constant. Further details are outlined in the next section.

4.1.2 Detailed mathematical solution

In the following we outline the mathematical details leading to (4.13), beginning with (4.9) and utilizing the basis functions given in (4.10-4.12). The Laplacian in (u,v,z) coordinates has the form

$$\nabla^2 = \frac{4}{3}\left(\frac{\partial^2}{\partial u^2} - \frac{\partial^2}{\partial u \partial v} + \frac{\partial^2}{\partial v^2} + \frac{3}{4}\frac{\partial^2}{\partial z^2}\right). \tag{4.14}$$

Applying this expression to $\psi(u,v,z)$ as given by (4.10) yields

$$\begin{aligned} &-\frac{1}{2m_r^*}\nabla^2\psi(u,v,z) = \\ &\frac{8\pi^2}{3m_r^*} e^{i\mathbf{k}_t\cdot\boldsymbol{\rho}} \sum_{i,j} a_{i,j} \left\{\left[k_n^2 + k_m^2 - k_n k_m\right] + \left[n_i^2 + m_i^2 - n_i m_i\right]\right. \\ &\left. + \left[k_n\left(2n_i - m_i\right) + k_m\left(2m_i - n_i\right)\right] + \frac{3}{4}\left(\frac{j}{2H}\right)^2\right\} e^{i\mathbf{G}_i\cdot\boldsymbol{\rho}} f_j(z). \end{aligned} \tag{4.15}$$

Next, we multiply both sides of (4.9) by $e^{-i\mathbf{G}_{i'}\cdot\boldsymbol{\rho}} f_{j'}(z)$ and integrate over the volume of the unit cell. The integral may be separated into the product of two integrals, one over the (u,v) plane and the other over z.

Beginning with the first term in (4.9), we find that the integral is complicated by the fact that the particle effective mass is not constant over the unit cell. In order to take this into account, we divide the integral into parts in which the effective mass is constant. First, we integrate over the entire unit cell assuming the effective mass is equal to the effective mass of the barrier material. Next, we subtract the integral over the entire (u,v) plane of the unit cell and between $-W/2$ and $W/2$ in the z-dimension assuming $m_r^*=m_b^*$, and add the same integral with $m_r^*=m_w^*$. At this point, the integral has effectively been performed with $m_r^*=m_w^*$ over the quantum well and $m_r^*=m_b^*$ above and below the quantum well. Finally, the difference of the effective mass in the cylindrical pore must be taken into account. To do this, we subtract the integral over the circular pore in the (u,v) plane and between $-W/2$ and $W/2$ in the z-dimension with $m_r^*=m_w^*$, and add the same integral with $m_r^*=m_b^*$. This procedure may be expressed mathematically as

$$\begin{aligned}
&\iiint_{\substack{unit\\cell}} \frac{1}{m_r^*} e^{i(\mathbf{G}_i-\mathbf{G}_{i'})\cdot\boldsymbol{\rho}} f_j f_{j'} dV = \frac{1}{m_b^*} \iiint_{\substack{unit\\cell}} e^{i(\mathbf{G}_i-\mathbf{G}_{i'})\cdot\boldsymbol{\rho}} f_j f_{j'} dV \\
&+\left(\frac{1}{m_w^*}-\frac{1}{m_b^*}\right) \iint_{\substack{unit\\cell}} e^{i(\mathbf{G}_i-\mathbf{G}_{i'})\cdot\boldsymbol{\rho}} du dv \int_{-W/2}^{W/2} f_j f_{j'} dz \\
&+\left(\frac{1}{m_b^*}-\frac{1}{m_w^*}\right) \iint_{\substack{circular\\pore}} e^{i(\mathbf{G}_i-\mathbf{G}_{i'})\cdot\boldsymbol{\rho}} du dv \int_{-W/2}^{W/2} f_j f_{j'} dz \\
&= \frac{1}{m_b^*}\delta_{i,i'}\delta_{j,j'} + Z\left\{\left(\frac{1}{m_w^*}-\frac{1}{m_b^*}\right)\delta_{i,i'} + \left(\frac{1}{m_b^*}-\frac{1}{m_w^*}\right)U\right\}
\end{aligned} \tag{4.16}$$

where

$$Z = \int_{-W/2}^{W/2} f_j f_{j'} dz \tag{4.17}$$

and

$$U = \iint_{\substack{circular \\ pore}} e^{i(\mathbf{G}_i - \mathbf{G}_{i'})\cdot\boldsymbol{\rho}} du dv . \tag{4.18}$$

Using (4.12) for the form of $f_j(z)$, the integral over the z-coordinate can be shown to be equal to

$$\begin{aligned} Z = & \frac{\sin\left(j'+j\right)\frac{\pi}{2}\left(1-\frac{W}{H}\right)-\sin\left(j'+j\right)\frac{\pi}{2}\left(1+\frac{W}{H}\right)}{\pi\left(j'+j\right)} \\ & -\frac{\sin\left(j'-j\right)\frac{\pi}{2}\left(1-\frac{W}{H}\right)-\sin\left(j'-j\right)\frac{\pi}{2}\left(1+\frac{W}{H}\right)}{\pi\left(j'-j\right)} \end{aligned} \tag{4.19}$$

if $j' \neq j$, and

$$Z = \frac{W}{H} + \frac{\sin \pi j\left(1-\frac{W}{H}\right)-\sin \pi j\left(1+\frac{W}{H}\right)}{2\pi j} \tag{4.20}$$

if $j' = j$.

Next, we must evaluate integral (4.18):

$$\iint_{\substack{circular \\ pore}} e^{i(\mathbf{G}_i - \mathbf{G}_{i'})\cdot\boldsymbol{\rho}} du dv = \iint_{\substack{circular \\ pore}} e^{i2\pi\left[(n_i - n_{i'})u + (m_i - m_{i'})v\right]} du dv . \tag{4.21}$$

To evaluate this integral, one must convert from the (u,v) basis to polar coordinates (r,θ)

$$\begin{aligned} U &= \int_0^{\rho}\int_0^{2\pi} \frac{2}{\sqrt{3}} r e^{i2\pi\left[(n_i - n_{i'})r(\cos\theta - (1/\sqrt{3})\sin\theta) + (m_i - m_{i'})(2/\sqrt{3})r\sin\theta\right]} dr d\theta \\ &= \frac{4\pi}{\sqrt{3}}\rho\frac{J_1\left(\rho C\right)}{C} \end{aligned} \tag{4.22}$$

if $C \neq 0$, and

$$U = \frac{2\pi}{\sqrt{3}}\rho^2$$

if C = 0 where

$$
\begin{aligned}
C &= \sqrt{A^2 + B^2} \\
A &= 2\pi\left(n_i - n_{i'}\right) \\
B &= 2\pi\left[\frac{2}{\sqrt{3}}\left(m_i - m_{i'}\right) - \frac{1}{\sqrt{3}}\left(n_i - n_{i'}\right)\right],
\end{aligned}
\tag{4.23}
$$

ρ is the radius of the circular pore normalized to the lattice pitch a, and J_1 is the Bessel function of the first kind. Here we have used the identity

$$
\begin{aligned}
U &= \int_0^{\rho}\int_0^{2\pi} r e^{iAr\cos\theta} e^{iBr\sin\theta} dr d\theta \\
&= 2\pi\rho \frac{J_1\left(\rho\sqrt{A^2 + B^2}\right)}{\sqrt{A^2 + B^2}}.
\end{aligned}
\tag{4.24}
$$

This completes the analysis of the Laplacian term in (4.9).

To evaluate the second term in (4.9) involving the potential V, we follow a similar procedure, dividing the integral into regions in which the potential is a constant. First, we integrate with $V=V_0$ over the entire unit cell. Next, since the potential is zero inside the quantum well, we subtract the integral with $V=V_0$ over the quantum well only, with u and v ranging over the entire unit cell and z between $-W/2$ and $W/2$. Finally, we add the integral with $V=V_0$ over the cylinder of the nanopore. Mathematically, we have

$$
\begin{aligned}
&\iiint_{\substack{unit\\cell}} V e^{i(\mathbf{G}_i - \mathbf{G}_{i'})\cdot\boldsymbol{\rho}} f_j f_{j'} dV = V_0 \iiint_{\substack{unit\\cell}} e^{i(\mathbf{G}_i - \mathbf{G}_{i'})\cdot\boldsymbol{\rho}} f_j f_{j'} dV \\
&\quad - V_0 \iint_{\substack{unit\\cell}} e^{i(\mathbf{G}_i - \mathbf{G}_{i'})\cdot\boldsymbol{\rho}} du dv \int_{-W/2}^{W/2} f_j f_{j'} dz \\
&\quad + V_0 \iint_{\substack{circular\\pore}} e^{i(\mathbf{G}_i - \mathbf{G}_{i'})\cdot\boldsymbol{\rho}} du dv \int_{-W/2}^{W/2} f_j f_{j'} dz \\
&= V_0 \left\{\delta_{i,i'}\delta_{j,j'} - Z\left[\delta_{i,i'} - U\right]\right\}.
\end{aligned}
\tag{4.25}
$$

Finally, the term on the right-hand side of the equality in (4.9), when multiplied by $e^{-i\mathbf{G}_{i'}\cdot\boldsymbol{\rho}} f_{j'}(z)$ and integrated over the volume of the unit cell, simply becomes

$$Ee^{i\mathbf{k}_t\cdot\boldsymbol{\rho}} \sum_{i,j} \delta_{i,i'}\delta_{j,j'} a_{i,j} = Ee^{i\mathbf{k}_t\cdot\boldsymbol{\rho}} a_{i',j'}. \tag{4.26}$$

Combining (4.14-4.26), and noting that the $e^{i\mathbf{k}_t\cdot\boldsymbol{\rho}}$ terms drop out of the equation, we have the final form of the eigenvalue equation:

$$\sum_{i,j} a_{i,j} M_{i,j,i',j'} = Ea_{i',j'} \tag{4.27}$$

where

$$\begin{aligned} M_{i,j,i',j'} = \frac{8\pi^2}{3}\Big\{&\left[k_n^2 + k_m^2 - k_n k_m\right] + \left[n_i^2 + m_i^2 - n_i m_i\right] \\ &+ \left[k_n\left(2n_i - m_i\right) + k_m\left(2m_i - n_i\right)\right] + \frac{3}{4}\left(\frac{j}{2H}\right)^2\Big\} \\ &\times\left\{\frac{1}{m_b^*}\delta_{i,i'}\delta_{j,j'} + Z\left[\left(\frac{1}{m_w^*} - \frac{1}{m_b^*}\right)\delta_{i,i'} + \left(\frac{1}{m_b^*} - \frac{1}{m_w^*}\right)U\right]\right\} \\ &+ V_0\left\{\delta_{i,i'}\delta_{j,j'} - Z\left[\delta_{i,i'} - U\right]\right\}. \end{aligned} \tag{4.28}$$

The derivation is very similar for a rectangular lattice, with the Hamiltonian given by

$$\begin{aligned} M_{i,j,i',j'} = 2\pi^2\Big\{&\left[k_n^2 + 2k_n k_m + k_m^2\right] + \left[n_i^2 + 2n_i m_i + m_i^2\right] \\ &+ \left(\frac{j}{2H}\right)^2\Big\} \times\left\{\frac{1}{m_b^*}\delta_{i,i'}\delta_{j,j'} + Z\left[\left(\frac{1}{m_w^*} - \frac{1}{m_b^*}\right)\delta_{i,i'} + \left(\frac{1}{m_b^*} - \frac{1}{m_w^*}\right)U\right]\right\} \\ &+ V_0\left\{\delta_{i,i'}\delta_{j,j'} - Z\left[\delta_{i,i'} - U\right]\right\}. \end{aligned} \tag{4.29}$$

All terms in this expression can be evaluated analytically. In general, the size of the matrix will be determined by the number of reciprocal lattice vectors used in the expansion. The appropriate number of reciprocal lattice vectors to use in the expansion must be determined by observing the rate of convergence of the eigenvalues with an increasing number of vectors. All simulation results presented here were obtained by using 81 reciprocal space vectors for the in-plane component of the wavefunction, and 9

vectors for the transverse component of the wavefunction, for a total of 729 basis vectors. This number was found to be sufficient to provide accuracy in the computed eigenvalues to better than 0.1 meV.

4.2 Simulation Results

4.2.1 Bandstructure

Computation of the bandstructure over the hexagonal Brillouin zone follows directly from (4.13). The computation was performed for an 8-nm-thick $In_{0.25}Ga_{0.75}As/GaAs$ quantum well perturbed by a triangular lattice of 40-nm-diameter pores on an 80-nm-pitch, and assuming a temperature of 77 K. These parameters correspond with those of the device structure from which the experimental data was obtained [38]. Figure 4.3 shows the result of the computation performed for the first three conduction subbands, while Fig. 4.4 shows the same computation performed for the first three valence subbands. Energies in the figures are referenced relative to the respective strained band edges. Wavefunctions at the symmetry points of the Brillouin zone are shown in Fig. 4.5.

4.2.2 Density of states

In order to compute the density of states from the bandstructure, we begin by discretizing both **k**-space and energy space. At each discrete energy E, we choose some small interval ΔE around that energy, and count the number of **k**-points which map to an energy within this interval. We then multiply the number of **k**-points by the area per **k**-point, which will depend on the mesh density. Finally, we divide this total area by the area per state in **k**-space, $(2\pi/L)^2$. The density of states at energy E is then given by

$$\rho(E) = \frac{N}{V\Delta E} = 2 \times \frac{kArea/(2\pi/L)^2}{L^2 W \Delta E} = \frac{kArea}{2\pi^2 W \Delta E}, \tag{4.30}$$

where N is the number of k-states within the energy interval ΔE, V is a real-space volume, *kArea* represents the area of k-space which maps to the energy interval ΔE, and the factor of 2 accounts for spin degeneracy. Plots of the conduction and valence band density of states obtained in this manner are shown in Figs. 4.6 and 4.7, respectively.

4.2.3 Selection rules

In order to compute the gain spectrum, one must first compute the joint density of states, which takes into account the bandstructure of both the conduction and valence bands as well as the selection rules determining the allowed transitions between subbands.

The selection rules can be determined by evaluation of the overlap integral $\left|I_{hm}^{en}\right|^2 = \left|\langle \psi_n | \psi_m \rangle\right|^2$ of the electron and hole wavefunctions over a unit cell. Note that orthonormality of the basis functions allows one to express the overlap integral very simply in terms of the eigenvectors obtained from the solution of (4.27) as

$$I_{hm}^{en} = \sum_{i,j} a_{i,j}^{*n} a_{i,j}^{m} . \tag{4.31}$$

Upon performing this computation one finds that, to an excellent approximation, only transitions between like-numbered subbands are allowed with $\left|I_{hm}^{en}\right|^2 \approx 1$. That is, only transitions between conduction subband number n, and valence subband number $m = n$, are allowed. For all other transitions, $\left|I_{hm}^{en}\right|^2 \approx 0$. In general, the overlap integral will vary across the Brillouin zone as shown in Fig. 4.8. However, note that the magnitude of the variation is negligible and limited primarily to a small region around the K symmetry

points of the Brillouin zone. The result of the joint density of states computation taking into account these interband selection rules is shown in Fig. 4.9.

4.2.4 Gain spectrum

With the joint density of states determined, the gain spectrum can be derived using the gain equation with Lorentzian broadening term

$$g(\hbar\omega) = \frac{\pi e^2}{n_r c \varepsilon_0 m_0^2 \omega} \sum_{n,m} \left| I_{hm}^{en} \right|^2 \int_0^\infty dE \rho_j(E) \left| \hat{e} \cdot \mathbf{p}_{cv} \right|^2 \times \frac{\Gamma/(2\pi)}{\left[E - \hbar\omega\right]^2 + (\Gamma/2)^2} \left[f_c^n(E) - f_v^m(E) \right] \tag{4.32}$$

where n and m denote the number of a specific subband in the conduction and valence band, respectively, $\rho_j(E)$ is the joint density of states function, $\left|\hat{e} \cdot \mathbf{p}_{cv}\right|^2$ is the momentum matrix element, Γ is the full width at half maximum of the Lorentzian broadening term, and f_c^n and f_v^m are the Fermi distribution functions for electrons in the conduction and valence bands [69]. In addition, for simplicity we take $\left|\hat{e} \cdot \mathbf{p}_{cv}\right|^2 = 3M_b^2/2$, where $M_b^2 = m_0 E_p/6$, and E_p is the optical matrix parameter equal to 25.7 eV for GaAs. This is a good approximation due to the fact that the in-plane kinetic energy of the first three subbands is small relative to the transverse confinement energy. The gain spectrum obtained from carrying out the calculation in (4.32) is shown in Fig. 4.10(a). A 1 meV Lorentzian broadening term was determined to provide the best agreement with the experimentally obtained spectrum shown in Fig. 4.10(b), which was obtained from a 1 mm long device at a resolution of 0.1 nm in pulsed operation with a 2 μs pulse width and 0.3% duty cycle and at a temperature of 77 K.

4.3 Comparing Analysis with Experiment

The spectrum in Fig. 4.10 consists of two distinct peaks: a narrow peak at 959 nm and a broad peak at 963 nm. Comparing the simulated spectrum to the joint density of states in Fig. 4.9, one finds that the broad peak at 963 nm is caused by the overlap of the first and second subbands, where the second subband appears as a shoulder on the peak caused by the first subband. The narrow peak at 959 nm is a result of the delta-function-like density of states of the third subband. The simulated gain spectrum shows excellent agreement with the experimentally obtained spectrum at an injection current of 90 mA, as shown in Fig. 4.10(b). It should be noted that the absence of distinct Fabry-Perot modes in the experimentally obtained laser spectrum is likely due to chirp resulting from the pulsed operation of the device. However, the light vs. current curve in [39] shows without ambiguity that the device is in fact lasing.

Figure 4.11 shows a plot of the experimentally obtained spectra of the nanopore laser as a function of injection current between 0 and 200 mA at a temperature of 77 K. The plot in Fig. 4.12 shows the position of each of the three peaks corresponding to the three subbands as a function of the injected current. The peaks of the first two subbands were obtained by deconvolution of the broad peak into two Lorentzians. The first subband experiences the strongest redshift of approximately 3 nm, which can be attributed to junction heating. From the magnitude of the redshift, one can extract the increase in junction temperature, assuming that the temperature at zero bias current is 77 K, to be approximately 20° over the 200 mA range of injection current. The second subband experiences a smaller redshift of just over 1 nm. Finally, the third subband experiences a net blueshift.

There are two physical mechanisms underlying the observed behavior of the second and third subbands. The first mechanism is slow carrier relaxation from higher subbands into lower subbands, which results in fast saturation of the second and third subbands. The second mechanism is growth enhancement across the 4-μm-wide laser stripe, which results in a slightly thicker quantum well in the center of the stripe relative to the edges.

Slow carrier relaxation is manifested in the laser spectrum at low currents. Lasing begins on the third and second subbands at a current of 10 mA. Between 10 mA and 50 mA, lasing on the second subband gradually shifts over to the first subband. From the joint density of states in Fig. 4.10, one finds that the gain for the second subband is lower than the first, and therefore it should have a higher lasing threshold. Contrary to this expectation, lasing on the second subband is observed at even lower currents than the first subband. This contradiction suggests a reduced relaxation rate from higher subbands into lower subbands via longitudinal optical (LO) phonon scattering. The reduction in LO phonon scattering rate, also known as the phonon bottleneck effect, is routinely observed in terahertz quantum cascade lasers when the miniband separation is significantly lower than the LO phonon energy of 36 meV in GaAs [70-76]. The phonon bottleneck effect results in the third subband reaching saturation before the first and second subbands. This effect is necessary to explain the observed blueshift in the third subband, as well as the reduced redshift in the second subband.

In addition to fast saturation of the third subband, growth enhancement across the 4 μm wide laser stripe must be taken into account in order to explain the blueshift. The magnitude of the growth enhancement can be estimated using the ratio of open area not

occupied by the hydrogen silsesquioxane (HSQ) dots used as the growth template to total area in a unit cell of the nanopore pattern. For an 80 nm pitch nanopore pattern with 40 nm diameter dots, this ratio is approximately 1.3. Thus, if the quantum well in the center of the stripe is 8 nm thick, the quantum well outside of the laser stripe must have a thickness of approximately 8/1.3=6.2 nm. One can imagine that there must exist some distribution in quantum well thickness across the nanopore stripe pattern satisfying these boundary conditions, with a thicker well at the center and thinner well toward the edges. As described in [39], the initial stripe width is 10 μm, which is later reduced to 4 μm by wet etching after regrowth of the nanopore active layer and GaAs cap. For simplicity, let us assume a linear distribution in quantum well thickness from the center to the edge of the 10 μm wide stripe. The total change in quantum well thickness should be 8 nm - 6.2 nm = 1.8 nm. When the stripe width is reduced to 4 μm by wet etching, the deviation from the center to the edge of the etched stripe should be reduced by a factor of 0.4, for a total change in quantum well thickness of approximately 0.7 nm.

The thickest part of the quantum well, and therefore the region of lowest carrier energy, is found at the center of the laser stripe. At low current levels, it is reasonable to assume that the majority of carriers can be found in the low energy region at the center of the stripe. As the current increases, fast saturation of the third subband results in a combination of spatial and spectral hole burning, causing the active lasing carrier population in the third subband to continuously shift outward toward the edges of the stripe where the thinner quantum well results in higher carrier energy.

Let us postulate that the spectral blueshift of the third subband is caused by this effect. One can easily calculate the change in quantum well thickness required in order to

cause the observed blueshift, after taking the thermal redshift into account. Performing this calculation at a current of 200 mA, one finds that the necessary change in thickness is approximately 0.7 nm, which is in excellent agreement with the change predicted by a simple linear growth enhancement profile. A similar line of reasoning could be used to explain the smaller redshift of the second subband relative to the first subband.

We note briefly that the 1 meV broadening term introduced into the gain spectrum computation should contain three primary components: inhomogeneous broadening due to growth enhancement effects, electron-phonon scattering, and electron-electron scattering. The inhomogeneous broadening contribution should be significantly less than 1 meV due to carrier energy relaxation toward the lowest energy region of the stripe and spectral and spatial hole burning as discussed above. However, the scattering contribution would still appear to be rather small. Fermi's rule states that the electron-phonon scattering rate depends on the matrix element of the interaction Hamiltonian given by

$$\left\langle e^{i\mathbf{k}_t'\cdot\boldsymbol{\rho}} u_{\mathbf{k}_t'}(u,v,z) \middle| e^{i\mathbf{q}\cdot\mathbf{r}} \middle| e^{i\mathbf{k}_t\cdot\boldsymbol{\rho}} u_{\mathbf{k}_t}(u,v,z) \right\rangle, \tag{4.33}$$

where $\mathbf{q}$ is the phonon wavevector. It appears plausible that since the envelope functions $u_{\boldsymbol{k}}$ change significantly as a function of in-plane momentum vector $\mathbf{k}_t$ as well as between subbands, that the magnitude of this matrix element is significantly reduced compared to an ordinary quantum well, resulting in a reduced electron-phonon scattering rate. This hypothesis requires further investigation.

In addition, the dispersion relation given here differs from that presented in [38]. The dispersion relation in [38] was computed for a nanopore lattice with 10-nm-diameter pores on a 20 nm pitch, which differs significantly from the actual device parameters of 40 nm diameter pores on an 80 nm pitch.

4.4 Valence Band Mixing Model

The one-band effective mass model outlined in the last section is sufficient for predicting the nanopore bandstructure close to the band edges. However, as will be shown in Chapter 5, it is also possible for a nanopore laser device to lase on higher energy subbands. In this case, the one-band model is accurate only for the conduction band and first heavy hole band, but loses its validity in the valence band due to mixing effects. Due to the proximity of the excited heavy hole subbands to the light hole subbands in energy, there is significant mixing introduced by three-dimensional quantum confinement between the two bands even for small **k**-vectors. This effect has been studied in other quantum nanostructures such as quantum dots and quantum wires [77]. In this section, we show that valence band mixing is an important effect in the nanopore structure because it leads to significant shifts in the band edges of excited heavy hole subbands, and also results in an increase in the density of states of higher energy subbands. The higher density of states combined with slow carrier relaxation rates as outlined in Section 4.7 can lead to lasing on the excited state subbands as will be demonstrated in Chapter 5.

4.4.1 The Pikus-Bir Hamiltonian

The valence bandstructure in a strained material system is governed by the Pikus-Bir Hamiltonian given by

$$H=-\begin{bmatrix} P+Q & -S & R & 0 & -\frac{1}{\sqrt{2}}S & \sqrt{2}R \\ -S^{\dagger} & P-Q & 0 & R & -\sqrt{2}Q & \sqrt{\frac{3}{2}}S \\ R^{\dagger} & 0 & P-Q & S & \sqrt{\frac{3}{2}}S^{\dagger} & \sqrt{2}Q \\ 0 & R^{\dagger} & S^{\dagger} & P+Q & -\sqrt{2}R^{\dagger} & -\frac{1}{\sqrt{2}}S^{\dagger} \\ -\frac{1}{\sqrt{2}}S^{\dagger} & -\sqrt{2}Q & \sqrt{\frac{3}{2}}S & -\sqrt{2}R & P+\Delta & 0 \\ \sqrt{2}R^{\dagger} & \sqrt{\frac{3}{2}}S^{\dagger} & \sqrt{2}Q & -\frac{1}{\sqrt{2}}S & 0 & P+\Delta \end{bmatrix} \begin{matrix} \left|\frac{3}{2},\frac{3}{2}\right\rangle \\ \left|\frac{3}{2},\frac{1}{2}\right\rangle \\ \left|\frac{3}{2},-\frac{1}{2}\right\rangle \\ \left|\frac{3}{2},-\frac{3}{2}\right\rangle \\ \left|\frac{1}{2},\frac{1}{2}\right\rangle \\ \left|\frac{1}{2},-\frac{1}{2}\right\rangle \end{matrix} \tag{4.34}$$

where the zone-center Bloch states are expressed as eigenfunctions of the total angular momentum and its projection onto the z-axis $\left|J,J_z\right\rangle$. The heavy hole spin up and spin down states are represented by $\left|\frac{3}{2},\pm\frac{3}{2}\right\rangle$, the light hole spin up and spin down states by $\left|\frac{3}{2},\pm\frac{3}{2}\right\rangle$, and the spin-orbit spin up and spin down states by $\left|\frac{1}{2},\pm\frac{1}{2}\right\rangle$. The explicit forms for these basis states can be found in [69]. The components of the matrix elements of the Hamiltonian are given by

$$\begin{aligned} P &= P_k + P_\varepsilon \qquad Q = Q_k + Q_\varepsilon \\ R &= R_k + R_\varepsilon \qquad S = S_k + S_\varepsilon \end{aligned}$$

$$\begin{aligned} P_k &= \left(\frac{\hbar^2}{2m_0}\right)\gamma_1\left(k_x^2+k_y^2+k_z^2\right) \\ Q_k &= \left(\frac{\hbar^2}{2m_0}\right)\gamma_2\left(k_x^2+k_y^2-2k_z^2\right) \\ R_k &= \left(\frac{\hbar^2}{2m_0}\right)\sqrt{3}\left[-\gamma_2\left(k_x^2-k_y^2\right)+2i\gamma_3 k_x k_y\right] \\ S_k &= \left(\frac{\hbar^2}{2m_0}\right)2\sqrt{3}\gamma_3\left(k_x-ik_y\right)k_z \end{aligned} \tag{4.35}$$

$$P_\varepsilon = -a_v\left(\varepsilon_{xx}+\varepsilon_{yy}+\varepsilon_{zz}\right) \qquad Q_\varepsilon = -\frac{b}{2}\left(\varepsilon_{xx}+\varepsilon_{yy}-2\varepsilon_{zz}\right)$$
$$R_\varepsilon = \frac{\sqrt{3}}{2}b\left(\varepsilon_{xx}-\varepsilon_{yy}\right)-id\varepsilon_{xy} \qquad S_\varepsilon = -d\left(\varepsilon_{xz}-i\varepsilon_{yz}\right).$$

where the wavevector **k** is interpreted as a differential operator $-i\nabla$; ε_{ij} are the components of the strain tensor; γ_i are the Luttinger inverse mass parameters; a_v, b, d, are the Pikus-Bir deformation potentials; and Δ is the spin-orbit split-off energy.

In a QW, the strain tensor has the following components:

$$\begin{aligned}\varepsilon_{xx} &= \varepsilon_{yy} = \varepsilon_0 \\ \varepsilon_{zz} &= -2\frac{C_{12}}{C_{11}}\varepsilon_0 \\ \varepsilon_{xy} &= \varepsilon_{xz} = \varepsilon_{yz} = 0\end{aligned} . \tag{4.36}$$

The hydrostatic and shear components of the strain are given by

$$\begin{aligned}P_\varepsilon &= \delta E_{hy} = -2a_v\frac{C_{11}-C_{12}}{C_{11}}\varepsilon_0 \\ Q_\varepsilon &= \frac{1}{2}\delta E_{sh} = -b\frac{C_{11}+2C_{12}}{C_{11}}\varepsilon_0\end{aligned} . \tag{4.37}$$

We also define

$$\zeta = \frac{1}{2}\delta E_{sh}. \tag{4.38}$$

Since the hydrostatic component raises or lowers the bandgap uniformly, we include the hydrostatic component in the bandgap energy so that only ζ enters the Hamiltonian in (4.34).

In general the eigenstates of the Hamiltonian in (4.34) are superpositions of the zone-center Bloch states and can be expressed as

$$\psi_{\mathbf{k}_\parallel}(\mathbf{r}) = \sum_v g^{(v)}(\mathbf{k}_\parallel,\mathbf{r})\left|v\right\rangle \tag{4.39}$$

where $\{|v\rangle\}$ are the zone-center Bloch states and $g^{(v)}(\mathbf{k}_{\parallel},\mathbf{r})$ represents the envelope function corresponding to Bloch state $|v\rangle$. The envelope functions satisfy

$$\sum_{v'}\left[H_{vv'}(-i\nabla)+V(\mathbf{r})\delta_{vv'}\right]g^{(v')}(\mathbf{k}_{\parallel},\mathbf{r})=E(\mathbf{k}_{\parallel})g^{(v')}(\mathbf{k}_{\parallel},\mathbf{r})\,. \tag{4.40}$$

4.4.2 Mathematical methods

In the following derivations we consider a rectangular lattice geometry in order to simplify the mathematics. Expressions for the triangular lattice will be given at the end of the section and can be derived in a similar manner.

In an ordinary quantum well, the in-plane components of momentum are scalars. However, in the confinement direction one must use the operator form of the momentum in the Hamiltonian given by (4.34):

$$k_z \to -i\frac{\partial}{\partial z}\,. \tag{4.41}$$

In the nanopore, the particle is confined in all three dimensions, and thus all three components of momentum must be treated as operators

$$k_x \to -i\frac{\partial}{\partial x}, k_y \to -i\frac{\partial}{\partial y}, k_z \to -i\frac{\partial}{\partial z}\,. \tag{4.42}$$

Furthermore, to ensure Hermiticity of the Hamiltonian, one must use the Hermitian forms of the operators P_k, Q_k, R_k, S_k. Since the Luttinger inverse mass parameters depend on the material, they are functions of position in the nanopore structure. Thus the operators must take the following forms:

$$\gamma(x,y,z)\frac{\partial^2}{\partial x_\alpha^2} \to \frac{\partial}{\partial x_\alpha}\gamma(x,y,z)\frac{\partial}{\partial x_\alpha} \tag{4.43}$$

$$\gamma(x,y,z)\frac{\partial}{\partial x_\alpha}\frac{\partial}{\partial x_\beta} \to \frac{1}{2}\left[\frac{\partial}{\partial x_\alpha}\gamma(x,y,z)\frac{\partial}{\partial x_\beta}+\frac{\partial}{\partial x_\beta}\gamma(x,y,z)\frac{\partial}{\partial x_\alpha}\right].$$

Using these forms of the operators and assuming a simple QW strain distribution with $Q_\varepsilon = \zeta$, $R_\varepsilon = S_\varepsilon = 0$, and P_ε incorporated into the bandgap energy, we obtain the following form of the global Hamiltonian matrix in (4.34):

$$H = -\begin{bmatrix} P_k+Q & -S_k & R_k & 0 & -\frac{1}{\sqrt{2}}S_k & \sqrt{2}R_k \\ -S_k^\dagger & P_k-Q & 0 & R_k & -\sqrt{2}Q & \sqrt{\frac{3}{2}}S_k \\ R_k^\dagger & 0 & P_k-Q & S_k & \sqrt{\frac{3}{2}}S_k^\dagger & \sqrt{2}Q \\ 0 & R_k^\dagger & S_k^\dagger & P_k+Q & -\sqrt{2}R_k^\dagger & -\frac{1}{\sqrt{2}}S_k^\dagger \\ -\frac{1}{\sqrt{2}}S_k^\dagger & -\sqrt{2}Q & \sqrt{\frac{3}{2}}S_k & -\sqrt{2}R_k & P_k+\Delta & 0 \\ \sqrt{2}R_k^\dagger & \sqrt{\frac{3}{2}}S_k^\dagger & \sqrt{2}Q & -\frac{1}{\sqrt{2}}S_k & 0 & P_k+\Delta \end{bmatrix} \begin{matrix} \left|\frac{3}{2},\frac{3}{2}\right\rangle \\ \left|\frac{3}{2},\frac{1}{2}\right\rangle \\ \left|\frac{3}{2},-\frac{1}{2}\right\rangle \\ \left|\frac{3}{2},-\frac{3}{2}\right\rangle \\ \left|\frac{1}{2},\frac{1}{2}\right\rangle \\ \left|\frac{1}{2},-\frac{1}{2}\right\rangle \end{matrix} \tag{4.44}$$

with $Q = Q_k + \zeta$ and

$$\begin{aligned} P_k &= -\left(\frac{\hbar^2}{2m_0}\right)\left(\frac{\partial}{\partial x}\gamma_1\frac{\partial}{\partial x}+\frac{\partial}{\partial y}\gamma_1\frac{\partial}{\partial y}+\frac{\partial}{\partial z}\gamma_1\frac{\partial}{\partial z}\right) \\ Q_k &= -\left(\frac{\hbar^2}{2m_0}\right)\left(\frac{\partial}{\partial x}\gamma_2\frac{\partial}{\partial x}+\frac{\partial}{\partial y}\gamma_2\frac{\partial}{\partial y}-2\frac{\partial}{\partial z}\gamma_2\frac{\partial}{\partial z}\right) \\ R_k &= -\left(\frac{\hbar^2}{2m_0}\right)\sqrt{3}\left[-\left(\frac{\partial}{\partial x}\gamma_2\frac{\partial}{\partial x}-\frac{\partial}{\partial y}\gamma_2\frac{\partial}{\partial y}\right)+i\left(\frac{\partial}{\partial x}\gamma_3\frac{\partial}{\partial y}+\frac{\partial}{\partial y}\gamma_3\frac{\partial}{\partial x}\right)\right] \\ S_k &= -\left(\frac{\hbar^2}{2m_0}\right)\sqrt{3}\left[\left(\frac{\partial}{\partial x}\gamma_3\frac{\partial}{\partial z}+\frac{\partial}{\partial z}\gamma_3\frac{\partial}{\partial x}\right)-i\left(\frac{\partial}{\partial y}\gamma_3\frac{\partial}{\partial z}+\frac{\partial}{\partial z}\gamma_3\frac{\partial}{\partial y}\right)\right] \end{aligned}. \tag{4.45}$$

Also note from (4.40) that the potential must be added to the diagonal elements of this matrix. Using the plane wave expansion approach, we express the envelope functions $g^{(v)}(\mathbf{k}_{\|},\mathbf{r})$ as

$$\begin{aligned} g^{(v)}(\mathbf{k}_{\|},\mathbf{r}) &= e^{i\mathbf{k}_{\|}\cdot\boldsymbol{\rho}} u^{v}_{\mathbf{k}\|}(\mathbf{r}) \\ &= e^{i2\pi(xk_n+yk_m)} u^{v}_{\mathbf{k}\|}(\mathbf{r}), \end{aligned} \tag{4.46}$$

where $\mathbf{k}_t$ and $\boldsymbol{\rho}$ refer to the in-plane wavevector and in-plane position vector, respectively. The function $u^{v}_{\mathbf{k}\|}(\mathbf{r})$ can be expanded in a Fourier series as the sum of reciprocal lattice vector plane waves as

$$\begin{aligned} u^{v}_{\mathbf{k}_{\|}}(\mathbf{r}) &= \sum_{i,j} a^{v}_{i,j}(\mathbf{k}_{\|}) e^{i\mathbf{G}_i\cdot\boldsymbol{\rho}} f_j(z) \\ &= \sum_{i,j} a^{v}_{i,j}(\mathbf{k}_{\|}) e^{i2\pi(n_i x+m_i y)} f_j(z), \end{aligned} \tag{4.47}$$

where $a_{i,j}$ are the Fourier coefficients of the expansion, $\mathbf{G}_i$ represents a reciprocal lattice vector, and $f_j(z)$ is a normalized function of the z-coordinate only given by

$$f_j(z) = \sqrt{\frac{2}{H}} \sin j\pi\left(\frac{1}{2}-\frac{z}{H}\right). \tag{4.48}$$

Using this plane wave expansion method, each entry in the global Hamiltonian matrix given by (4.34) becomes a submatrix with a size equal to the number of basis states used in the expansion.

As an example of the general technique, let us consider the matrix elements of the upper left corner entry of the global Hamiltonian P_k+Q. The elements of this particular submatrix are given by

$$
\begin{aligned}
H_{i,j,i',j'}^{P+Q} &= \left\langle e^{i(\mathbf{k}_{\parallel}+\mathbf{G}_{i'})\cdot\boldsymbol{\rho}} f_{j'}(z) \middle| P_k + Q \middle| e^{i(\mathbf{k}_{\parallel}+\mathbf{G}_{i})\cdot\boldsymbol{\rho}} f_j(z) \right\rangle \\
&= \left\langle e^{i(\mathbf{k}_{\parallel}+\mathbf{G}_{i'})\cdot\boldsymbol{\rho}} f_{j'}(z) \middle| P_k + Q_k + \zeta \middle| e^{i(\mathbf{k}_{\parallel}+\mathbf{G}_{i})\cdot\boldsymbol{\rho}} f_j(z) \right\rangle \\
&= \iiint_{\Omega} e^{-i(\mathbf{k}_{\parallel}+\mathbf{G}_{i'})\cdot\boldsymbol{\rho}} f_{j'}^{*}(z)(P_k + Q_k + \zeta) e^{i(\mathbf{k}_{\parallel}+\mathbf{G}_{i})\cdot\boldsymbol{\rho}} f_j(z) dV
\end{aligned}
\quad . \tag{4.49}
$$

where Ω is the volume of the unit cell. Note that this integral is complicated by the fact that the Luttinger parameters vary as a function of position. We use the same approach as in Section 4.1, in which case the spatial variations in effective mass were accounted for by dividing the integral into pieces in which the effective mass is a constant.

To illustrate the mathematics, we evaluate the term

$$
\begin{aligned}
&\iiint_{\Omega} e^{-i(\mathbf{k}_{\parallel}+\mathbf{G}_{i'})\cdot\boldsymbol{\rho}} f_{j'}^{*}(z) P_k e^{i(\mathbf{k}_{\parallel}+\mathbf{G}_{i})\cdot\boldsymbol{\rho}} f_j(z) dV \\
&= -\frac{1}{2} \iiint_{\Omega} e^{-i(\mathbf{k}_{\parallel}+\mathbf{G}_{i'})\cdot\boldsymbol{\rho}} f_{j'}^{*}(z) \left(\frac{\partial}{\partial x} \gamma_1 \frac{\partial}{\partial x} + \frac{\partial}{\partial y} \gamma_1 \frac{\partial}{\partial y} + \frac{\partial}{\partial z} \gamma_1 \frac{\partial}{\partial z} \right) e^{i(\mathbf{k}_{\parallel}+\mathbf{G}_{i})\cdot\boldsymbol{\rho}} f_j(z) dV
\end{aligned}
\tag{4.50}
$$

where we are working in units in which $\hbar^2 / m_0 = 1$. Let us start with the first term

$$
\begin{aligned}
&-\frac{1}{2} \iiint_{\Omega} e^{-i(\mathbf{k}_{\parallel}+\mathbf{G}_{i'})\cdot\boldsymbol{\rho}} f_{j'}^{*}(z) \frac{\partial}{\partial x} \gamma_1 \frac{\partial}{\partial x} e^{i(\mathbf{k}_{\parallel}+\mathbf{G}_{i})\cdot\boldsymbol{\rho}} f_j(z) dx dy dz \\
&= -\frac{1}{2} \int_{-\frac{1}{2}}^{\frac{1}{2}} \int_{-\frac{1}{2}}^{\frac{1}{2}} \int_{-\frac{L}{2}}^{\frac{L}{2}} e^{-i(\mathbf{k}_{\parallel}+\mathbf{G}_{i'})\cdot\boldsymbol{\rho}} f_{j'}^{*}(z) \partial \left[\gamma_1 \frac{\partial}{\partial x} e^{i(\mathbf{k}_{\parallel}+\mathbf{G}_{i})\cdot\boldsymbol{\rho}} f_j(z) \right] dy dz
\end{aligned}
\quad . \tag{4.51}
$$

which we can then evaluate using integration by parts as follows:

$$
\begin{aligned}
&\int_{-\frac{1}{2}}^{\frac{1}{2}} e^{-i(\mathbf{k}_{\parallel}+\mathbf{G}_{i'})\cdot\boldsymbol{\rho}} f_{j'}^{*}(z) \partial \left[\gamma_1 \frac{\partial}{\partial x} e^{i(\mathbf{k}_{\parallel}+\mathbf{G}_{i})\cdot\boldsymbol{\rho}} f_j(z) \right] \\
&= \left[uv \right]_{-1/2}^{1/2} - \int_{-1/2}^{1/2} v du
\end{aligned}
\tag{4.52}
$$

where

$$
\begin{aligned}
u &= e^{-i(\mathbf{k}_{\parallel}+\mathbf{G}_{i'})\bullet\boldsymbol{\rho}} f_{j'}^{*}(z) \\
du &= -2\pi i\left(k_n + n_{i'}\right) e^{-i(\mathbf{k}_{\parallel}+\mathbf{G}_{i'})\bullet\boldsymbol{\rho}} f_{j'}^{*}(z)dx, \\
v &= \gamma_1 \frac{\partial}{\partial x} e^{i(\mathbf{k}_{\parallel}+\mathbf{G}_{i})\bullet\boldsymbol{\rho}} f_j(z) \\
&= \gamma_1 2\pi i\left(k_n + n_i\right) e^{i(\mathbf{k}_{\parallel}+\mathbf{G}_{i})\bullet\boldsymbol{\rho}} f_j(z).
\end{aligned}
\tag{4.53}
$$

Using (4.52) in (4.51) yields

$$
\begin{aligned}
&-\frac{1}{2}\iiint_{\Omega} e^{-i(\mathbf{k}_{\parallel}+\mathbf{G}_{i'})\bullet\boldsymbol{\rho}} f_{j'}^{*}(z)\frac{\partial}{\partial x}\gamma_1\frac{\partial}{\partial x} e^{i(\mathbf{k}_{\parallel}+\mathbf{G}_{i})\bullet\boldsymbol{\rho}} f_j(z)dxdydz \\
&= -\frac{1}{2}\int_{-\frac{1}{2}}^{\frac{1}{2}}\int_{-\frac{L}{2}}^{\frac{L}{2}} \left[uv\right]_{-1/2}^{1/2} dydz + \frac{1}{2}\int_{-\frac{1}{2}}^{\frac{1}{2}}\int_{-\frac{1}{2}}^{\frac{1}{2}}\int_{-\frac{L}{2}}^{\frac{L}{2}} \left[vdu\right] dydz.
\end{aligned}
\tag{4.54}
$$

We start with the boundary integral

$$
\begin{aligned}
&-\frac{1}{2}\int_{-\frac{1}{2}}^{\frac{1}{2}}\int_{-\frac{L}{2}}^{\frac{L}{2}} \left[uv\right]_{-1/2}^{1/2} dydz \\
&= -\frac{1}{2}\int_{-\frac{1}{2}}^{\frac{1}{2}}\int_{-\frac{L}{2}}^{\frac{L}{2}} \left[e^{-i(\mathbf{k}_{\parallel}+\mathbf{G}_{i'})\bullet\boldsymbol{\rho}} f_{j'}^{*}(z)\gamma_1(x,y,z)2\pi i\left(k_n + n_i\right) e^{i(\mathbf{k}_{\parallel}+\mathbf{G}_{i})\bullet\boldsymbol{\rho}} f_j(z)\right]_{-1/2}^{1/2} dydz \\
&= -\pi i\left(k_n + n_i\right)\int_{-\frac{1}{2}}^{\frac{1}{2}}\int_{-\frac{L}{2}}^{\frac{L}{2}} \left[e^{i\pi\left(n_i - n_{i'}\right)}\gamma_1(\frac{1}{2},y,z) - e^{-i\pi\left(n_i - n_{i'}\right)}\gamma_1(-\frac{1}{2},y,z)\right] e^{i2\pi\left(m_i - m_{i'}\right)} f_{j'}^{*} f_j dydz.
\end{aligned}
\tag{4.55}
$$

This is a surface integral evaluated along the vertical faces of the unit cell determined by the equations x = -1/2, x = +1/2. Note that $\gamma_1(x,y,z)$ is a function of space on these planes, namely $\gamma_1(x,y,z) = \gamma_{1B}$ for $L/2 < z < H/2$ and $-H/2 < z < -L/2$, and $\gamma_1(x,y,z) = \gamma_{1W}$ for $-L/2 < z < L/2$ independent of the y-coordinate where B denotes barrier and W denotes quantum well. To evaluate this integral we again use the technique of dividing the integral into pieces in which γ is a constant. First, we integrate over the

entire surface with $\gamma_1(x,y,z)=\gamma_{1B}$. Next, we add the integral over the quantum well region only with $\gamma_1(x,y,z)=\gamma_{1W}-\gamma_{1B}$. The first integral with $\gamma_1(x,y,z)=\gamma_{1B}$ becomes

$$
\begin{aligned}
&-\pi i\left(k_n+n_i\right)\int_{-\frac{1}{2}}^{\frac{1}{2}}\int_{-\frac{L}{2}}^{\frac{L}{2}}\left[e^{i\pi\left(n_i-n_{i'}\right)}\gamma_1(\frac{1}{2},y,z)-e^{-i\pi\left(n_i-n_{i'}\right)}\gamma_1(-\frac{1}{2},y,z)\right]e^{i2\pi\left(m_i-m_{i'}\right)}f_{j'}^{*}f_j dydz\\
&=-\pi i\left(k_n+n_i\right)\gamma_B\int_{-\frac{1}{2}}^{\frac{1}{2}}\int_{-\frac{L}{2}}^{\frac{L}{2}}\left[e^{i\pi\left(n_i-n_{i'}\right)}-e^{-i\pi\left(n_i-n_{i'}\right)}\right]e^{i\left(m_i-m_{i'}\right)y}f_{j'}^{*}f_j dydz\\
&=-\pi i\left(k_n+n_i\right)\gamma_B\int_{-\frac{1}{2}}^{\frac{1}{2}}\int_{-\frac{L}{2}}^{\frac{L}{2}}2i\sin\left[\pi\left(n_i-n_{i'}\right)\right]e^{i\left(m_i-m_{i'}\right)y}f_{j'}^{*}f_j dydz\\
&=0.
\end{aligned}
\tag{4.56}
$$

A similar situation occurs when we evaluate the integral with $\gamma_1(x,y,z)=\gamma_{1W}-\gamma_{1B}$. Thus, the boundary term integration is identically zero.

Next, we evaluate the second integral in (4.54)

$$
\begin{aligned}
&\frac{1}{2}\int_{-\frac{1}{2}}^{\frac{1}{2}}\int_{-\frac{1}{2}}^{\frac{1}{2}}\int_{-\frac{1}{2}}^{\frac{1}{2}}\left[vdu\right]dydz\\
&=2\pi^2\left(k_n+n_i\right)\left(k_n+n_{i'}\right)\int_{-\frac{1}{2}}^{\frac{1}{2}}\int_{-\frac{1}{2}}^{\frac{1}{2}}\int_{-\frac{1}{2}}^{\frac{1}{2}}\gamma_1(x,y,z)e^{e\left(\mathbf{G}_i-\mathbf{G}_{i'}\right)\cdot\boldsymbol{\rho}}f_j(z)f_{j'}^{*}(z)dxdydz.
\end{aligned}
\tag{4.57}
$$

To evaluate this integral, we use the technique of dividing the integral into parts in which γ is a constant. First, we integrate over the entire unit cell volume with $\gamma_1=\gamma_{1B}$. Utilizing orthonormality of the basis functions this yields

$$\delta_{i,i'}\delta_{j,j'}\left[W\right]\gamma_{1B} \tag{4.58}$$

where

$$W=2\pi^2\gamma_1\left(k_n+n_i\right)\left(k_n+n_{i'}\right) \tag{4.59}$$

and the subscript in (4.58) indicates whether to use the value of γ_1 in the barrier material or in the quantum well material. Next, we integrate over the quantum well region only with $\gamma_1 = \gamma_{1W} - \gamma_{1B}$ which yields

$$\delta_{i,i'} Z \left([W]_{\gamma_{1W}} - [W]_{\gamma_{1B}} \right), \tag{4.60}$$

where

$$Z = \int_{-L/2}^{L/2} f_j(z) f_{j'}^*(z) dz,$$

which can be evaluated analytically as

$$\begin{aligned} Z = & \frac{\sin\left(j'+j\right)\frac{\pi}{2}\left(1-\frac{L}{H}\right) - \sin\left(j'+j\right)\frac{\pi}{2}\left(1+\frac{L}{H}\right)}{\pi\left(j'+j\right)} \\ & - \frac{\sin\left(j'-j\right)\frac{\pi}{2}\left(1-\frac{L}{H}\right) - \sin\left(j'-j\right)\frac{\pi}{2}\left(1+\frac{L}{H}\right)}{\pi\left(j'-j\right)} \end{aligned} \tag{4.61}$$

if $j' \neq j$, and

$$Z = \frac{L}{H} + \frac{\sin \pi j\left(1-\frac{L}{H}\right) - \sin \pi j\left(1+\frac{L}{H}\right)}{2\pi j} \tag{4.62}$$

if $j' = j$.

Finally, we integrate over the pore volume with $\gamma_1 = \gamma_{1B} - \gamma_{1W}$ which yields

$$ZU \left([W]_{\gamma_{1B}} - [W]_{\gamma_{1W}} \right), \tag{4.63}$$

where

$$
\begin{aligned}
U &= \int_0^{\rho}\int_0^{2\pi} re^{i2\pi\left[(n_i-n_{i'})x+(m_i-m_{i'})y\right]}drd\theta \\
&= 2\pi\rho\frac{J_1\left(\rho C\right)}{C}
\end{aligned}
\tag{4.64}
$$

if $C\neq 0$, and

$$
U = \pi\rho^2 \tag{4.65}
$$

if C=0 where J_1 is the Bessel function of the first kind and

$$
\begin{aligned}
C &= \sqrt{A^2+B^2} \\
A &= 2\pi\left(n_i-n_{i'}\right) \\
B &= 2\pi\left(m_i-m_{i'}\right)
\end{aligned}
\quad . \tag{4.66}
$$

Thus, the first part of the integral in (4.50) becomes

$$
\begin{aligned}
&-\frac{1}{2}\iiint_{\Omega} e^{-i(\mathbf{k}_{\parallel}+\mathbf{G}_{i'})\bullet\boldsymbol{\rho}} f_{j'}^{*}(z)\left(\frac{\partial}{\partial x}\gamma_1\frac{\partial}{\partial x}\right)e^{i(\mathbf{k}_{\parallel}+\mathbf{G}_{i})\bullet\boldsymbol{\rho}} f_j(z)dV \\
&= \delta_{i,i'}\delta_{j,j'}\left[W\right]_{\gamma_{1B}} + \delta_{i,i'}Z\left(\left[W\right]_{\gamma_{1W}}-\left[W\right]_{\gamma_{1B}}\right)+ZU\left(\left[W\right]_{\gamma_{1B}}-\left[W\right]_{\gamma_{1W}}\right),
\end{aligned}
\tag{4.67}
$$

where

$$
W = 2\pi^2\gamma_1\left(k_n+n_i\right)\left(k_n+n_{i'}\right). \tag{4.68}
$$

The expression for the y-derivative terms in (4.50) will be similar, with $k_n \to k_m$ and $n_i \to m_i$. Thus, we can take the y-derivatives into account simply by adding the appropriate terms to the expression for W:

$$
W = 2\pi^2\gamma_1\left[\left(k_n+n_i\right)\left(k_n+n_{i'}\right)+\left(k_m+m_i\right)\left(k_m+m_{i'}\right)\right]. \tag{4.69}
$$

Finally, we must account for the z-derivative terms in (4.50). The derivation of the expression for these terms follows from the integration by parts technique which has just been outlined, and we will only give the final results:

$$
\begin{aligned}
&-\frac{1}{2}\iiint_{\Omega} e^{-i(\mathbf{k}_{\parallel}+\mathbf{G}_{i'})\cdot\boldsymbol{\rho}} f_{j'}^{*}(z)\left(\frac{\partial}{\partial z}\gamma_1\frac{\partial}{\partial z}\right)e^{i(\mathbf{k}_{\parallel}+\mathbf{G}_{i})\cdot\boldsymbol{\rho}} f_{j}(z)dV \\
&=\left(\frac{\pi j}{L}\right)\left(\frac{\pi j'}{L}\right)\left[\delta_{i,i'}Z_B^{'}\gamma_{1B}+\delta_{i,i'}Z_W^{'}\left(\gamma_{1W}-\gamma_{1B}\right)+UZ_W^{'}\left(\gamma_{1B}-\gamma_{1W}\right)\right]
\end{aligned}
\tag{4.70}
$$

where

$$
Z_W^{'}=\frac{L}{2H}+\frac{1}{4\pi j}(-1)^{j}\sin\pi j\frac{L}{H} \tag{4.71}
$$

$$
Z_B^{'}=\frac{1}{2} \tag{4.72}
$$

if $j=j'$ and

$$
\begin{aligned}
Z_W^{'}=&\frac{1}{\pi\left(j-j'\right)}\cos\left[\frac{\left(j-j'\right)\pi}{2}\right]\sin\left[\frac{\left(j-j'\right)\pi}{2}\frac{L}{H}\right] \\
&+\frac{1}{\pi\left(j+j'\right)}\cos\left[\frac{\left(j+j'\right)\pi}{2}\right]\sin\left[\frac{\left(j+j'\right)\pi}{2}\frac{L}{H}\right]
\end{aligned}
\tag{4.73}
$$

$$
Z_B^{'}=0 \tag{4.74}
$$

if $j\neq j,'$ where the subscripts W or B indicate whether the integration over the z-coordinate has been performed over the quantum well region or the barrier region.

Putting all of these results together we obtain the following result for (4.50):

$$
\begin{aligned}
&\iiint_{\Omega} e^{-i(\mathbf{k}_{\parallel}+\mathbf{G}_{i'})\cdot\boldsymbol{\rho}} f_{j'}^{*}(z)P_k e^{i(\mathbf{k}_{\parallel}+\mathbf{G}_{i})\cdot\boldsymbol{\rho}} f_{j}(z)dV \\
&=\delta_{i,i'}\delta_{j,j'}\left[W\right]_{\gamma_{2B}}+\delta_{i,i'}Z\left(\left[W\right]_{\gamma_{1W}}-\left[W\right]_{\gamma_{1B}}\right)+ZU\left(\left[W\right]_{\gamma_{1B}}-\left[W\right]_{\gamma_{1W}}\right) \\
&+\left(\frac{\pi j}{L}\right)\left(\frac{\pi j'}{L}\right)\left[\delta_{i,i'}Z_B^{'}\gamma_{1B}+\delta_{i,i'}Z_W^{'}\left(\gamma_{1W}-\gamma_{1B}\right)+UZ_W^{'}\left(\gamma_{1B}-\gamma_{1W}\right)\right],
\end{aligned}
\tag{4.75}
$$

where

$$
W=2\pi^2\gamma_1\left[\left(k_n+n_i\right)\left(k_n+n_{i'}\right)+\left(k_m+m_i\right)\left(k_m+m_{i'}\right)\right]
$$

and $Z_W^{'}, Z_B^{'}$ are given by (4.71)-(4.74). A similar expression holds for the matrix elements of Q_k

$$\begin{aligned}
&\iiint_{\Omega} e^{-i(\mathbf{k}_{\parallel}+\mathbf{G}_{i'})\bullet\boldsymbol{\rho}} f_{j'}^{*}(z) Q_k e^{i(\mathbf{k}_{\parallel}+\mathbf{G}_{i})\bullet\boldsymbol{\rho}} f_j(z) dV \\
&= \delta_{i,i'}\delta_{j,j'}[W]_{\gamma_{2B}} + \delta_{i,i'} Z\left([W]_{\gamma_{2W}} - [W]_{\gamma_{2B}}\right) + ZU\left([W]_{\gamma_{2B}} - [W]_{\gamma_{2W}}\right) \\
&-2\left(\frac{\pi j}{L}\right)\left(\frac{\pi j'}{L}\right)\left[\delta_{i,i'} Z_B^{'}\gamma_{2B} + \delta_{i,i'} Z_W^{'}\left(\gamma_{2W} - \gamma_{2B}\right) + UZ_W^{'}\left(\gamma_{2B} - \gamma_{2W}\right)\right],
\end{aligned} \tag{4.76}$$

where we have simply replaced $\gamma_1 \to \gamma_2$ and multiplied the *z*-derivative term by -2 as in (4.45). For the diagonal elements of the global Hamiltonian we must also add the contribution of the potential $V(x, y, z)$. The zero of potential energy is chosen to be the position of the unstrained band edge. Thus, the potential in the quantum well for holes is shifted for all bands (light hole, heavy hole, and spin orbit) by the hydrostatic strain given in (4.37), while the potential in the barrier is $\Delta E_v = 0.4\Delta E_g$, where ΔE_g is the difference between GaAs and InGaAs bandgaps. The derivation of the matrix elements of the potential is similar to the derivation in (4.25) from which we obtain

$$\delta_{i,i'}\delta_{j,j'} V_{0b} + \delta_{i,i'} Z\left(V_{0w} - V_{0b}\right) + \left(V_{0b} - V_{0w}\right) ZU, \tag{4.77}$$

where

$$V_{0w} = -2a_v \frac{C_{11} - C_{12}}{C_{11}} \varepsilon_0 \tag{4.78}$$

and

$$V_{0b} = \Delta E_v . \tag{4.79}$$

Finally, we must take into account the matrix elements of the shear strain, which splits the degeneracy of the heavy and light hole bands at zone-center. The shear strain is a function of space, and is equal to

$$\zeta = \frac{1}{2}\delta E_{sh} = -b\frac{C_{11}+2C_{12}}{C_{11}}\varepsilon_0 \tag{4.80}$$

in the quantum well and zero in the barriers. Thus the matrix elements are given by

$$\delta_{i,i'}Z\zeta - ZU\zeta\ . \tag{4.81}$$

Combining (4.75)-(4.77), and (4.81), we obtain the following expression for the upper left submatrix of the global Hamiltonian:

$$\begin{aligned}
H^{11}_{i,j,i',j'} &= \iiint_{\Omega} e^{-i(\mathbf{k}_{\parallel}+\mathbf{G}_{i'})\cdot\boldsymbol{\rho}} f^{*}_{j'}(z)(P_k+Q_k+\zeta+V)e^{i(\mathbf{k}_{\parallel}+\mathbf{G}_{i})\cdot\boldsymbol{\rho}} f_j(z)dV \\
&= \delta_{i,i'}\delta_{j,j'}\left[W^{11}\right]_{\gamma_B} + \delta_{i,i'}Z\left(\left[W^{11}\right]_{\gamma_W} - \left[W^{11}\right]_{\gamma_B}\right) + ZU\left(\left[W^{11}\right]_{\gamma_B} - \left[W^{11}\right]_{\gamma_W}\right) \\
&+ \left(\frac{\pi j}{L}\right)\left(\frac{\pi j'}{L}\right)\Big[\delta_{i,i'}Z'_B\left(\gamma_{1B}-2\gamma_{2B}\right) + \delta_{i,i'}Z'_W\left[\left(\gamma_{1W}-\gamma_{1B}\right)-2\left(\gamma_{2W}-\gamma_{2B}\right)\right] \\
&+ UZ'_W\left[\left(\gamma_{1B}-\gamma_{1W}\right)-2\left(\gamma_{2B}-\gamma_{2W}\right)\right]\Big] + \delta_{i,i'}\delta_{j,j'}V_{0b} + \delta_{i,i'}Z\left(V_{0w}-V_{0b}\right) + \left(V_{0b}-V_{0w}\right)ZU \\
&+ \delta_{i,i'}Z\zeta - ZU\zeta
\end{aligned} \tag{4.82}$$

where

$$W^{11} = 2\pi^2\left(\gamma_1+\gamma_2\right)\left[\left(k_n+n_i\right)\left(k_n+n_{i'}\right)+\left(k_m+m_i\right)\left(k_m+m_{i'}\right)\right], \tag{4.83}$$

and Z is given by (4.61)-(4.62), and Z'_W and Z'_B are given by (4.71)-(4.74).

This analysis must be performed for each element of the global Hamiltonian in (4.44). Due to the Hermiticity of (4.44) we only need the submatrices H^{11}, H^{22}, H^{55}, H^{12}, H^{13}, and H^{25} from which we can construct the rest of the global Hamiltonian. The mathematical techniques outlined in this section are very similar for the evaluation of all of these matrix elements, and we show only the final results here:

$$
\begin{aligned}
H^{22}_{i,j,i',j'} &= \delta_{i,i'}\delta_{j,j'}\left[W^{22}\right]_{\gamma_B} + \delta_{i,i'}Z\left(\left[W^{22}\right]_{\gamma_W} - \left[W^{22}\right]_{\gamma_B}\right) + ZU\left(\left[W^{22}\right]_{\gamma_B} - \left[W^{22}\right]_{\gamma_W}\right) \\
&+ \left(\frac{\pi j}{L}\right)\left(\frac{\pi j'}{L}\right)\left[\delta_{i,i'}Z'_B\left(\gamma_{1B} + 2\gamma_{2B}\right) + \delta_{i,i'}Z'_W\left[\left(\gamma_{1W} - \gamma_{1B}\right) + 2\left(\gamma_{2W} - \gamma_{2B}\right)\right]\right. \\
&\left. + UZ'_W\left[\left(\gamma_{1B} - \gamma_{1W}\right) + 2\left(\gamma_{2B} - \gamma_{2W}\right)\right]\right] + \delta_{i,i'}\delta_{j,j'}V_{0b} + \delta_{i,i'}Z\left(V_{0w} - V_{0b}\right) + \left(V_{0b} - V_{0w}\right)ZU \\
&- \delta_{i,i'}Z\zeta + ZU\zeta
\end{aligned}
\tag{4.84}
$$

$$
W^{22} = 2\pi^2\left(\gamma_1 - \gamma_2\right)\left[\left(k_n + n_i\right)\left(k_n + n_{i'}\right) + \left(k_m + m_i\right)\left(k_m + m_{i'}\right)\right]
$$

$$
\begin{aligned}
H^{55}_{i,j,i',j'} &= \delta_{i,i'}\delta_{j,j'}\left[W^{55}\right]_{\gamma_B} + \delta_{i,i'}Z\left(\left[W^{55}\right]_{\gamma_W} - \left[W^{55}\right]_{\gamma_B}\right) + ZU\left(\left[W^{55}\right]_{\gamma_B} - \left[W^{55}\right]_{\gamma_W}\right) \\
&+ \left(\frac{\pi j}{L}\right)\left(\frac{\pi j'}{L}\right)\left[\delta_{i,i'}Z'_B\gamma_{1B} + \delta_{i,i'}Z'_W\left(\gamma_{1W} - \gamma_{1B}\right) + UZ'_W\left(\gamma_{1B} - \gamma_{1W}\right)\right] \\
&+ \delta_{i,i'}\delta_{j,j'}V_{0b} + \delta_{i,i'}Z\left(V_{0w} - V_{0b}\right) + \left(V_{0b} - V_{0w}\right)ZU \\
&+ \delta_{i,i'}\delta_{j,j'}\Delta_B + \delta_{i,i'}Z\left(\Delta_W - \Delta_B\right) + \left(\Delta_B - \Delta_W\right)ZU
\end{aligned}
\tag{4.85}
$$

$$
W^{55} = 2\pi^2\left(\gamma_1 - \gamma_2\right)\left[\left(k_n + n_i\right)\left(k_n + n_{i'}\right) + \left(k_m + m_i\right)\left(k_m + m_{i'}\right)\right],
$$

where Δ_B is the spin-orbit split-off energy in the barrier material and Δ_W is the spin-orbit split-off energy in the quantum well.

$$
\begin{aligned}
H^{12}_{i,j,i',j'} &= \delta_{i,i'}\left\{Z'_{B1}\left[W^{12}_1\right]_{\gamma_B} + Z'_{B2}\left[W^{12}_2\right]_{\gamma_B} + Z'_{QW1}\left(\left[W^{12}_1\right]_{\gamma_W} - \left[W^{12}_1\right]_{\gamma_B}\right)\right. \\
&\left. + Z'_{QW2}\left(\left[W^{12}_2\right]_{\gamma_W} - \left[W^{12}_2\right]_{\gamma_B}\right)\right\} + UZ'_{QW1}\left(\left[W^{12}_1\right]_{\gamma_B} - \left[W^{12}_1\right]_{\gamma_W}\right) \\
&+ UZ'_{QW2}\left(\left[W^{12}_2\right]_{\gamma_B} - \left[W^{12}_2\right]_{\gamma_W}\right)
\end{aligned}
\tag{4.86}
$$

$$
\begin{aligned}
W^{12}_1 &= -\pi i\sqrt{3}\gamma_3\left(\frac{j\pi}{L}\right)\left[\left(k_n + n_{i'}\right) - i\left(k_m + m_{i'}\right)\right] \\
W^{12}_2 &= \pi i\sqrt{3}\gamma_3\left(\frac{j'\pi}{L}\right)\left[\left(k_n + n_i\right) - i\left(k_m + m_i\right)\right]
\end{aligned}
$$

and

$$Z'_{B1} = Z'_{QW1} = Z'_{B2} = Z'_{QW2} = 0 \tag{4.87}$$

if $j=j'$

$$Z'_{B1} = \frac{1-(-1)^{(j'+j)}}{\pi(j'+j)} + \frac{1-(-1)^{(j'-j)}}{\pi(j'-j)} \tag{4.88}$$

$$\begin{aligned} Z'_{QW1} = & \frac{2}{\pi(j'+j)} \sin\left[\frac{(j'+j)\pi}{2}\right] \sin\left[\frac{(j'+j)\pi}{2}\frac{L}{H}\right] \\ & + \frac{2}{\pi(j'-j)} \sin\left[\frac{(j'-j)\pi}{2}\right] \sin\left[\frac{(j'-j)\pi}{2}\frac{L}{H}\right] \end{aligned} \tag{4.89}$$

$$Z'_{B2} = \frac{1-(-1)^{(j+j')}}{\pi(j+j')} + \frac{1-(-1)^{(j-j')}}{\pi(j-j')} \tag{4.90}$$

$$\begin{aligned} Z'_{QW2} = & \frac{2}{\pi(j+j')} \sin\left[\frac{(j+j')\pi}{2}\right] \sin\left[\frac{(j+j')\pi}{2}\frac{L}{H}\right] \\ & + \frac{2}{\pi(j-j')} \sin\left[\frac{(j-j')\pi}{2}\right] \sin\left[\frac{(j-j')\pi}{2}\frac{L}{H}\right] \end{aligned} \tag{4.91}$$

if $j \neq j'$.

$$H^{13}_{i,j,i',j'} = \delta_{i,i'}\delta_{j,j'}\left[W^{13}\right]_{\gamma_B} + \delta_{i,i'}Z\left(\left[W^{13}\right]_{\gamma_W} - \left[W^{13}\right]_{\gamma_B}\right) + ZU\left(\left[W^{13}\right]_{\gamma_B} - \left[W^{13}\right]_{\gamma_W}\right) \tag{4.92}$$

$$\begin{aligned} W^{13} = & 2\pi^2\sqrt{3}\left\{\gamma_2\left[-(k_n+n_i)(k_n+n_{i'}) + (k_m+m_i)(k_m+m_{i'})\right]\right. \\ & \left. + i\gamma_3\left[(k_n+n_{i'})(k_m+m_i) + (k_m+m_{i'})(k_n+n_i)\right]\right\} \end{aligned}$$

$$\begin{aligned} H^{25}_{i,j,i',j'} = & -\sqrt{2}\left\{\delta_{i,i'}\delta_{j,j'}\left[W^{25}\right]_{\gamma_B} + \delta_{i,i'}Z\left(\left[W^{25}\right]_{\gamma_W} - \left[W^{25}\right]_{\gamma_B}\right)\right. \\ & + ZU\left(\left[W^{25}\right]_{\gamma_B} - \left[W^{25}\right]_{\gamma_W}\right) - 2\left(\frac{\pi j}{L}\right)\left(\frac{\pi j'}{L}\right)\left[\delta_{i,i'}Z'_B\gamma_{2B} + \delta_{i,i'}Z'_W\left(\gamma_{2W} - \gamma_{2B}\right)\right. \\ & \left.\left. + UZ'_W\left(\gamma_{2B} - \gamma_{2W}\right)\right] + \delta_{i,i'}Z\zeta - ZU\zeta\right\} \end{aligned} \tag{4.93}$$

$$W^{25} = 2\pi^2\gamma_2\left[(k_n+n_i)(k_n+n_{i'}) + (k_m+m_i)(k_m+m_{i'})\right].$$

4.5 Intersubband Transitions

The utilization of intersubband transitions in semiconductor structures has, in recent years, led to the development of a wide range of far-infrared devices suitable for applications ranging from spectroscopy to imaging. The design of these structures depends critically on numerical modeling and a detailed understanding of the physics of intersubband transitions.

The quantum well infrared photodetector (QWIP) is the most well-developed of the intersubband devices [78], although the TM-polarization limitation has instigated the search for other alternatives sensitive to infrared radiation at normal incidence [79]. One alternative which has been explored recently is semiconductor quantum dots (QDs) [80, 81], which due to in-plane quantization effects possess a nonzero in-plane component of the dipole moment [82-85]. This has been shown to lead to infrared detection at normal incidence to the semiconductor surface, which greatly simplifies the fabrication and design of quantum dot infrared photodetectors (QDIPs). However, the introduction of QDs as the absorption medium also results in additional problems such as reduction of peak absorption due to inhomogeneous broadening, and reduced absorption volume due to low QD density. The issue of low absorption volume is typically overcome by stacking QD layers [86]. However, inhomogeneous broadening remains a problem for devices fabricated using self-assembled QDs [80].

In this section we examine the possible use of the nanopore active layer in intersubband devices, which would have the potential to be used in both infrared and terahertz applications. In Section 4.5.1 we describe the basic physics of intersubband absorption in an IQD array, including the dipole moment and oscillator strength. In Section 4.5.2 we provide an example to illustrate that through appropriate simulation and

design, the nanopore array can be tailored to provide for polarization-dependent terahertz or infrared absorption, which is not possible with traditional QWIP or QDIP devices. Finally, in Section 4.5.3 we conclude by deriving a sum rule for the nanopore structure.

4.5.1 Intersubband physics in a nanopore array

We begin by reviewing the quantum mechanics of intersubband transitions in a bounded system such as a semiconductor QW in which the electron wavefunction decays to zero infinitely far from the well. The strength of an optical transition is typically characterized by the dipole matrix element between the initial and final states. Since a dimensionless quantity is more useful for making comparisons in different systems, the oscillator strength is often used instead of the dipole matrix element. The oscillator strength is defined through the $\mathbf{A} \cdot \mathbf{p}$ term in the Hamiltonian describing the interaction between the electron and the electromagnetic field as

$$f_{n'n} = \frac{2}{m\hbar\omega_{n'n}} \left| \langle n' | \mathbf{p} | n \rangle \right|^2 , \tag{4.94}$$

where $\omega_{n'n} = E_{n'n} / \hbar = (E_{n'} - E_n) / \hbar$ is the frequency corresponding to the energy difference between the initial and final states [87]. The more common position operator form of the oscillator strength can be obtained from the commutation relation

$$\mathbf{p} = im / \hbar [H, \mathbf{r}] . \tag{4.95}$$

In the following we will introduce dimensionless units by making the transformations $\mathbf{r} \rightarrow a_0\, \mathbf{r}$ and $\mathbf{p} \rightarrow \hbar\mathbf{p}/a_0$, where energy is now normalized to $E_0 = \hbar^2 / m a_0^2$ and a_0 is a fundamental length which in the case of the nanopore array lattice will be the size of the unit cell.

In these normalized units, (4.95) becomes

$$\mathbf{p} = i[H, \mathbf{r}]. \tag{4.96}$$

This commutator yields the following relationship between the momentum and position operator forms of the dipole matrix element:

$$\langle n'|\mathbf{p}|n\rangle = iE_{n'n}\langle n'|\mathbf{r}|n\rangle. \tag{4.97}$$

Using (4.97) in (4.94) we obtain the more commonly used position operator form of the oscillator strength

$$f_{n'n} = \frac{2m\omega_{n'n}}{\hbar}\left|\langle n'|\mathbf{r}|n\rangle\right|^2. \tag{4.98}$$

In addition, the oscillator strengths satisfy the *f*-sum rule

$$\sum_{n'} f_{n'n} = 1. \tag{4.99}$$

This rule can be derived by considering the commutator $i[p_x,x] = 1$ from which we obtain

$$\begin{aligned} 1 &= i\langle n|[p_x, x]|n\rangle \\ &= i\sum_{n'}\left[\langle n|p_x|n'\rangle\langle n'|x|n\rangle - \langle n|x|n'\rangle\langle n'|p_x|n\rangle\right] \\ &= 2\sum_{n'}\mathrm{Im}\langle n'|p_x|n\rangle\langle n'|x|n\rangle^* = \sum_{n'} f_{n'n}. \end{aligned} \tag{4.100}$$

In a quantum well, the electron wavefunctions have the form

$$\psi(\mathbf{r}) = \frac{e^{i\mathbf{k}_t\cdot\boldsymbol{\rho}}}{\sqrt{A}}\varphi(z), \tag{4.101}$$

where $\mathbf{k_t} = k_x\hat{\mathbf{x}} + k_y\hat{\mathbf{y}}$, $\boldsymbol{\rho} = x\hat{\mathbf{x}} + y\hat{\mathbf{y}}$, and

$$\varphi(z) = \sqrt{\frac{2}{L}}\sin\left(\frac{n\pi z}{L}\right), \tag{4.102}$$

where L is the width of the QW [69]. The dipole moment between initial and final states is given by

$$
\begin{aligned}
\boldsymbol{\mu}_{ba} &= \langle \psi_b | \mathbf{r} | \psi_a \rangle \\
&= \left\langle \frac{e^{i\mathbf{k}_t' \cdot \boldsymbol{\rho}}}{\sqrt{A}} \varphi_b(z) \middle| \mathbf{r} \middle| \frac{e^{i\mathbf{k}_t \cdot \boldsymbol{\rho}}}{\sqrt{A}} \varphi_a(z) \right\rangle \\
&\simeq \delta_{\mathbf{k}_t, \mathbf{k}_t'} \langle \varphi_b | z | \varphi_a \rangle \hat{\mathbf{z}}.
\end{aligned}
\tag{4.103}
$$

Since the optical absorption coefficient is proportional to $|\hat{\mathbf{e}} \cdot \boldsymbol{\mu}_{ba}|^2$ where $\hat{\mathbf{e}}$ is the polarization direction of the electromagnetic field, the polarization of the dipole moment along the $\hat{\mathbf{z}}$ direction implies that TM polarized light will be most strongly absorbed while TE polarized light will not be absorbed at all. This is the well-known TM limitation of QWIP devices.

To analyze the intersubband transitions in a nanopore array, we take a numerical approach similar to that outlined in [88]. To simplify the mathematics, we will consider the general case of a rectangular unit cell instead of a triangular unit cell. All lengths will be normalized to the size of the unit cell in the $\hat{\mathbf{x}}$ direction denoted by *a*, and we define an asymmetry factor β as the ratio of the size of the unit cell in the $\hat{\mathbf{x}}$ direction *a* to the size of the unit cell in the $\hat{\mathbf{y}}$ direction denoted by *b*. In these normalized coordinates the position vector, in-plane momentum vector, and reciprocal space basis vectors take the form

$$
\boldsymbol{\rho} = x\hat{\mathbf{x}} + y\hat{\mathbf{y}} \,, \tag{4.104}
$$

$$
\mathbf{k}_t = k_x \hat{\mathbf{x}} + \beta k_y \hat{\mathbf{y}} \,, \tag{4.105}
$$

and

$$
\mathbf{G} = 2\pi l \hat{\mathbf{x}} + 2\pi \beta m \hat{\mathbf{y}} \,, \tag{4.106}
$$

respectively, where *l*, *m* are integers. We represent the wavefunctions as the product of a plane wave and a periodic envelope as

$$\psi(u,v,z) = \sqrt{\beta} e^{i\mathbf{k}_t \cdot \boldsymbol{\rho}} u_{\mathbf{k}_t}(u,v,z)$$
$$= \sqrt{\beta} e^{i2\pi(xk_x + \beta y k_y)} u_{\mathbf{k}_t}(u,v,z), \tag{4.107}$$

where

$$u_{\mathbf{k}_t}(u,v,z) = \sum_{i,j} a_{i,j}(\mathbf{k}_t) e^{i\mathbf{G}_i \cdot \boldsymbol{\rho}} f_j(z)$$
$$= \sum_{i,j} a_{i,j}(\mathbf{k}_t) e^{i2\pi(l_i x + m_i \beta y)} f_j(z), \tag{4.108}$$

and

$$f_j(z) = \sqrt{\frac{2}{H}} \sin j\pi \left(\frac{1}{2} - \frac{z}{H} \right). \tag{4.109}$$

Due to the fact that the nanopore array is a periodic unbounded structure, we must use the momentum matrix form of the oscillator strength instead of the more common position operator form [89]. This is the direct result of the position operator being a non-periodic function. In order to compute the oscillator strength, we first compute the momentum matrix element using Eqs. (4.107) - (4.109)

$$\mathbf{p}_{ba} = \delta_{\mathbf{k}_t, \mathbf{k}_t'} \left\langle u_{\mathbf{k}_t'}(u,v,z) \middle| \mathbf{p} \middle| u_{\mathbf{k}_t}(u,v,z) \right\rangle$$
$$= \left(p_{\hat{\mathbf{x}}} \hat{\mathbf{x}} + p_{\hat{\mathbf{y}}} \hat{\mathbf{y}} + p_{\hat{\mathbf{z}}} \hat{\mathbf{z}} \right) \delta_{\mathbf{k}_t, \mathbf{k}_t'}. \tag{4.110}$$

Performing this integration, one obtains generalized expressions for the three components of the momentum matrix element in terms of the coefficients of the plane wave expansion in Eq. (4.108):

$$p_{\hat{\mathbf{x}}} = 2\pi \sum_{\substack{i=i' \\ j=j'}} l_i a_{i',j'}^* a_{i,j} \tag{4.111}$$

$$p_{\hat{\mathbf{y}}} = 2\pi\beta \sum_{\substack{i=i' \\ j=j'}} m_i a_{i',j'}^* a_{i,j} \tag{4.112}$$

$$p_{\hat{\mathbf{z}}} = \frac{i}{H} \sum_{\substack{i=i' \\ j \neq j'}} j a_{i',j'}^{*} a_{i,j} \left[\frac{1-(-1)^{(j'-j)}}{(j'-j)} + \frac{1-(-1)^{(j'+j)}}{(j'+j)} \right]. \tag{4.113}$$

Note that, in general, the in-plane components of the matrix element may be nonzero, implying that absorption of TE-polarized light is allowed in a nanopore array. Furthermore, the $\hat{\mathbf{x}}$ and $\hat{\mathbf{y}}$ polarized components depend on the details of the nanopore array geometry. Thus one can in principle control the polarization dependence of intersubband absorption through appropriate design of the array geometry. These features are unique to the nanopore array, and cannot be obtained from an ordinary QW or QDs.

In general, the momentum matrix elements and hence the oscillator strengths for intersubband transitions given by Eq. (4.94) will be a function of the in-plane momentum vector $\mathbf{k}_t$, and will vary across the Brillouin zone. This is the result of the fact that the oscillator strength depends strongly on the symmetries of the electron wavefunction in the initial and final subbands, which will be a function of in-plane momentum vector. Variations in oscillator strength across the Brillouin zone must be taken into account when calculating the intersubband absorption spectrum, since all points in the Brillouin zone will not contribute equally to the absorption.

To better illustrate this fact, we consider the special case of a nanopore square lattice with 80 nm pitch and 40 nm diameter pores. Figure 4.13 shows the first three energy subbands of the conduction bandstructure computed for this nanopore array geometry. For simplicity we consider intersubband transitions between the first and second subbands and first and third subbands only. Figure 4.14 shows the oscillator strength for absorption on the 1-2 intersubband transition as a function of in-plane momentum across the Brillouin zone. Note that for light polarized along the $\hat{\mathbf{x}}$ axis, only

states having a large k_x component of momentum contribute significantly to absorption. Likewise, for light polarized along the $\hat{\mathbf{y}}$ axis, only states having a large k_y component of momentum contribute significantly to absorption. Figure 4.15 shows the oscillator strength for absorption on the 1-3 intersubband transition. In this case both polarizations experience the strongest absorption for intersubband transitions at the four corners of the Brillouin zone. As demonstrated here, the nature of the variations in oscillator strength across the Brillouin zone will depend on both the initial and final subbands.

4.5.2 Polarization dependence of intersubband absorption

As demonstrated in the previous section, the oscillator strength depends strongly on the symmetries of the initial and final subband wavefunctions. In this section, we demonstrate that by adjusting the asymmetry factor $\beta = a/b$ of the nanopore array unit cell, we can tune the polarization dependence and oscillator strengths of these transitions. For simplicity we will be considering intersubband transitions only at the center or Γ point of the Brillouin zone.

Figure 4.16 shows a plot of the $\hat{\mathbf{y}}$ component of the oscillator strength denoted by f_y as a function of the asymmetry factor β. The value of β was varied by decreasing the lattice constant in the $\hat{\mathbf{x}}$ direction and keeping the lattice constant in the $\hat{\mathbf{y}}$ direction fixed at 80 nm. The plot for the $\hat{\mathbf{x}}$ component of the oscillator strength is not shown because it is nonzero and equal to f_y only for the 1-3 transition and $\beta = 1$.

For $\beta = 1$, note that only the 1-3 transition is allowed with $f_y = f_x = 0.1$. Reducing the value of β by shrinking the unit cell along the $\hat{\mathbf{x}}$ direction results in a breaking of the unit cell symmetry. This, in turn, results in a significant shift in the symmetry of the third

subband wavefunction as shown in Fig. 4.17, while the symmetry of the first subband wavefunction remains largely unaffected. Since the oscillator strength depends on the initial and final subband wavefunctions through Eq. (4.110), the $\hat{\mathbf{x}}$ component of the oscillator strength becomes zero, with a corresponding increase in the magnitude of the $\hat{\mathbf{y}}$ component as shown in Fig. 4.16. Thus, for a nanopore array lattice with $0.85 < \beta < 1$, absorption will only occur on the 1-3 transition for light polarized along the $\hat{\mathbf{y}}$ direction.

As we continue to reduce the symmetry of the unit cell by decreasing β, we find that for $\beta \approx 0.85$ both the third and second subband wavefunctions undergo another change in symmetry as shown in Figs. 4.17 and 4.18, respectively. This results in $f_x = f_y = 0$ for the third subband transition and for $\beta < 0.85$, and thus the 1-3 intersubband transition becomes completely disallowed independent of the polarization of the incident light. However, while the 1-3 transition becomes disallowed, the 1-2 transition becomes allowed, with $f_y = 0.5$ and $f_x = 0$. The magnitude of f_y for the 1-2 transition continues to increase as the symmetry of the unit cell is reduced further until $f_y \approx 0.75$ for $\beta = 0.5$. This example illustrates that the nanopore array provides the unique ability to tune the magnitude and polarization dependence of the intersubband absorption spectrum by controlling the geometry of the unit cell.

4.5.3 Sum rule

In order to obtain a sum rule for intersubband transitions in a nanopore array analogous to Eq. (4.99), we take an approach similar to that outlined in [89]. The Schrödinger equation can be written as

$$\left[-\frac{1}{2m^*}\nabla^2+\left[V(\mathbf{r})-E_{n,\mathbf{k}}\right]\right]\psi_{n,\mathbf{k}}(\mathbf{r})=0, \tag{4.114}$$

where

$$\psi_{n,\mathbf{k}}=e^{i\mathbf{k}\cdot\boldsymbol{\rho}}u_{n,\mathbf{k}}(\mathbf{r}) \tag{4.115}$$

and n is a subband index. Performing the derivatives in Eq. (4.114) one obtains a simplified form of the Hamiltonian which operates only on the periodic part of the wavefunction

$$\left[H(\mathbf{k})-E_{n,\mathbf{k}}\right]u_{n,\mathbf{k}}=0, \tag{4.116}$$

where

$$H(\mathbf{k})=-\frac{1}{2m^*}\left[\left(\frac{\partial^2}{\partial x^2}+\frac{\partial^2}{\partial y^2}\right)+2i\left(k_x\frac{\partial}{\partial x}+\beta k_y\frac{\partial}{\partial y}\right)-\left(k_x^2+\beta^2k_y^2\right)-\left(\frac{j\pi}{H}\right)^2\right]+V(\mathbf{r}). \tag{4.117}$$

Again, due to the unbounded nature of the wavefunctions in the nanopore array, the position operator is not well defined, and Eqs. (4.97) - (4.100) do not hold. In order to correct this, we introduce a periodic position operator as in [89] consisting of the repetition of the sawlike function $q(x)=x\theta(1/2-x)$ where $\theta(x)$ is the step function defined by

$$\theta(x)=\begin{cases}1 & (x\geq 0)\\ 0 & (x<0)\end{cases}. \tag{4.118}$$

A similar operator $q(y)=y\theta(1/2-y)$ can be defined along the $\hat{\mathbf{y}}$ dimension. In order to find the relationship between the momentum operator matrix element and periodic position operator matrix element analogous to that in Eq. (4.97), we compute the commutator of $H(\mathbf{k})$ with $q(x)$

$$\left[H(\mathbf{k}),q(x)\right]=-\frac{1}{m^*}\left(\frac{\partial}{\partial x}+ik_x\right)+\frac{1}{m^*}\delta\left(x+\frac{1}{2}\right)\left(\frac{\partial}{\partial x}+ik_x\right)+\frac{1}{2m^*}\dot{\delta}\left(x+\frac{1}{2}\right). \quad (4.119)$$

Taking the matrix element of both sides of Eq. (4.119) yields

$$iE_{n'n}(\mathbf{k})\left\langle n',\mathbf{k}\middle|x\middle|n,\mathbf{k}\right\rangle=\left\langle n',\mathbf{k}\middle|p_x\middle|n,\mathbf{k}\right\rangle+\delta_{n'n}k_x+w^x_{n'n}(\mathbf{k}), \quad (4.120)$$

where

$$\begin{aligned} w^x_{n'n}(\mathbf{k})=&\left(\frac{1}{m^*_w}-1\right)\left[\left\langle n',\mathbf{k}\middle|p_x+k_x\middle|n,\mathbf{k}\right\rangle_{QW}-\left\langle n',\mathbf{k}\middle|p_x+k_x\middle|n,\mathbf{k}\right\rangle_{Pore}\right]\\ &-\left\langle n',\mathbf{k}\middle|\frac{1}{m^*}\delta\left(x+\frac{1}{2}\right)(p_x+k_x)\middle|n,\mathbf{k}\right\rangle+i\left\langle n',\mathbf{k}\middle|\frac{1}{2m^*}\dot{\delta}\left(x+\frac{1}{2}\right)\middle|n,\mathbf{k}\right\rangle. \end{aligned} \quad (4.121)$$

When taking the matrix elements of Eq. (4.119), the position dependence of the effective mass must be taken into account. To do this we take an approach similar to that outlined in [89] in which the integrations are separated into regions in which the effective mass is constant. In the expression for $w^x_{n'n}(\mathbf{k})$, the subscripts *QW* and *Pore* in the first two terms $\left\langle n',\mathbf{k}\middle|p_x+k_x\middle|n,\mathbf{k}\right\rangle_{QW}$ and $\left\langle n',\mathbf{k}\middle|p_x+k_x\middle|n,\mathbf{k}\right\rangle_{Pore}$ are the result of the position dependence of the effective mass, and indicate that the integration is to be performed over the entire quantum well plane of the unit cell or the cylindrical pore region of the unit cell, respectively.

To derive the sum rule we consider the commutator

$$i\left[p_x,q(x)\right]=1-\delta\left(x+\frac{1}{2}\right) \quad (4.122)$$

which has corresponding matrix element

$$i\langle n,\mathbf{k}|\left[p_x,q(x)\right]|n,\mathbf{k}\rangle = i\sum_{n'}\left\{\langle n,\mathbf{k}|p_x|n',\mathbf{k}\rangle\langle n',\mathbf{k}|x|n,\mathbf{k}\rangle - \langle n,\mathbf{k}|x|n',\mathbf{k}\rangle\langle n',\mathbf{k}|p_x|n,\mathbf{k}\rangle\right\}$$

$$= -i\sum_{n'\neq n}\left\{\langle n',\mathbf{k}|p_x|n,\mathbf{k}\rangle\langle n',\mathbf{k}|x|n,\mathbf{k}\rangle^* - \langle n',\mathbf{k}|p_x|n,\mathbf{k}\rangle^*\langle n',\mathbf{k}|x|n,\mathbf{k}\rangle\right\}$$

$$= 1 - \int_{-\frac{1}{2}}^{\frac{1}{2}}\int_{-\frac{H}{2}}^{\frac{H}{2}}\left|u_{n,k}\left(-\frac{1}{2},y,z\right)\right|^2 dydz \tag{4.123}$$

from which we obtain

$$2\sum_{n'\neq n}\mathrm{Im}\left\{\langle n',\mathbf{k}|p_x|n,\mathbf{k}\rangle\langle n',\mathbf{k}|x|n,\mathbf{k}\rangle^*\right\} = 1 - \int_{-\frac{1}{2}}^{\frac{1}{2}}\int_{-\frac{H}{2}}^{\frac{H}{2}}\left|u_{n,k}\left(-\frac{1}{2},y,z\right)\right|^2 dydz. \tag{4.124}$$

In order to express this sum rule in terms of the oscillator strengths, we use Eq. (4.120) and solve for $\langle n',\mathbf{k}|x|n,\mathbf{k}\rangle$ in terms of $\langle n',\mathbf{k}|p_x|n,\mathbf{k}\rangle$

$$\langle n',\mathbf{k}|x|n,\mathbf{k}\rangle = \frac{\langle n',\mathbf{k}|p_x|n,\mathbf{k}\rangle + \delta_{n'n}k_x + w^x_{n'n}(\mathbf{k})}{iE_{n'n}(\mathbf{k})}. \tag{4.125}$$

Using this expression in Eq. (4.124) yields

$$\sum_{n'\neq n} f^x_{n'n} = 1 - \int_{-\frac{1}{2}}^{\frac{1}{2}}\int_{-\frac{H}{2}}^{\frac{H}{2}}\left|u_{n,k}\left(-\frac{1}{2},y,z\right)\right|^2 dydz - 2\,\mathrm{Im}\sum_{n'\neq n} i\left\{\frac{\langle n',\mathbf{k}|p_x|n,\mathbf{k}\rangle w^{x*}_{n'n}(\mathbf{k})}{E_{n'n}(\mathbf{k})}\right\}. \tag{4.126}$$

Note that the $\delta_{n'n}k_x$ term does not contribute to the sum since the sum is taken only over $n'\neq n$. A similar expression applies for the $\hat{\mathbf{y}}$ component of the oscillator strength. Expressions for the various terms in Eq. (4.126) can be obtained in terms of the coefficients of the plane wave expansion in Eq. (4.108), and are given in the Section 4.5.5. These expressions are useful in numerical computations, since they reduce the

number of integrations which must be performed. The total oscillator strength is given by the sum of the $\hat{\mathbf{x}}$ and $\hat{\mathbf{y}}$ components as

$$\sum_{n'\neq n} f_{n'n}(\mathbf{k}) = 2 - \int_{-\frac{1}{2}}^{\frac{1}{2}}\int_{-\frac{H}{2}}^{\frac{H}{2}} \left| u_{n,k}\left(-\frac{1}{2}, y, z\right)\right|^2 dydz - \int_{-\frac{1}{2}}^{\frac{1}{2}}\int_{-\frac{H}{2}}^{\frac{H}{2}} \left| u_{n,k}\left(x, -\frac{1}{2}, z\right)\right|^2 dxdz$$
$$-2\,\mathrm{Im}\sum_{n'\neq n} i\left\{\frac{\langle n',\mathbf{k}|\,p_x\,|n,\mathbf{k}\rangle\, w_{n'n}^{x*}(\mathbf{k}) + \langle n',\mathbf{k}|\,p_y\,|n,\mathbf{k}\rangle\, w_{n'n}^{y*}(\mathbf{k})}{E_{n'n}(\mathbf{k})}\right\}, \tag{4.127}$$

where we define $w_{n'n}^{y}$ in a manner similar to Eq. (4.121) with p_x and k_x replaced by p_y and βk_y respectively. From this equation we find that the sum of the oscillator strengths will in general depend on the details of the nanopore lattice geometry and resulting bandstructure at each point in the Brillouin zone.

4.5.4 Conclusion

We have proposed the use of the nanopore active layer for detection of radiation in the infrared and terahertz regions of the electromagnetic spectrum. The nature of the selection and sum rules have been outlined and it has been shown that the nanopore active layer is unique in that it allows for exquisite control over the polarization dependence and magnitude of intersubband absorption. Due to in-plane quantization effects, the nanopore array possesses a nonzero in-plane component of the dipole moment, which implies that it should be sensitive to light at normal incidence. In addition, due to the fact that the nanopore array is a patterned structure, it should suffer less from inhomogeneous broadening effects in comparison to self-assembled QD arrays.

The nanopore active layer may be particularly well suited to applications in polarimetry. Current approaches to far-infrared polarimetry utilize linear gratings etched onto the surface of individual pixels in the QWIP detector. Detection of the full

polarization vector would require stacking multiple detectors with different grating orientations [90]. The nanopore active layer may provide an alternative in which the polarization dependence of each layer could be designed into the lattice geometry. By utilizing multiple layers sensitive to different polarizations, the full polarization vector could in principle be read without stacking multiple individual devices. The nanopore array could also be used in a more traditional far-infrared detector, utilizing bound-to-bound or bound-to-continuum transitions with the benefits of normal incidence detection in addition to reduced inhomogeneous broadening and larger gain volume compared to self-assembled QDs. Finally, with further improvement in carrier extraction techniques and epitaxial design to reduce dark currents, the nanopore array has the potential be used as a terahertz detector. All of these applications benefit from the wide range of parameters such as the lattice geometry, lattice constant, pore diameter, and material system which can be used to fine-tune the absorption properties to target a specific application. We note briefly that small variations in the size of the pores or lattice constant introduced during the electron beam lithography process will likely lead to a small amount of broadening, although this is difficult to quantify due to the fact that variations in lattice geometry make the inverse quantum dot structure nonperiodic and therefore significantly more difficult to analyze numerically. However, we can predict qualitatively that the effects of these variations will be less severe for small pore sizes and large lattice constants in the regime where quantum size effects just begin to become important.

4.5.5 Numerical expressions

Utilizing orthonormality of the basis functions and Eqs. (4.107) - (4.109), one can obtain the following simplified expressions for the integrals in Eq. (4.127):

$$\int_{-\frac{1}{2}}^{\frac{1}{2}}\int_{-\frac{H}{2}}^{\frac{H}{2}}\left|u_{n,k}\left(-\frac{1}{2},y,z\right)\right|^2 dydz=\sum_{\substack{i,j\\ i',j'}} a_{i,j}^{n*}a_{i',j'}^{n}(-1)^{(l_{i'}-l_i)}\delta_{m_{i'},m_i}\delta_{j,j'} \tag{4.128}$$

$$\int_{-\frac{1}{2}}^{\frac{1}{2}}\int_{-\frac{H}{2}}^{\frac{H}{2}}\left|u_{n,k}\left(x,-\frac{1}{2},z\right)\right|^2 dxdz=\sum_{\substack{i,j\\ i',j'}} a_{i,j}^{n*}a_{i',j'}^{n}(-1)^{(m_{i'}-m_i)}\delta_{l_{i'},l_i}\delta_{j,j'}\ . \tag{4.129}$$

Using a similar technique we obtain the following expressions for the various contributions to $w_{n'n}^{x}(\mathbf{k})$ in Eq. (4.121):

$$\left\langle n',\mathbf{k}\right|p_x\left|n,\mathbf{k}\right\rangle=2\pi\sum_{\substack{i=i'\\ j=j'}} l_i a_{i',j'}^{n'*}a_{i,j}^{n} \tag{4.130}$$

$$\left\langle n',\mathbf{k}\right|p_x+k_x\left|n,\mathbf{k}\right\rangle_{QW}=2\pi\sum_{\substack{i,i'\\ j,j'}} a_{i',j'}^{n'*}a_{i,j}^{n}\left(l_i+\frac{k_x}{2\pi}\right)\delta_{i,i'}Z_{j,j'} \tag{4.131}$$

$$\left\langle n',\mathbf{k}\right|p_x+k_x\left|n,\mathbf{k}\right\rangle_{Pore}=2\pi\sum_{\substack{i,i'\\ j,j'}} a_{i',j'}^{n'*}a_{i,j}^{n}\left(l_i+\frac{k_x}{2\pi}\right)U_{i,i'}Z_{j,j'} \tag{4.132}$$

$$\begin{aligned}\left\langle n',\mathbf{k}\right|\frac{1}{m^*}\delta\left(x+\frac{1}{2}\right)\left(p_x+k_x\right)\left|n,\mathbf{k}\right\rangle=2\pi\sum_{\substack{i,i'\\ j,j'}} a_{i',j'}^{n'*}a_{i,j}^{n}\left(l_i+\frac{k_x}{2\pi}\right)\Big\{&\left(-1\right)^{(l_i-l_{i'})}\delta_{m_i,m_{i'}}\delta_{j,j'}\\ &+\left(\frac{1}{m_w^*}-1\right)\left(-1\right)^{(l_i-l_{i'})}\delta_{m_i,m_{i'}}Z_{j,j'}\Big\}\end{aligned} \tag{4.133}$$

$$i\left\langle n',\mathbf{k}\right|\frac{1}{2m^*}\dot{\delta}\left(x+\frac{1}{2}\right)\left|n,\mathbf{k}\right\rangle=\pi\sum_{\substack{i,i'\\ j,j'}}a_{i',j'}^{n'*}a_{i,j}^{n}\left(n_i-n_{i'}\right)\left\{\left(-1\right)^{(l_i-l_{i'})}\delta_{m_i,m_{i'}}\delta_{j,j'}\right.$$
$$\left.+\left(\frac{1}{m_w^*}-1\right)\left(-1\right)^{(l_i-l_{i'})}\delta_{m_i,m_{i'}}Z_{j,j'}\right\},\tag{4.134}$$

where

$$Z_{j,j'}=\frac{\sin\left(j'+j\right)\frac{\pi}{2}\left(1-\frac{W}{H}\right)-\sin\left(j'+j\right)\frac{\pi}{2}\left(1+\frac{W}{H}\right)}{\pi\left(j'+j\right)}$$
$$-\frac{\sin\left(j'-j\right)\frac{\pi}{2}\left(1-\frac{W}{H}\right)-\sin\left(j'-j\right)\frac{\pi}{2}\left(1+\frac{W}{H}\right)}{\pi\left(j'-j\right)}\tag{4.135}$$

if $j'\neq j$, and

$$Z_{j,j'}=\frac{W}{L}+\frac{\sin\pi j\left(1-\frac{W}{L}\right)-\sin\pi j\left(1+\frac{W}{L}\right)}{2\pi j}\tag{4.136}$$

if $j'=j$, and

$$U=\int_0^{\rho}\int_0^{2\pi}re^{i2\pi\left[(n_i-n_{i'})x+(m_i-m_{i'})y\right]}drd\theta$$
$$=2\pi\rho\frac{J_1\left(\rho C\right)}{C}\tag{4.137}$$

if $C\neq 0$, and

$$U=\pi\rho^2$$

if C=0 where J_1 is the Bessel function of the first kind and

$$C=\sqrt{A^2+B^2}$$
$$A=2\pi\left(n_i-n_{i'}\right)\quad.$$
$$B=2\pi\left(m_i-m_{i'}\right)$$

4.6 Parametric Analysis and Optimization of the Nanopore Active Layer

In this section, we present a detailed analytical study of the effect of nanopore lattice geometry, material parameters, and temperature on the density of states and intraband energy gaps in an ordered nanopore array diode laser. An improved fabrication process is proposed to increase the peak gain achievable in the nanopore laser by a factor of three.

In Section 4.6.1, we explore the effect of the shape of the unit cell on the bandstructure and density of states. The effects of lattice pitch and pore diameter on the bandstructure as well as the magnitude of the intraband energy gaps are investigated in Section 4.6.2. In Section 4.6.3 we outline the effects of material system and material parameters. Finally, in Section 4.6.4 the effect of temperature on the density of states and emission spectrum is explored. Parameters used in the simulations can be found in Table 4.1.

4.6.1 Unit cell geometry

Unit cell geometry has the most pronounced impact on the overall shape of the density of states and therefore on the shape of the laser emission spectrum. The first nanopore lasers were designed with a triangular unit cell in order to maximize the pore density. In this section we will investigate the bandstructure and density of states of a triangular geometry and square geometry, which are the two most commonly used geometries in periodic structures such as photonic crystals.

Figure 4.19 shows the three-dimensional bandstructure for electrons in the conduction band for a nanopore lattice with triangular and square unit cell geometries. More traditional plots of the bandstructure which show the energy along lines in k-space

connecting the symmetry points of the Brillouin zone are shown in Fig. 4.20. Note that Fig. 4.19 shows only the first three subbands for clarity, while Fig. 4.20 shows the first four subbands. It is interesting to note the drastic changes in the bandstructure which can be brought about simply by changing the unit cell geometry. The primary difference in the two bandstructures is the location of the largest energy gap. In the triangular unit cell geometry, the largest gap exists between the second and third subbands, while in the square unit cell geometry, the largest gap exists between the first and second subbands.

Figure 4.21 shows plots of the density of states derived from the band diagrams, which more clearly reveal the magnitude and position of the energy gaps. The size of the largest gap for the hexagonal unit cell geometry is approximately 0.8 meV, while that for the square unit cell geometry is approximately 1.2 meV. Furthermore, in the triangular geometry the first and second subbands are quite distinct, while in the square geometry the second and third subbands are indistinguishable and blend together to form what appears to be a single band. We also note that the quantized energies are slightly higher in the triangular geometry compared to the square geometry by approximately 1 meV. We attribute this to the higher fill factor and therefore smaller confinement volume of the triangular geometry. Finally, the triangular geometry appears to offer a slightly higher peak density of states resulting from the flat third subband, which is an important observation when designing a semiconductor laser based on the nanopore active layer.

4.6.2 Lattice pitch and nanopore diameter

One of the novel features of the nanopore active layer is that the density of states can be tuned continuously between that of an ordinary quantum well and that of a QD. In the limit of small pore size, the nanopore structure exhibits characteristics similar to a

quantum well. As the pore diameter approaches the lattice pitch, the in-plane component of quantum confinement increases, eventually resulting in triangular shaped QDs as shown in Fig. 4.22. The evolution from quantum well to QDs is also evident in the energy bandstructure shown in Fig. 4.23. As the pore diameter increases, the bands become flatter and span a narrower range of energies. The contribution to the density of states from each band therefore becomes more delta-function-like which is a defining characteristic of QDs. Note that in the limit of large pore diameter the first two subbands become nearly degenerate in energy. In addition, the third subband appears to be the most sensitive to variation in pore diameter.

One of the primary parameters of interest is the magnitude of the energy gap between the second and third subbands. The future use of the nanopore active layer for applications in the terahertz or far-infrared region of the spectrum will likely require the accurate tuning of this energy gap in order to achieve the desired absorption or emission properties. Figure 4.24(a) shows the variation of the energy gap between the second and third subbands, defined as the minimum energy of the third subband minus the maximum energy of the second subband, with increasing pore diameter for conduction band electrons. Figure 4.24(b) shows a similar plot for heavy holes in the valence band. Each curve in the plot represents a different lattice pitch.

For electrons in the conduction band and large pitches, the energy gap is relatively insensitive to changes in the pore diameter over a wide range of diameters. The curves are characterized by a sharp kink as the pore diameter approaches the lattice pitch and the quantum confined states become more QD-like. Note that there is a steady increase in the maximum achievable energy gap as the pitch is reduced from 100 nm to 60 nm. In order

to explain this feature of the data, we note again that when the pore diameter is equal to the lattice pitch, we effectively have an array of QDs. One would therefore expect that the energy gap should increase as the in-plane area of the QDs is reduced. This area can be easily computed assuming that the pore diameter is equal to the lattice pitch as the area of the triangular unit cell minus the area occupied by the pores in the unit cell. The expression is given by $a^2\left(\sqrt{3}/4-\pi/8\right)$ where a is the lattice pitch. Thus the QD volume decreases as a^2 and we should expect an increase in the size of the energy gap in correspondence with this decrease in volume. At a pitch of 50 nm the maximum gap remains almost unchanged, while at a pitch of 40 nm the maximum gap begins decreasing. We attribute this feature of the data to an increase in QD coupling strength as the lattice pitch is reduced below 50 nm. Note also that as the pitch is reduced, the kink in the curves becomes less prominent, implying that the gap size becomes more sensitive to small variations in pore diameter.

For the case of heavy holes in the valence band shown in Fig. 4.24(b), the curves are in general more sharply kinked compared to the curves for electrons in the conduction band. In addition, the peak energy gap continues to increase as the pitch is reduced, which is an indication that even at pitches as low as 40 nm heavy holes do not couple strongly between QDs. Finally, the maximum achievable gap in the valence band is approximately half that in the conduction band. These features of the data for heavy holes can be attributed to the significantly larger effective mass of the heavy hole compared to the electron.

4.6.3 Material system parameters

In addition to the geometrical characteristics of the nanopore laser such as unit cell geometry, pore diameter, and lattice pitch, the characteristics of the nanopore active layer are also strongly affected by the potential barrier height between the quantum well and the pores. This barrier height is determined by the material system used in the fabrication process, which at the present time has been limited to the InGaAs/GaAs system. In this material system, the flexibility in engineering the potential barrier height results from control over the indium composition of the quantum well material.

Figure 4.25 shows the magnitude of the density of states in each of the three subbands as a function of indium composition in the InGaAs layer. The third subband experiences the largest effect, increasing by nearly a factor of three over the entire range of indium compositions investigated. The observed increase in the density of states can be attributed to the third subband becoming significantly flatter as the potential barrier height is increased. In contrast, the density of states of the first and second subbands decreases only slightly and is relatively insensitive to variations in indium content.

Figure 4.26 shows the separation in energy between adjacent peaks in the density of states. The separation between the third subband peak, represented by P3, and the second subband peak, represented by P2, increases from 2.5 meV to 4 meV for indium compositions ranging between 5% and 50%. In contrast, the separation between the first and second subband peaks represented by P1 and P2, respectively, remains relatively unchanged over the entire range of indium compositions. Thus the indium content also has a significant impact on the magnitude of the largest intraband energy gap.

Due to the unique delta-function-like nature of the third subband, it is desirable to increase the density of states for this subband relative to the other subbands as much as

possible in order to realize the advantages predicted for quantum dot lasers, namely low threshold current and high differential quantum efficiency. The trends shown for the InGaAs/GaAs material system are encouraging in this respect. However, increasing the indium composition entails certain practical difficulties in the fabrication process.

In selective area growth, there are two important factors which can significantly change the material properties. These factors are growth enhancement and composition enhancement [91-98]. Growth enhancement refers to the increase in epilayer thickness which must occur due to conservation of mass when growing on a patterned template. In this case, an InGaAs quantum well is being grown on a template of SiO_2 dots. The enhancement factor can be calculated as the ratio of the total area of the unit cell to the open area of the unit cell not covered by the SiO_2 mask. Composition enhancement refers to the increase in indium content in an InGaAs epilayer when grown on a masked substrate. It is important to note that as the indium composition is increased, the critical thickness for the formation of dislocations decreases, being approximately 5 nm for an $In_{0.50}Ga_{0.50}As$ quantum well [99]. Thus both the thickness and composition of the quantum well must be carefully controlled to prevent the formation of misfit dislocations. Although the growth enhancement factor can be approximated, it is more difficult to predict the indium composition with a high degree of certainty. Furthermore, the growth of high indium content epilayers by MOCVD generally requires growth at relatively low temperatures below 600 °C, and thus the material quality also suffers.

Ideally, instead of modifying the composition of the quantum well, one could change only the characteristics of the barrier material that are not affected by growth enhancement. One possibility is the use of an AlGaAs barrier which has the advantage of

providing a large bandgap and therefore large potential barrier. However, it is well known that the use of AlGaAs is incompatible with MOCVD regrowth due to the oxidation of aluminum.

Details of the current fabrication process can be found in [2, 38], but will be briefly outlined here for clarity. The present fabrication technique for a nanopore laser begins with a base structure consisting of a GaAs substrate with a 1 μm AlGaAs lower cladding and a 100 nm GaAs lower core. The nanopore template is then patterned on the lower core, and the InGaAs quantum well and 10 nm GaAs cap are then regrown on the template. After stripping the template, a 100 nm GaAs upper core is grown. A ridge waveguide is then etched through the active layer just far enough to remove the quantum well, leaving part of the lower core in order to prevent exposure of the underlying AlGaAs layer. A 1.5 μm AlGaAs upper cladding and 100 nm GaAs contact layer are then regrown to complete the buried heterostructure.

The use of an AlGaAs core would clearly be incompatible with the existing process due to oxidation of the AlGaAs. However, one could in principle circumvent this problem with appropriate modifications to the process. First, instead of etching the ridge waveguide after the regrowth of the GaAs upper core, we propose the etching of the ridge waveguide immediately after the regrowth of the InGaAs nanopore active layer. At this point there is no exposed AlGaAs. Next we grow a thin, approximately 20 nm thick AlGaAs layer to serve as the potential barrier for the nanopore active layer, and continue growth of the GaAs upper core, AlGaAs upper cladding, and GaAs contact layers. By making these modifications to the process we reduce the number of regrowth steps in addition to incorporating a high potential barrier layer which could in principle

significantly increase the density of states and therefore the gain of the nanopore laser. Note that the potential barrier is now asymmetric on either side of the nanopore active layer, consisting of GaAs beneath the nanopore layer, and AlGaAs both inside the pores as well as on top of the nanopore active layer.

In order to see the potential benefits of this process, we can proceed with calculations similar to those performed for the varied indium composition of the nanopore layer. Instead of varying the indium composition, we keep the indium composition fixed at 25% and vary only the aluminum composition used for the upper barrier layer. Figure 4.27 shows the peak density of states for each of the first three subbands as a function of aluminum composition in the barrier layer. Note that the density of states of the delta-function-like third subband increases by approximately a factor of three at aluminum compositions as low as 40%. In contrast, the density of states of the first two subbands decreases slightly. This is highly desirable since we would like to emphasize the QD-like properties of the nanopore active layer in order to achieve the potential benefits of low threshold current and high differential quantum efficiency. Figure 4.28 shows the separation between the peaks in the density of states between the first and second subbands and between the second and third subbands. The energy gaps remain relatively unchanged with increasing aluminum composition.

4.6.4 Temperature effects

For potential infrared or terahertz applications of the nanopore active layer it is important to understand the effect of temperature on the intraband energy gaps and density of states. For semiconductor lasers it is also generally desirable for the laser spectrum to be insensitive to temperature.

Figure 4.29 shows the position of each subband peak in the density of states as a function of temperature between 0 K and 300 K. Each peak experiences a negligible redshift of 0.5 meV over the entire temperature range. As shown in Fig. 4.30, the separation between the peaks stays constant. Thus, we expect the primary temperature dependence of the spectral characteristics to result from the temperature dependence of the InGaAs bandgap, which would simply result in an equal redshift of each subband with increasing temperature. More importantly, the relative positions of the peaks in the density of states and the magnitudes of the intraband energy gaps should remain unchanged with temperature, which is an important and desirable characteristic for the use of the nanopore active layer in any terahertz or far-infrared applications.

4.7 Carrier Scattering Mechanisms

Carrier scattering is an important consideration in the nanopore active layer because it determines the rate at which carriers thermalize to the lowest energy subbands. The physics of intersubband scattering changes drastically in the nanopore structure due to the three-dimensional nature of the electron and hole envelope functions. In Chapter 5, it will be shown experimentally that excited state subbands tend to reach threshold before the lower energy subbands. This is contradictory to the behavior one would expect based on a Fermi distribution of carriers. The implication is that the intersubband scattering lifetime is greater than the spontaneous emission lifetime, which is typically on the order of nanoseconds. In a typical quantum well this is clearly not the case, and lasing is always observed near the band edge.

Electron-phonon interactions are governed by the same physics as electron-photon interactions, namely Fermi's golden rule given by

$$\frac{1}{\tau}=\frac{2\pi}{\hbar}\sum_{f,q}\alpha^2(q)\left|\left\langle\psi_f\left|e^{i\mathbf{q}\cdot\mathbf{r}}\right|\psi_i\right\rangle\right|^2\delta\left(E_f-E_i\pm E_q\right)\left[n_B\left(E_q,T_l\right)+\begin{Bmatrix}1\\0\end{Bmatrix}\right] \tag{4.138}$$

where τ is the scattering lifetime; $\alpha^2(q)$ depends on the type of phonon scattering (optical or acoustic, deformation or polar); ψ_f, ψ_i are the final and initial state wavefunctions; E_q is the phonon energy; and n_B is the Bose-Einstein distribution given by

$$n_B(E_q,T_l)=\frac{1}{e^{E_q/k_BT_l}-1}. \tag{4.139}$$

By analogy to electron-photon interactions, one can have both stimulated emission and spontaneous emission of phonons. In the emission process one must take into account both stimulated and spontaneous emission, in which case one uses the upper signs in the above equation, and the stimulated emission rate is proportional to n_B while the spontaneous emission rate results from the 1 in the $\begin{Bmatrix}1\\0\end{Bmatrix}$ term. For absorption one uses the lower signs and the 0 in the $\begin{Bmatrix}1\\0\end{Bmatrix}$ term since spontaneous absorption is nonexistent.

In an ordinary quantum well, the dominant scattering mechanism depends on the energy scale and the temperature. Energy conservation demands that the difference between the initial and final states matches the phonon energy. The LO phonon energies in InGaAs are 28.9 meV and 33.6 meV. These energies are independent of phonon wavevector as a result of the nearly flat dispersion of the LO phonon bands. This fact implies that once energy conservation is satisfied, it is trivial to satisfy momentum conservation since we are free to choose the particular phonon wavevector we need to equal the difference between the initial and final state wavevectors. Thus, LO phonon

scattering is a very efficient intersubband scattering process at room temperature with a typical carrier scattering lifetime of 100 s of femtoseconds, much faster than any optical processes. At temperatures where $k_B T \ll E_q$, however, optical phonon scattering becomes much less efficient due to the temperature dependence of the Bose-Einstein distribution. Stimulated emission of LO phonons can be drastically reduced, in which case acoustic phonon scattering becomes the dominant carrier relaxation mechanism. Acoustic phonon scattering rates dominate intrasubband relaxation independent of temperature, but intersubband relaxation is still much slower compared to LO phonon scattering due to the linear dispersion of the acoustic phonon branch which makes satisfying both momentum and energy conservation more difficult and restricts the energy a carrier can lose in a single scattering event. Typical acoustic phonon scattering rates are on the order of 100 s of picoseconds. This is slower than stimulated emission of photons but faster than spontaneous emission.

In the next sections we will outline the theory of electron-phonon interactions in the nanopore active layer and, for comparison, in an ordinary quantum well, and we will provide some preliminary calculations which indicate that both the optical and acoustic phonon scattering rates are expected to be reduced by about two orders of magnitude in the nanopore structure. These calculations support the observation of initial lasing on excited state subbands as outlined in Chapter 5.

4.7.1 Review of scattering in a quantum well

Recall that in a quantum well the wavefunction has the form

$$\psi(\mathbf{k},\mathbf{r}) = \left(\frac{2}{LA}\right)^{1/2} e^{i\mathbf{k}_{\parallel}\cdot\mathbf{r}_{\parallel}} \sin k_z z, \tag{4.140}$$

which is a simple plane wave in the quantum well plane. The matrix element in Eq. (4.138) evaluates to

$$G\left(\mathbf{k}',\mathbf{k},\mathbf{q}\right)=\delta_{\mathbf{k}'_{\|},\mathbf{k}_{\|}+\mathbf{q}}G\left(k'_z,k_z,q_z\right) \tag{4.141}$$

$$\begin{aligned}
G\left(k'_z,k_z,q_z\right)&=\int_0^L \psi\left(k',z\right)e^{iq_z z}\psi\left(k,z\right)dz \\
&=\frac{1}{2}\left[\frac{\sin\left\{\left(q_z+k'_z-k_z\right)L/2\right\}}{\left(q_z+k'_z-k_z\right)L/2}e^{i\left(q_z+k'_z-k_z\right)L/2}\right. \\
&\quad+\frac{\sin\left\{\left(q_z-k'_z+k_z\right)L/2\right\}}{\left(q_z-k'_z+k_z\right)L/2}e^{i\left(q_z-k'_z+k_z\right)L/2} \\
&\quad-\frac{\sin\left\{\left(q_z+k'_z+k_z\right)L/2\right\}}{\left(q_z+k'_z+k_z\right)L/2}e^{i\left(q_z+k'_z+k_z\right)L/2} \\
&\quad\left.-\frac{\sin\left\{\left(q_z-k'_z-k_z\right)L/2\right\}}{\left(q_z-k'_z-k_z\right)L/2}e^{i\left(q_z-k'_z-k_z\right)L/2}\right].
\end{aligned} \tag{4.142}$$

Equation (4.141) implies strict conservation of in-plane momentum. For the z-component of momentum there is no restriction on the momentum. However, the maxima in $G\left(k'_z,k_z,q_z\right)$ occur for the four momentum conserving values

$$q_z=\pm\left(k'_z\pm k_z\right). \tag{4.143}$$

The inherent "fuzziness" of momentum conservation in the transverse dimension is the result of the uncertainty principle which states that real space and momentum space are related by a Fourier transform. The more the particle wavepacket becomes confined in the growth dimension, the more uncertain its momentum becomes.

For acoustic phonon deformation potential scattering, the scattering rate is given by Eq. (4.138) with

$$\alpha^2\left(q\right)=\frac{D^2}{2\rho c_s^2\Omega},$$

where D is the deformation potential equal to 7.2 eV, ρ = 5500 kg/m^3, c_s = 3400 m/s in InGaAs. For polar LO phonon scattering we have

$$\alpha_i^2(q) = \frac{c_i}{\Omega q^2}, \tag{4.144}$$

where Ω is the volume of a unit cell, q is the phonon wavevector, and

$$\begin{aligned} c_1 &= \frac{2\pi e^2}{\varepsilon_\infty}\left(1-\frac{\omega_{T1}^2}{\omega_{L1}^2}\right)\frac{\omega_{T2}^2-\omega_{L1}^2}{\omega_{L2}^2-\omega_{L1}^2} \\ c_2 &= \frac{2\pi e^2}{\varepsilon_\infty}\left(1-\frac{\omega_{T2}^2}{\omega_{L2}^2}\right)\frac{\omega_{L2}^2-\omega_{T1}^2}{\omega_{L2}^2-\omega_{L1}^2}, \end{aligned} \tag{4.145}$$

which describes the form of the electron-polar optical phonon potential, where c_1 is used for scattering involving the lowest LO branch, and c_2 is used for scattering involving the upper LO branch.

Evaluating Eq. (4.138) requires summing over all possible phonon wavevectors. This process can be performed mathematically as an integral. For acoustic phonon scattering this integral can be evaluated as

$$\begin{aligned} \sum_{q_z}\left|G(k_z',k_z,q_z)\right|^2 &= \int_{-\infty}^{\infty}\left|G(k_z',k_z,q_z)\right|^2 dq_z\,\frac{L}{2\pi} \\ &= \delta_{n,m}+\frac{1}{2}. \end{aligned} \tag{4.146}$$

For optical phonon scattering this integral is complicated by the 1/q^2 dependence of the polar interaction. However, one can still obtain an analytical form for the integral:

$$
\begin{aligned}
L^2(q) &= \sum_{q_z} \frac{\left|G\left(k_z', k_z, q_z\right)\right|^2}{q^2} = \int_{-\infty}^{\infty} \frac{\left|G\left(k_z', k_z, q_z\right)\right|^2}{q_{\|}^2 + q_z^2} dq_z \frac{L}{2\pi} \\
&= \frac{1}{2}\left[\frac{1+\delta_{n,m}}{q_{\|}^2 + \left(k_z' - k_z\right)^2} + \frac{1}{q_{\|}^2 + \left(k_z' + k_z^2\right)} \right. \\
&\quad -2\frac{q_{\|}}{L}\left(1 - e^{-q_{\|}L}\cos\left(k_z' - k_z\right)L\right) \\
&\quad \left. \times\left(\frac{1}{q_{\|}^2 + \left(k_z' - k_z\right)^2} - \frac{1}{q_{\|}^2 + \left(k_z' + k_z\right)^2} \right)^2 \right].
\end{aligned}
\tag{4.147}
$$

4.7.2 Polar LO phonon scattering

In the nanopore structure it is necessary to exercise care in the use of the word "subband." In a quantum well each subband forms as the result of quantization resulting from confinement along the growth direction. These subbands are typically separated by more than an LO phonon energy. In the nanopore, there are again subbands resulting from quantization along the growth direction. However, there are also subbands within these subbands, as the in-plane confinement gives rise to gaps in the in-plane dispersion relations. Thus one must be careful to differentiate whether one is referring to subbands resulting from transverse confinement or in-plane confinement. From this point onward we will adopt the terminology "transverse" and "longitudinal" subbands to differentiate between quantized carrier motion in the transverse or longitudinal directions. As in an ordinary quantum well, we should expect LO phonon scattering to dominate carrier relaxation between transverse subbands due to the fact that these subbands are separated by more than an LO phonon energy.

There are two ways in which the periodic variations in potential in the nanopore structure can change the LO phonon scattering rate. The first is through the formation of

longitudinal subbands in the bandstructure. In an ordinary quantum well, because the in-plane dispersion is a continuous (approximately parabolic) function, there are always states available for a particle in an excited state transverse subband to scatter into a lower energy transverse subband such that energy is conserved. However, in the nanopore it is possible that there are no available states one LO phonon energy below the initial state energy due to the presence of an energy gap. This problem becomes worse as the gaps become larger and the longitudinal subbands become flatter or, in other words, as we approach the regime of full three-dimensional confinement (a quantum dot) by making the pore diameter approach the lattice pitch. This problem is known as the "phonon bottleneck" and can severely limit the LO phonon scattering rate. The second way the nanopore structure can modify the LO phonon scattering rate is through the matrix element of the electron-phonon interaction Hamiltonian. The form of the wavefunction is no longer a simple plane wave in the plane of the quantum well, but also contains a slowly varying envelope. Since the matrix element depends on the wavefunctions in the initial and final states, the matrix element will clearly be changed in the nanopore compared to an ordinary quantum well.

Evaluating this integral is nontrivial and there is no simple analytical formula for the scattering rate. In order to simplify the computations we will assume an infinite barrier in the transverse direction so that the transverse wavefunction is completely confined to the quantum well. The potential barrier height in the cylindrical pores will be kept finite. This simplification allows us to separate the wavefunction as the product of a function of z only and a function of x and y only. This simplification results in the following form for the matrix element:

$$G(\mathbf{k}',\mathbf{k},\mathbf{q}) = G(k_z',k_z,q_z)\,G(k_{\|}',k_{\|},q_{\|}), \tag{4.148}$$

where

$$G(\mathbf{k}_{\|}',\mathbf{k}_{\|},\mathbf{q}_{\|}) = \int_{-a/2}^{a/2}\int_{-a/2}^{a/2} e^{i(\mathbf{k}_{\|}+\mathbf{q}_{\|}-\mathbf{k}_{\|}')\cdot\boldsymbol{\rho}} u_{k_{\|}'}^{f*}(x,y)\,u_{k_{\|}}^{i}(x,y)\,dxdy\,, \tag{4.149}$$

$\boldsymbol{\rho} = x\hat{\mathbf{x}} + y\hat{\mathbf{y}}$, $G(k_z',k_z,q_z)$ is given by Eq. (4.142), $u_{k_{\|}'}^{f}(x,y)$ is the in-plane envelope function of the final state, and $u_{k_{\|}}^{i}(x,y)$ is the in-plane envelope function of the initial state. Once we have the matrix element in Eq. (4.138), we must then perform an integral over q to obtain the total scattering rate:

$$\sum_{q_z}\frac{\left|G(\mathbf{k}',\mathbf{k},\mathbf{q})\right|^2}{q^2} = \frac{\Omega}{(2\pi)^3}\int_{-\infty}^{\infty}\int_{-\infty}^{\infty}\int_{-\infty}^{\infty}\frac{\left|G(k_z',k_z,q_z)\right|^2}{q_z^2+q_{\|}^2}\left|G(k_{\|}',k_{\|},q_{\|})\right|^2 dq_z dq_x dq_y. \tag{4.150}$$

We perform the integral over q_z first because this allows us to use the analytical expression in Eq. (4.147). Having performed this integration, we are then left to perform the integral over $q_{\|}$. This integral increases the computation time significantly since Eq. (4.150) must be evaluated at many points in phonon momentum space to obtain an accurate integration. In reality $\left|G(k_{\|}',k_{\|},q_{\|})\right|^2$ decays to close to zero at some finite value of $q_{\|}$ which allows the truncation of the limits of integration.

To obtain an estimate of the LO phonon scattering rate in the nanopore, let us consider a transition at the Γ point of the Brillouin zone between the first longitudinal subband in the first excited transverse subband, and the first longitudinal subband in the ground state transverse subband. We assume that these two states are separated by exactly one LO phonon energy, where we use the lower LO branch energy in the calculations. For this particular case, the in-plane wavefunctions in the initial and final

states are nearly identical. The two wavefunctions are only different in the transverse direction, in which the lower energy state is a cosine curve (even parity) and the higher energy state is a sine curve (odd parity). Performing the integration in Eq. (4.150) yields a value of 2.6×10^{-4}, which yields a scattering rate of 9.3×10^{10} s^{-1} or a scattering lifetime of 10 ps. In order to contrast this value with that of a quantum well, we evaluate Eq. (4.138) with $q_{\parallel}=0$, $k_z'=\pi/L$, $k_z=2\pi/L$ which yields 1.4×10^{-2} and a net scattering rate of 5×10^{12} s^{-1} or a scattering lifetime of 200 fs, which is in good agreement with experimentally observed values. Thus we expect the intersubband (between transverse bands) scattering rate in the nanopore to be two orders of magnitude smaller than that of an ordinary quantum well. Although the scattering lifetime of 10 ps in the nanopore is still much smaller than typical spontaneous emission lifetime, the carrier densities in the excited state subbands should be expected to be much larger (by about 2 orders of magnitude) than in a typical quantum well at comparable total carrier densities. Thus we should expect to observe significant spontaneous emission from excited state subbands at much lower total carrier densities in the nanopore compared to an ordinary quantum well. Indeed, this is the behavior we observe experimentally as will be shown in Chapter 5.

4.7.3 Acoustic phonon scattering

To analyze the acoustic phonon scattering rate, we again are interested in computing the matrix element given by Eqs. (4.148)-(4.149). However, the linear dispersion of the acoustic phonon branch significantly modifies the integration over phonon wavevectors. We are no longer free to choose any wavevector we wish to satisfy momentum conservation. For a particular energy separation between initial and final states ΔE, the phonon wavevector is determined according to

$$q = \frac{\Delta E}{\hbar c_s}, \tag{4.151}$$

where c_s is the speed of sound in InGaAs (~3400 m/s). Since the magnitude of the phonon wavevector is fixed by this relationship, we are only free to change the direction of the vector with magnitude q in momentum space. This vector can be visualized as tracing out a sphere with radius q, where any point on this sphere satisfies energy conservation. Let us define angles as in the usual spherical coordinate system so that the following formulas give the projection of the vector onto the three coordinate axes:

$$\begin{aligned} q_x &= q \sin\theta \cos\varphi \\ q_y &= q \sin\theta \sin\varphi \\ q_z &= q \cos\theta. \end{aligned} \tag{4.152}$$

The integral over $\mathbf{q}$ then becomes an integral over θ, φ.

To obtain an estimate of the intersubband scattering rate, we consider scattering within the ground state transverse subband. Let us consider the transitions from the Γ point of the second longitudinal subband to all **k** points in the first longitudinal subband. Figure 4.31 shows the intersubband acoustic phonon scattering rate as a function of **k** point in the first subband. Note that the scattering rate is largest at Γ=0. Figure 4.32 shows the how the scattering rate between the Γ points of the two subbands depends on the wavevector of the emitted phonon. It is interesting to note from this plot that emission of phonons is favored in the plane of the quantum well and in the four principle symmetry directions $+\hat{\mathbf{x}}$, $-\hat{\mathbf{x}}$, $+\hat{\mathbf{y}}$, and $-\hat{\mathbf{y}}$ of the square lattice. In the plot these directions correspond to $(\theta, \varphi) = (90°, 0°), (90°, 90°), (90°, 180°), (90°, 270°)$.

To obtain the total scattering rate out of the Γ point, we integrate the result in Fig. 4.31 over the Brillouin zone and divide by the **k**-space area per state which is $(2\pi)^2$ where we are working in units where *a*, the lattice pitch, is equal to 1. This integration gives a net scattering rate out of the Γ point of 3.6×10^7, which is equivalent to a scattering lifetime of 27.5 ns. As in the case of LO phonon scattering, the acoustic phonon scattering rate is lower by two orders of magnitude compared to the rates in a typical quantum well. It is also important to note that 27.5 ns is an order of magnitude *larger* than the spontaneous emission lifetime which is typically on the order of 1 ns. This implies that intersubband scattering is slower than all optical processes in the nanopore structure. Again, this is a surprising result which has important implications for the behavior of a nanopore laser device. It suggests that excited subbands may achieve population inversion and laser threshold before lower energy subbands, independent of the magnitude of the density of states. This is in contradiction with the assumption of a Fermi distribution of carriers. As will be shown in Chapter 5, the spectral behavior of fabricated nanopore laser devices appears to support this conclusion.

4.8 Broadening

Inhomogeneous broadening is an important consideration in an ordered nanopore array. Due to the fact that the subbands are only separated by a few meV in most cases, these energy gaps can easily become obscured by broadening effects. We can gain some insight into the effects of inhomogeneous broadening by considering an ordinary quantum well with infinite barriers in which the quantum confinement energies are determined simply by

$$E = \frac{\hbar^2 \pi^2 n^2}{2m^* L^2}. \tag{4.153}$$

The differential change in energy due to a small change in the well width L is then given by

$$dE = -\frac{\hbar^2 \pi^2 n^2}{m^* L^3} dL. \tag{4.154}$$

From this equation, we find two important facts: (1) the change in energy is proportional to n^2 which implies that the effect on higher energy subbands will be greater than on lower energy subbands, and (2) it is inversely proportional to L^3 which implies that the smaller the well, the larger the shift in energy for a given change in L.

Based on these deductions we can predict that inhomogeneous broadening in the nanopore will be significantly worse for higher lying subbands than for subbands near the band edge, and the energy gaps are more likely to be obscured. In addition, we should expect the broadening to become worse with increasing pore size.

In order to quantify these predictions, we have calculated the density of states for a few different cases assuming a Gaussian distribution of pore sizes centered around 60 nm with a pitch of 100 nm in a square lattice geometry as shown in Figs. 4.33-4.35. We assume that there are no pores which have sizes above some diameter d_{max} and below some diameter d_{min}, or in other words we truncate the Gaussian above d_{max} and below d_{min}. Each plot assumes a different d_{max} and d_{min}. Within each plot the standard deviation of the Gaussian distribution is varied from 0 nm to 5 nm.

From Fig. 4.35 we can see that for a d_{max} and d_{min} of 65 and 55 nm, respectively, with a standard deviation of 5 nm, the higher energy subbands are completely obscured by broadening. However, the typical variation observed in fabricated devices is no more

than ±3 nm. This would correspond to the case of Fig. 4.34. The standard deviation of the pore diameter in the fabricated devices is uncertain. However, based on the experimentally obtained spectra in Chapter 5 which show very distinct subbands, we should expect a standard deviation of no more than about 1 nm based on the plots in Fig. 4.34.

4.9 Table and Figures

Table 4.1 Parameters used in the simulations for the temperature dependent bandgaps, particle effective masses, and lattice constants of GaAs, InGaAs, and AlGaAs.

	GaAs	$In_xGa_{1-x}As$	$Al_xGa_{1-x}As$
E_g(eV)	$1.519 - 5.405\times10^{-4}\frac{T^2}{(T+204)}$	$0.42+0.625(1-x)-\left(\frac{5.8}{(T+300)}-\frac{4.19}{(T+273)}\right)\times10^{-4}T^2(1-x)-4.19\times10^{-4}\frac{T^2}{(T+271)}+0.475(1-x)^2$	$1.519+1.155x+0.37x^2-5.41\times10^{-4}\frac{T^2}{(T+204)}$ (x<0.45) $1.981+0.124x+0.144x^2-4.6\times10^{-4}\frac{T^2}{(T+204)}$ (x>0.45)
$m_e^*(m_0)$	0.067	$0.023+0.037(1-x)+0.003(1-x)^2$	0.063+0.083x (x<0.45) 0.85-0.14x (x>0.45)
$m_h^*(m_0)$	0.51	0.41+0.1(1-x)	0.51+0.25x
a_0 (Å)	5.6533	6.0584x+5.6533(1-x)	5.6533+0.0078x

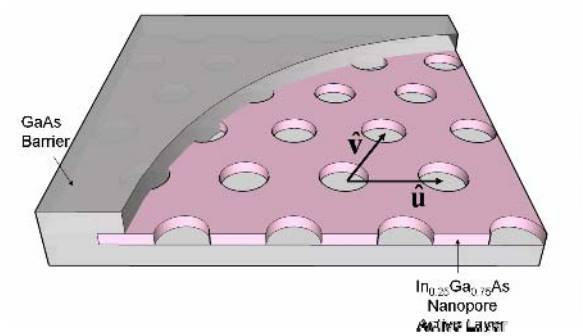

Fig. 4.1 Schematic illustration of the nanopore active layer which consists of a hexagonal array of cylindrical GaAs barriers perturbing an InGaAs quantum well.

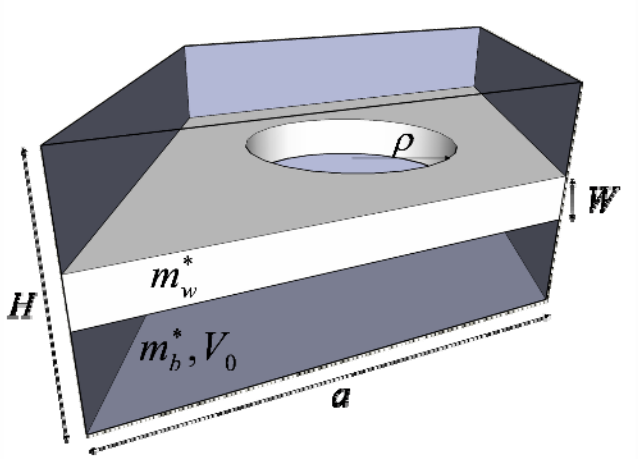

Fig. 4.2 Illustration of the ordered nanopore array unit cell with definition of the relevant variables.

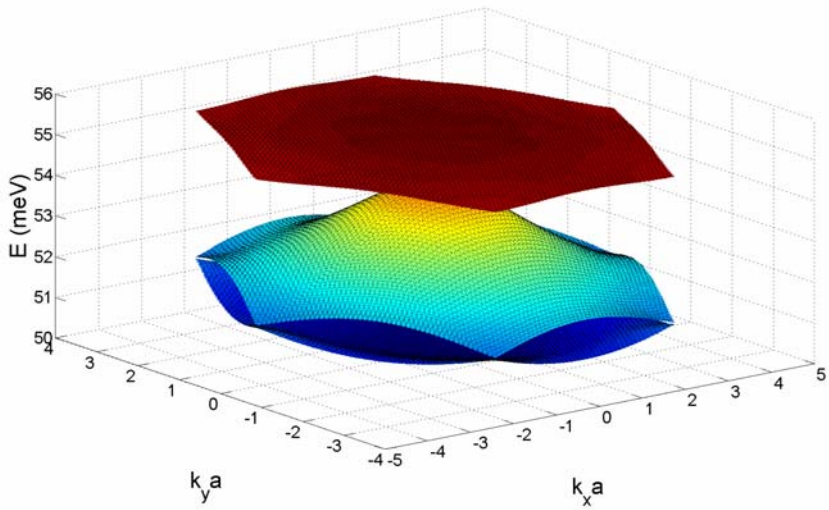

(a)

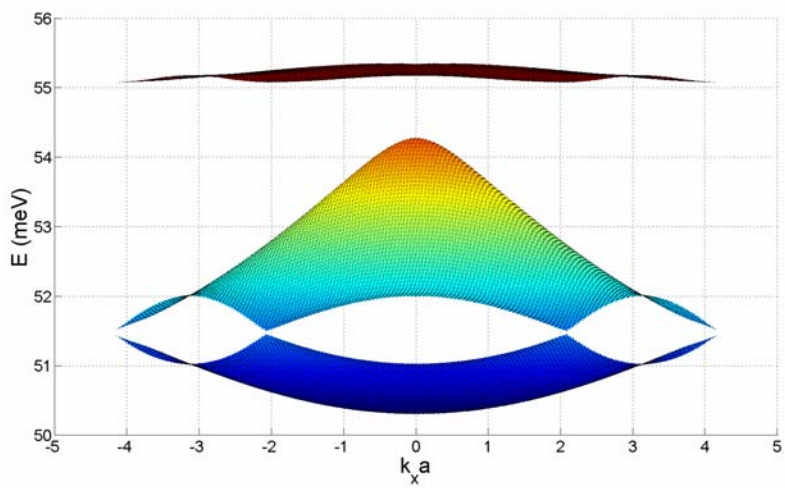

(b)

Fig. 4.3 First three conduction subbands plotted over the hexagonal Brillouin zone from (a) top-down perspective and (b) side perspective. Energies are referenced relative to the strained conduction band edge.

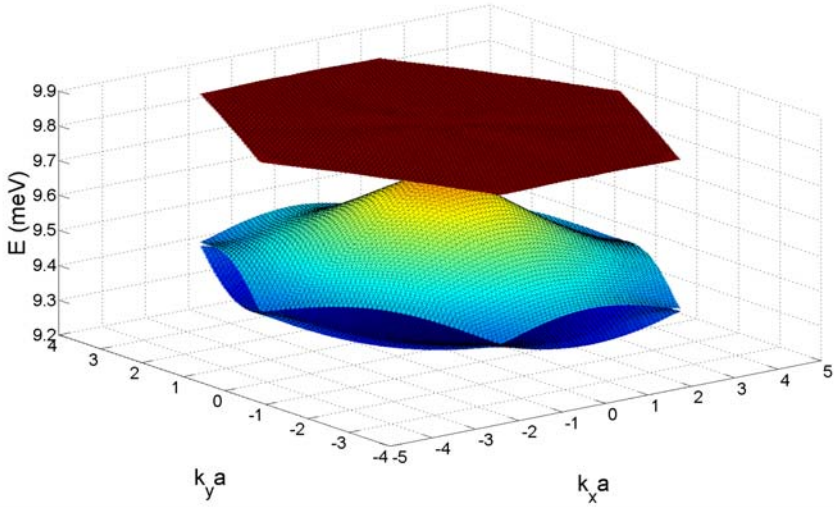

(a)

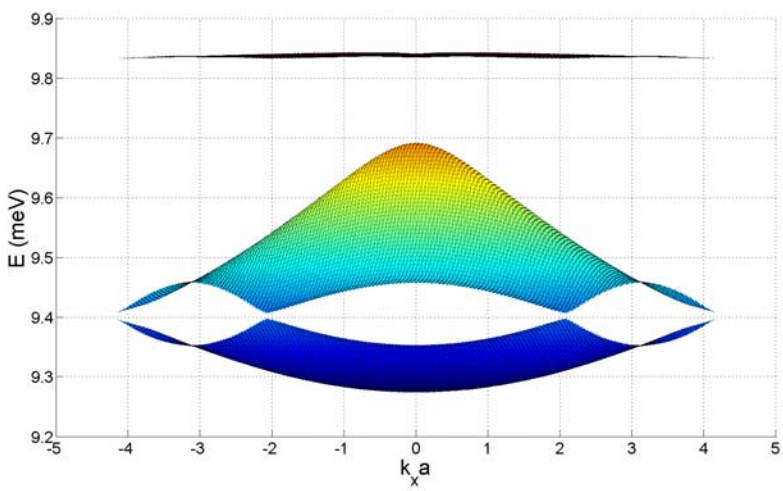

(b)

Fig. 4.4 First three valence subbands plotted over the hexagonal Brillouin zone from (a) top-down perspective and (b) side perspective. Energies are referenced relative to the strained valence band edge.

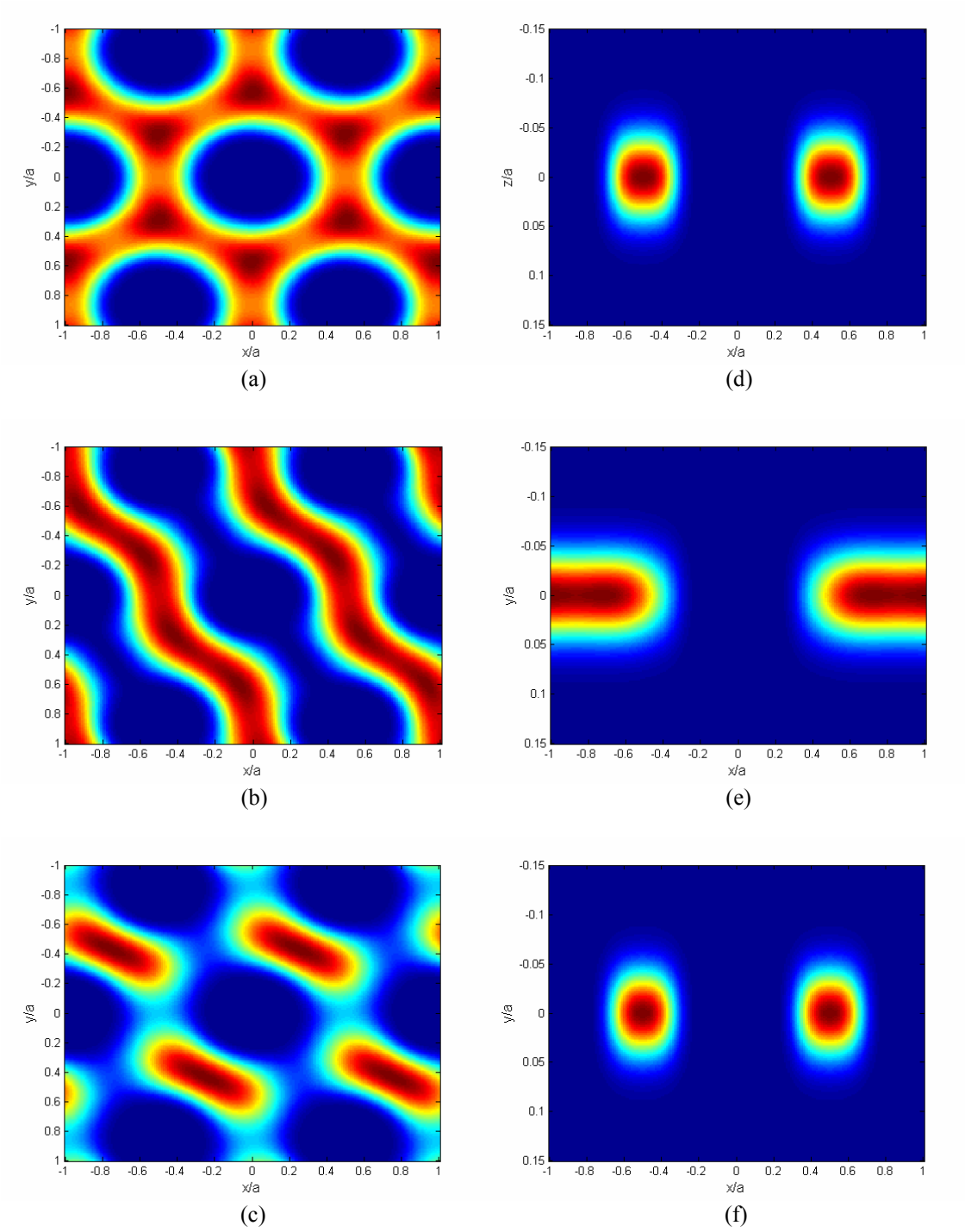

Fig. 4.5 Electron wavefunctions at the symmetry points of the Brillouin zone. Top-down views of the wavefunction are shown in the left column at the (a) Γ (b) M and (c) K points of the Brillouin zone. Cross-sectional views of the corresponding wavefunctions in the left column are shown in the right column along lines connecting (d) Γ to M, (e) Γ to K, and (f) Γ to M .

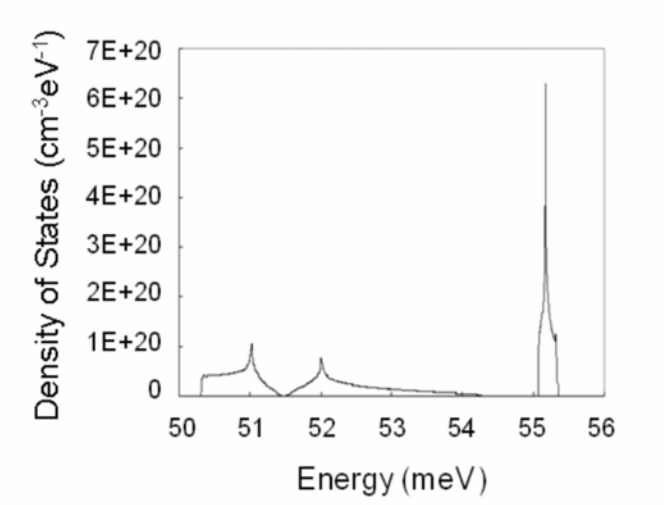

Fig. 4.6 Conduction band density of states showing the contribution from the first three subbands. Energies are referenced relative to the strained conduction band edge.

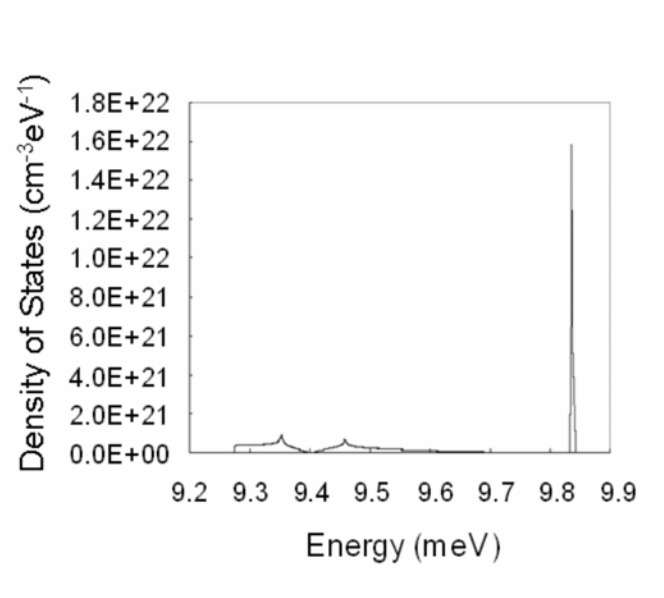

Fig. 4.7 Valence band density of states showing the contribution from the first three subbands. Energies are referenced relative to the strained valence band edge.

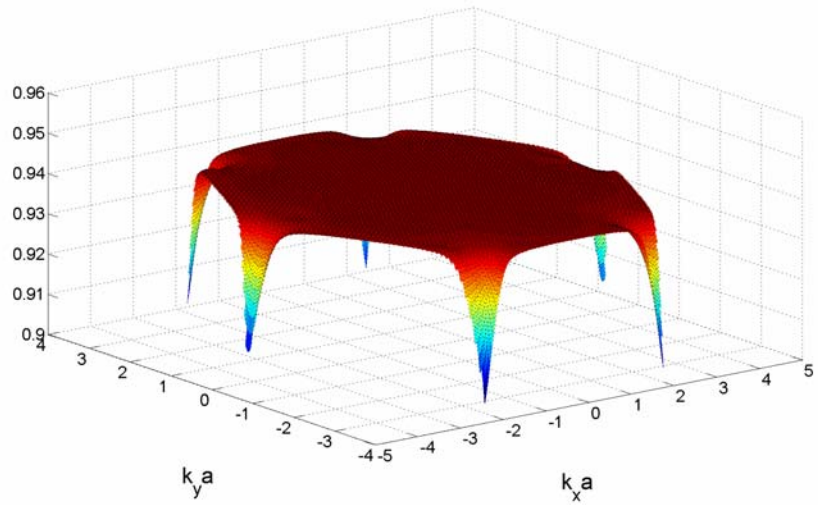

(a)

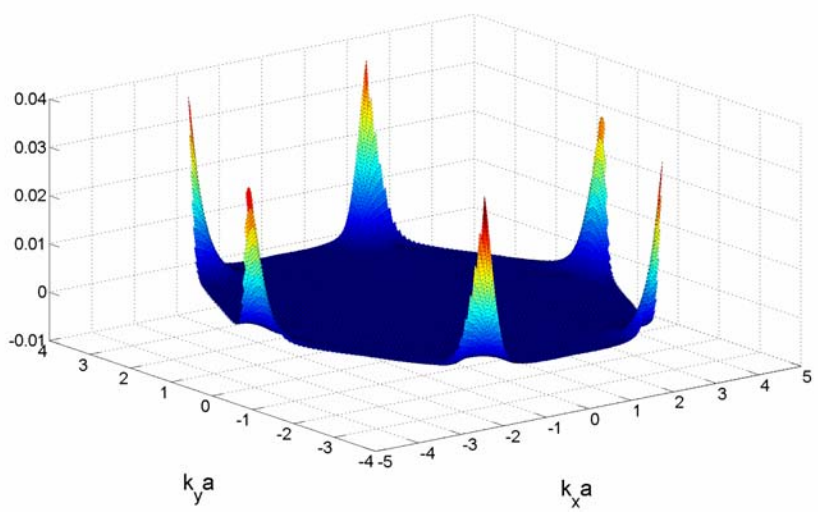

(b)

Fig. 4.8 Squared modulus of the electron-hole wavefunction overlap integral for the transition between (a) the first electron and first hole subband and (b) the first electron and second hole subband.

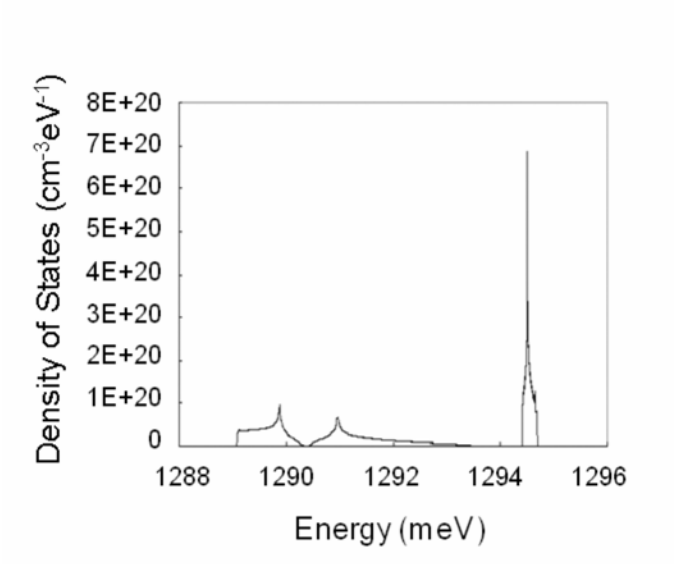

Fig. 4.9 Joint density of states showing the contribution from the first three subbands.

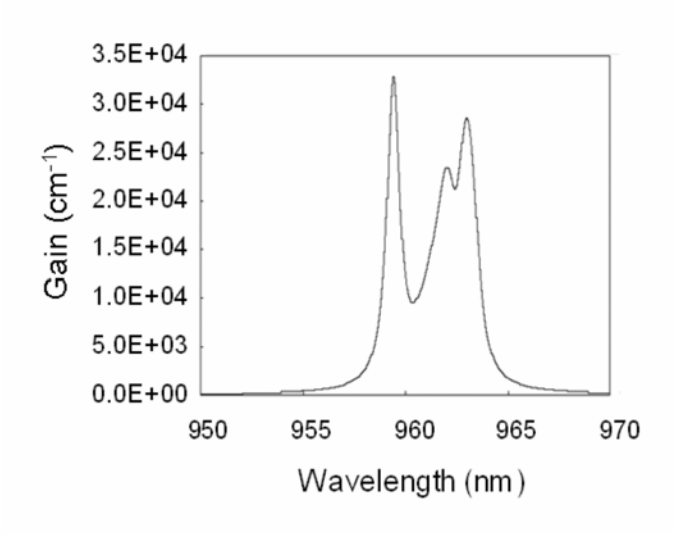

(a)

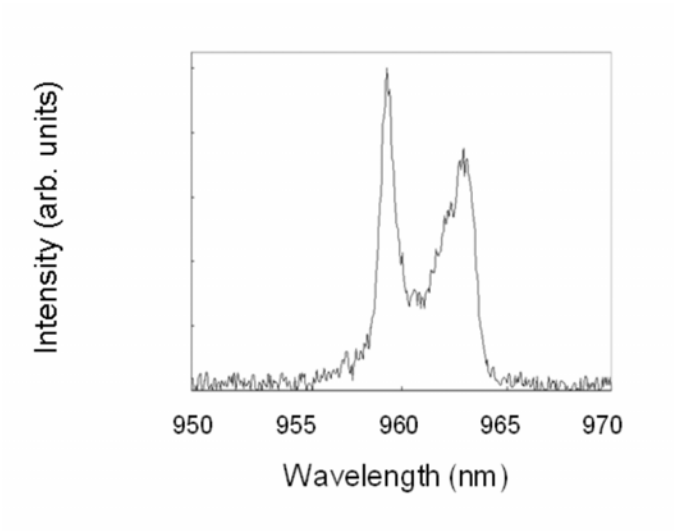

(b)

Fig. 4.10 (a) Computed gain spectrum and (b) measured emission spectrum at 90 mA injection current.

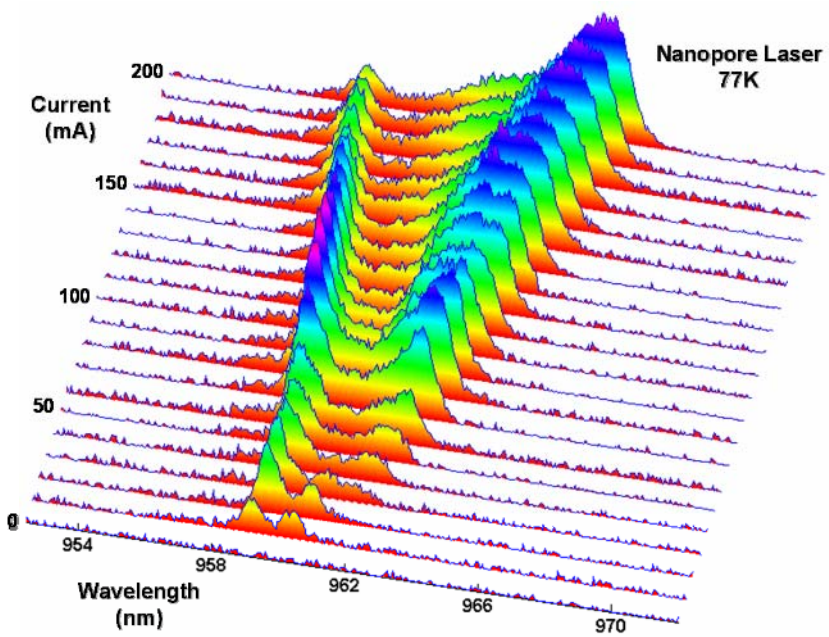

Fig. 4.11 Evolution of the emission spectrum as a function of current.

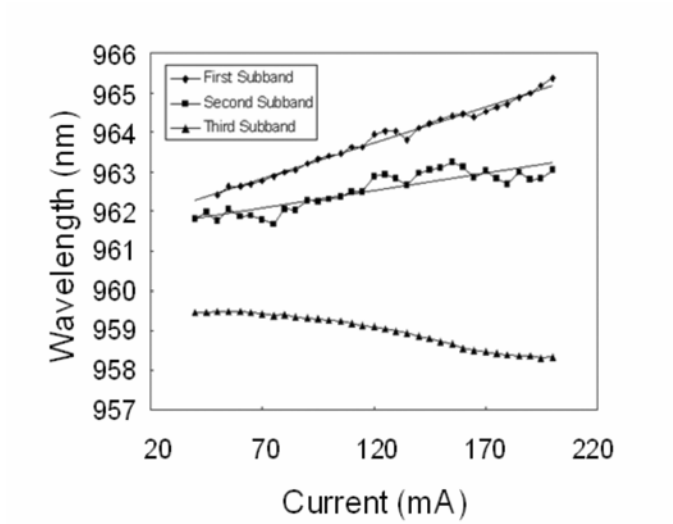

Fig. 4.12 Wavelength of each subband peak as a function of injection current. The straight line fits for the first and second subbands are guides for the eye.

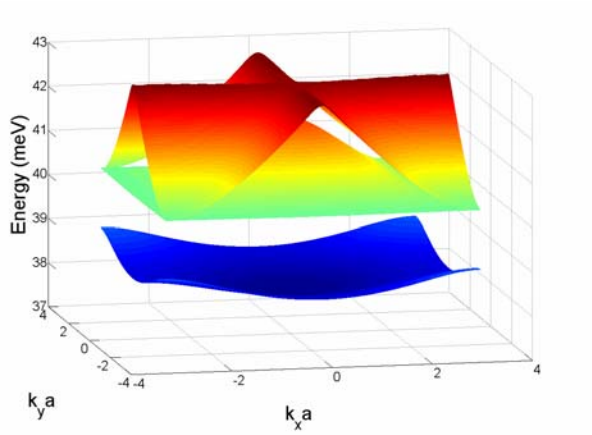

Fig. 4.13 Bandstructure for a rectangular lattice IQD array geometry with 80 nm pitch and 40 nm diameter pores.

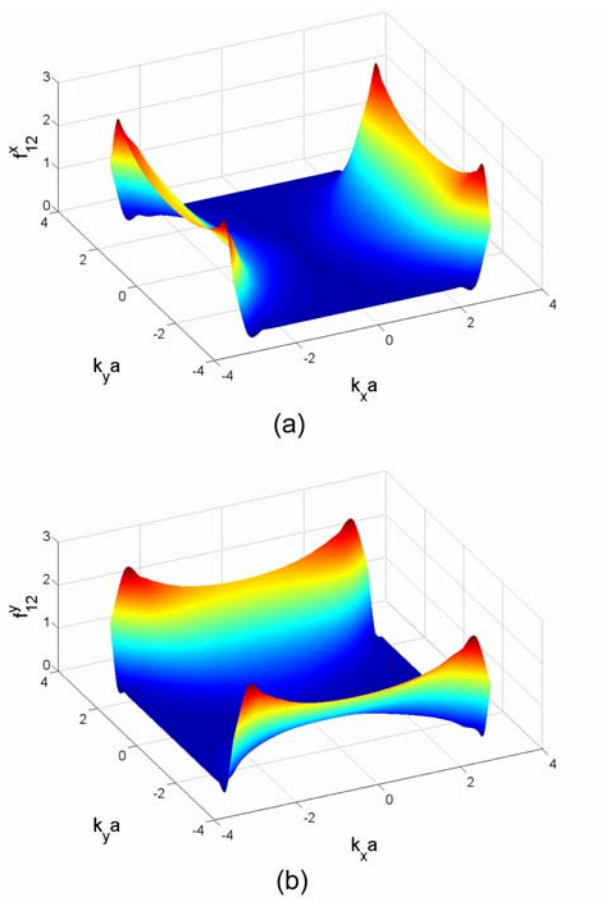

Fig. 4.14 Oscillator strength for intersubband absorption between the first and second subbands plotted over the Brillouin zone for light polarized along (a) the $\hat{\mathbf{x}}$ direction and (b) the $\hat{\mathbf{y}}$ direction.

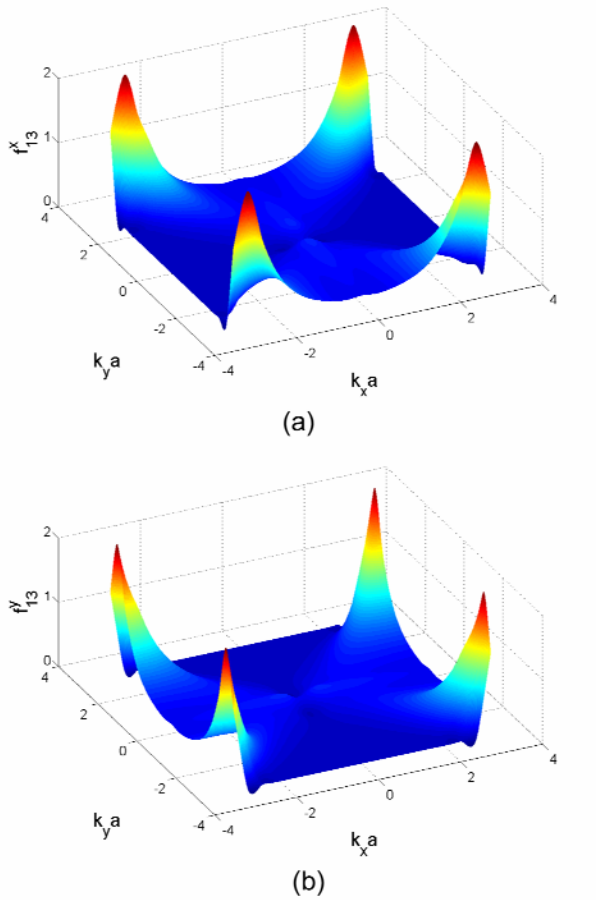

Fig. 4.15 Oscillator strength for intersubband absorption between the first and third subbands plotted over the Brillouin zone for light polarized along (a) the $\hat{\mathbf{x}}$ direction and (b) the $\hat{\mathbf{y}}$ direction.

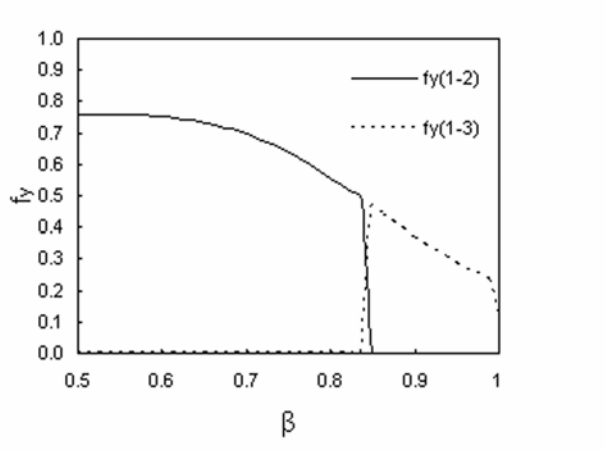

Fig. 4.16 $\hat{\mathbf{y}}$ component of the oscillator strength as a function of the rectangular lattice asymmetry factor β for the 1-2 and 1-3 intersubband transitions at the Γ point of the Brillouin zone.

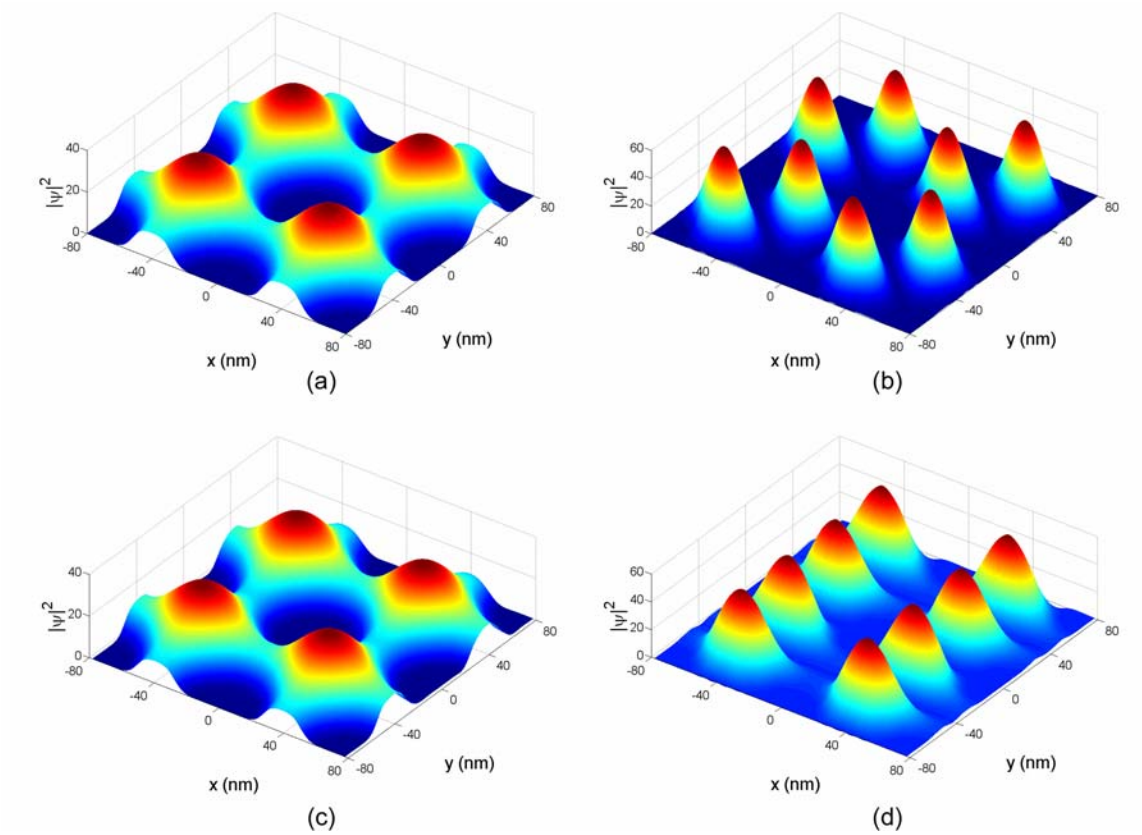

Fig. 4.17 Wavefunctions in the (a) first and (b) third subbands with $\beta = 1$ and (c) first and (d) third subbands with $\beta = 0.975$. Breaking the perfect square symmetry of the lattice results in a reorientation of the third subband wavefunction.

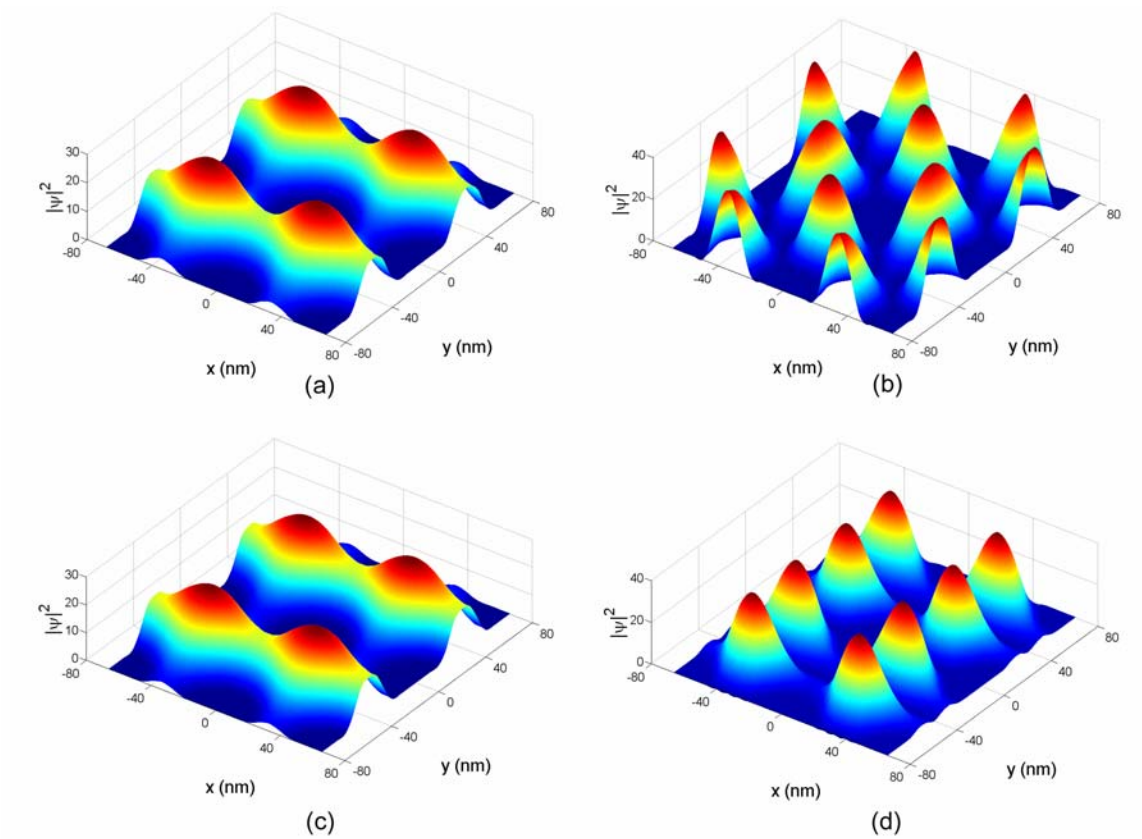

Fig. 4.18 Wavefunctions in the (a) first and (b) second subbands with $\beta = 0.85$ and (c) first and (d) second subbands with $\beta = 0.825$.

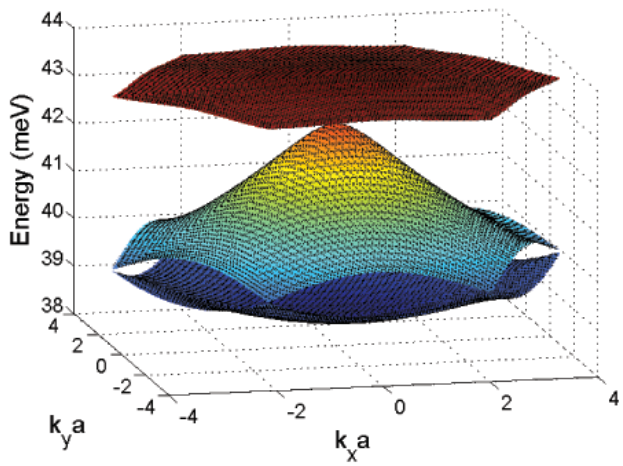

(a)

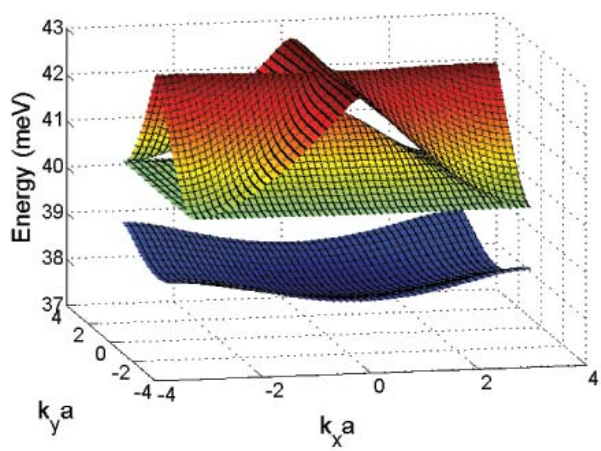

(b)

Fig. 4.19 Three-dimensional bandstructure for a unit cell with (a) triangular and (b) square geometry showing only the first three subbands for a nanopore structure with 80 nm pitch and 40 nm pore diameter.

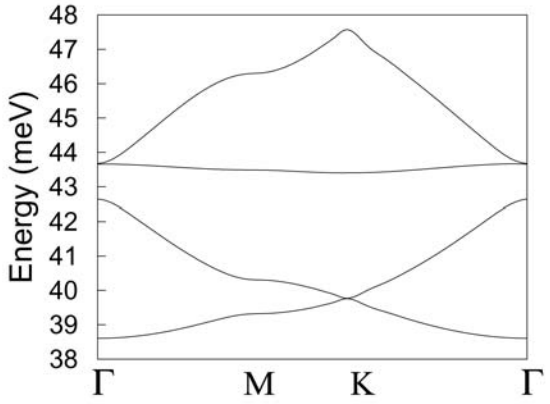

(a)

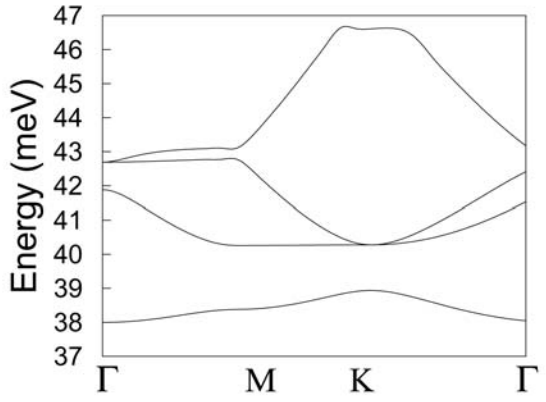

(b)

Fig. 4.20 Bandstructure along lines connecting the symmetry points in the Brillouin zone for a unit cell with (a) triangular and (b) square geometry showing the first four subbands for a nanopore structure with 80 nm pitch and 40 nm pore diameter.

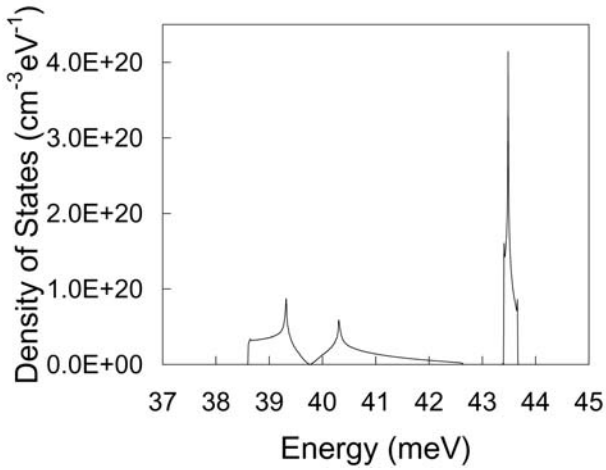

(a)

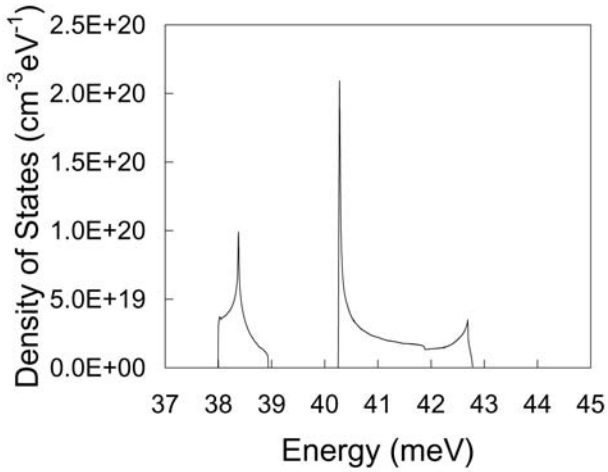

(b)

Fig. 4.21 Density of states for a nanopore lattice with (a) triangular and (b) square unit cell geometry for a nanopore structure with 80 nm pitch and 40 nm pore diameter.

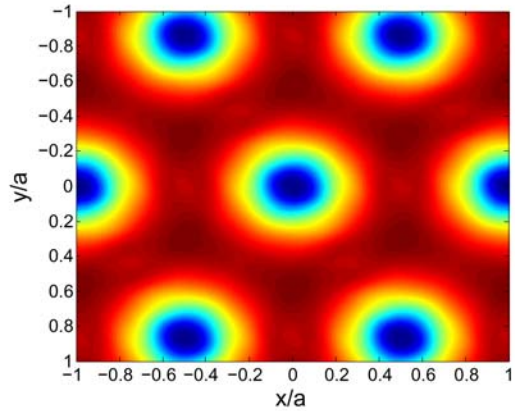

(a)

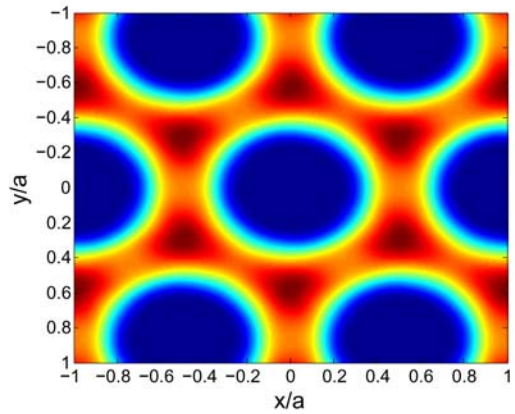

(b)

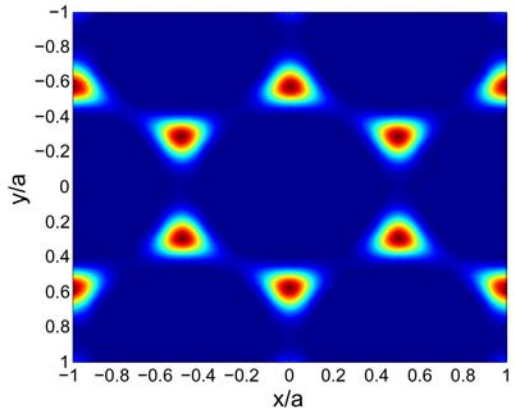

(c)

Fig. 4.22 Ground state wavefunctions of a nanopore active layer with 80 nm pitch and pore diameters of (a) 10 nm, (b) 40 nm, and (c) 70 nm.

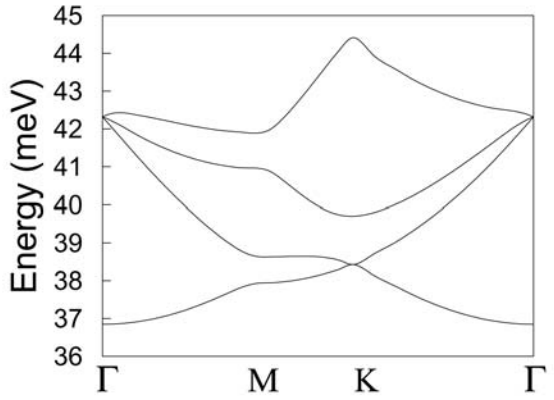

(a)

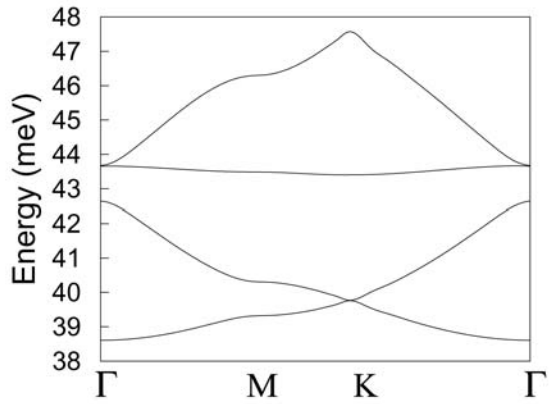

(b)

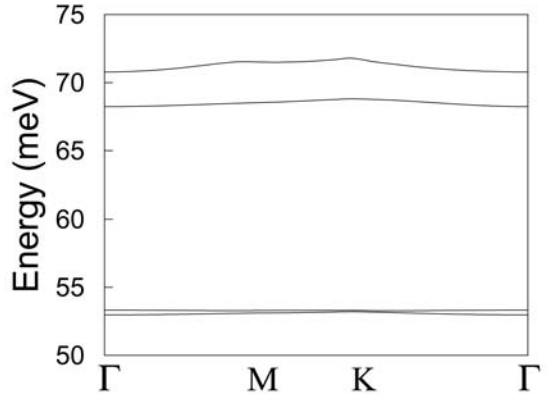

(c)

Fig. 4.23 Band diagrams of a nanopore active layer with 80 nm pitch and pore diameters of (a) 10 nm, (b) 40 nm, and (c) 70 nm showing the first four subbands.

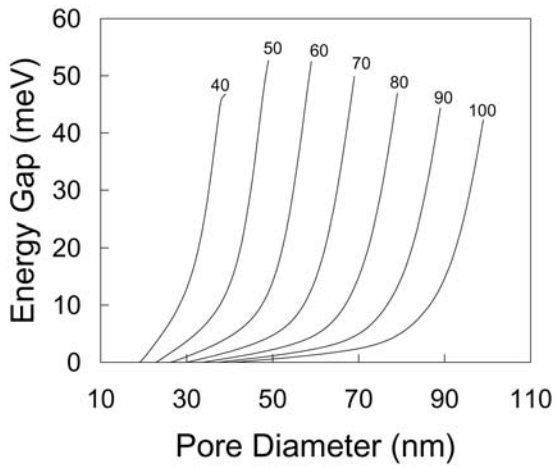

(a)

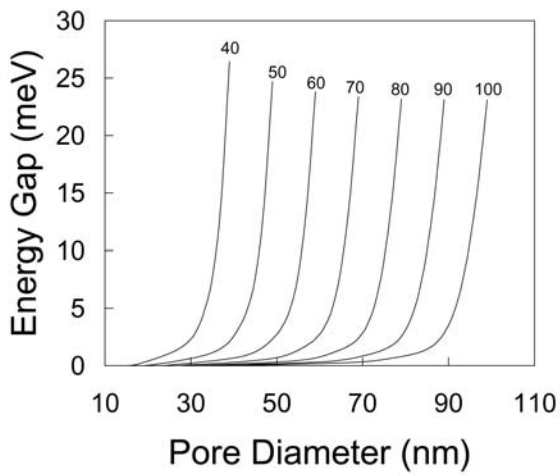

(b)

Fig. 4.24 Variation of the energy gap between the second and third subbands for (a) electrons and (b) heavy holes. The label above each curve is the lattice pitch in nanometers.

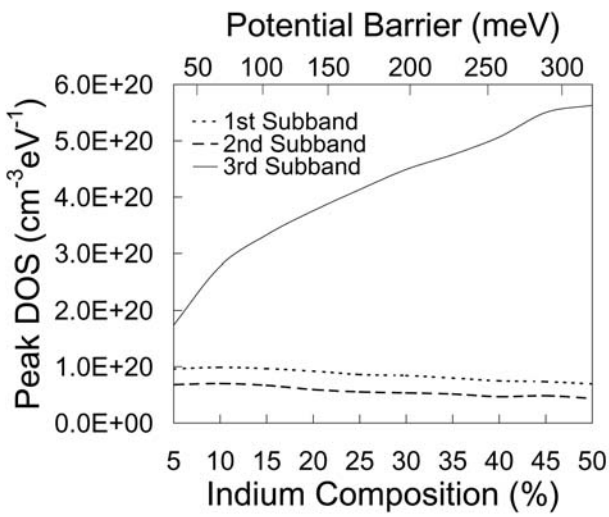

Fig. 4.25 Variation of the magnitude of the density of states for each of the first three subbands as a function of indium composition in the InGaAs layer.

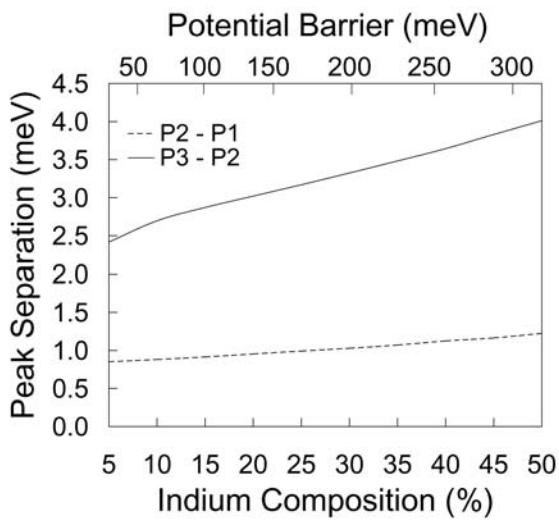

Fig. 4.26 Variation of the separation between subband peaks in the density of states as a function of indium composition in the InGaAs layer.

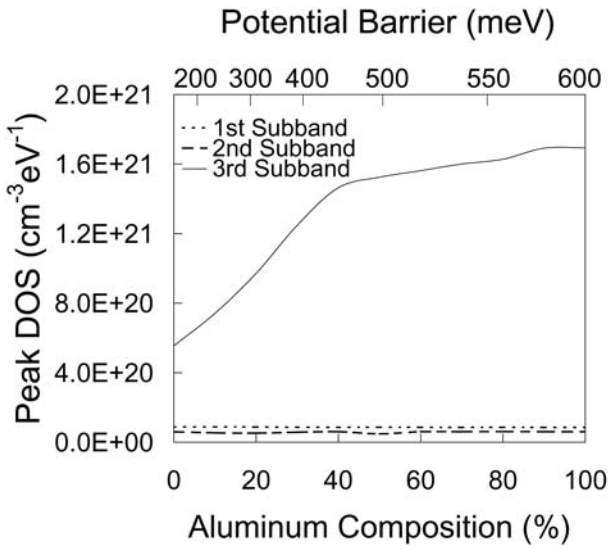

Fig. 4.27 Variation of the magnitude of the density of states for each of the first three subbands as a function of aluminum composition in the AlGaAs barrier layer.

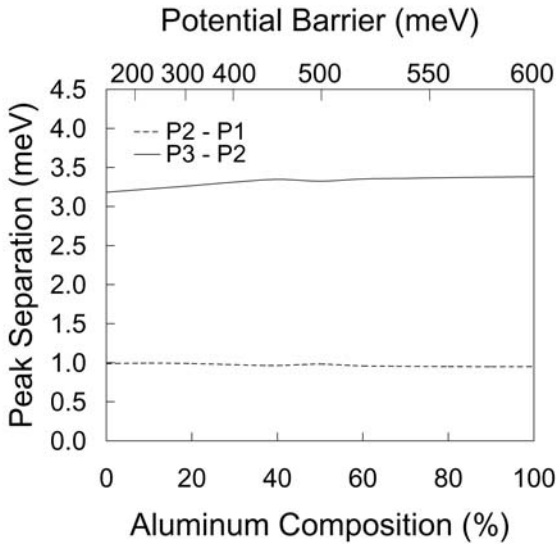

Fig. 4.28 Variation of the separation between subband peaks in the density of states as a function of aluminum composition in the AlGaAs barrier layer.

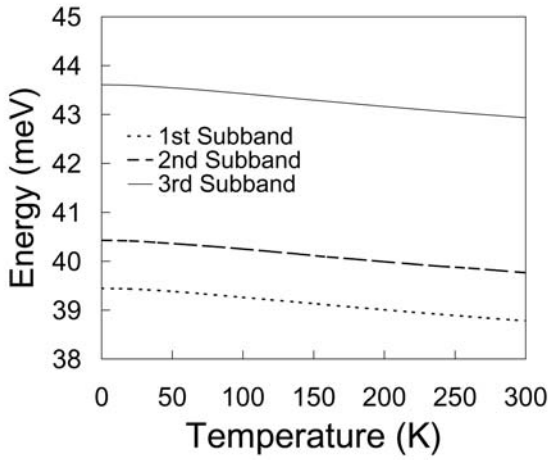

Fig. 4.29 Energy of the peak of each subband in the density of states as a function of temperature.

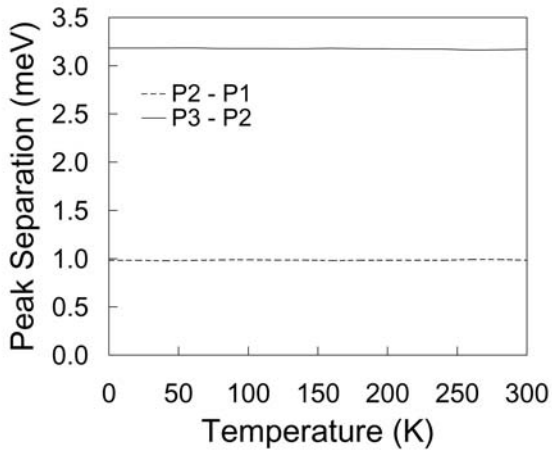

Fig. 4.30 Variation of the separation between subband peaks in the density of states as a function of temperature.

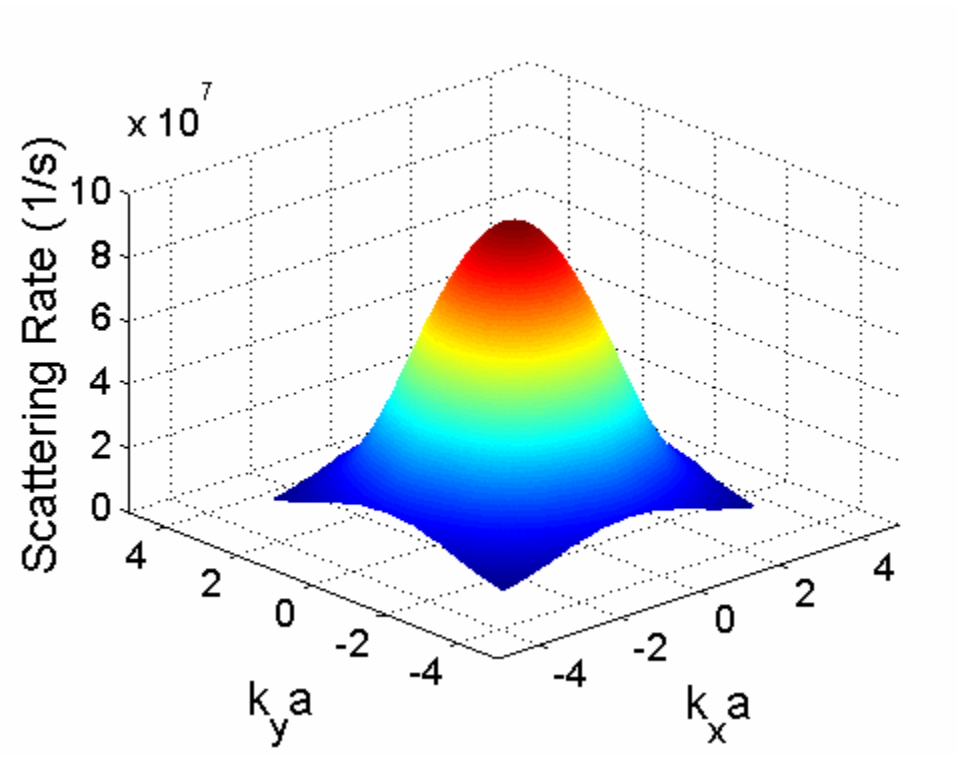

Fig. 4.31 Intersubband acoustic phonon scattering rate from the Γ point in the second longitudinal subband to each **k** point in the first longitudinal subband.

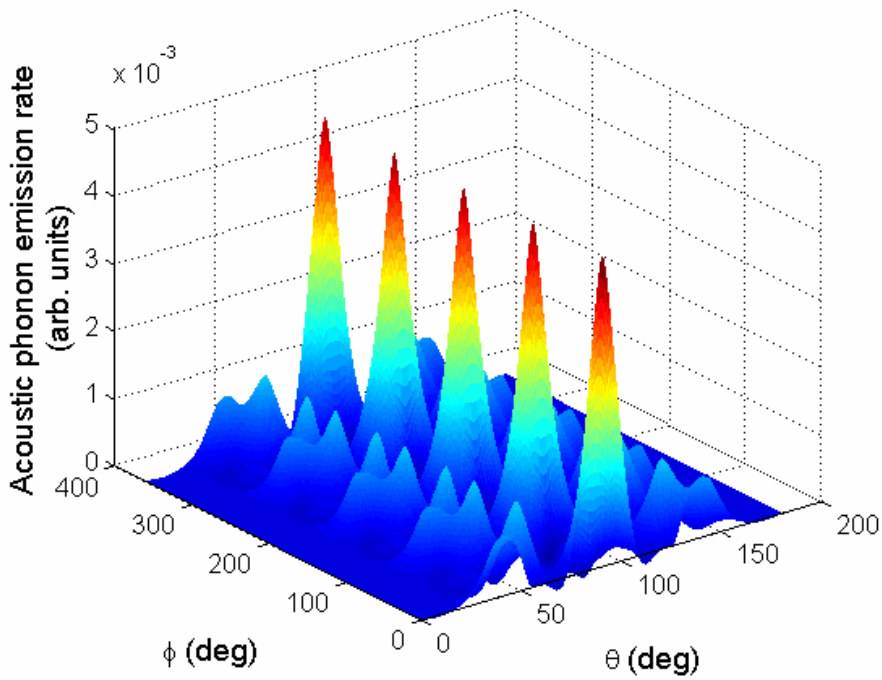

Fig. 4.32 Angular dependence of the acoustic phonon emission rate for transitions at the Γ point of the Brillouin zone between the second and first subbands.

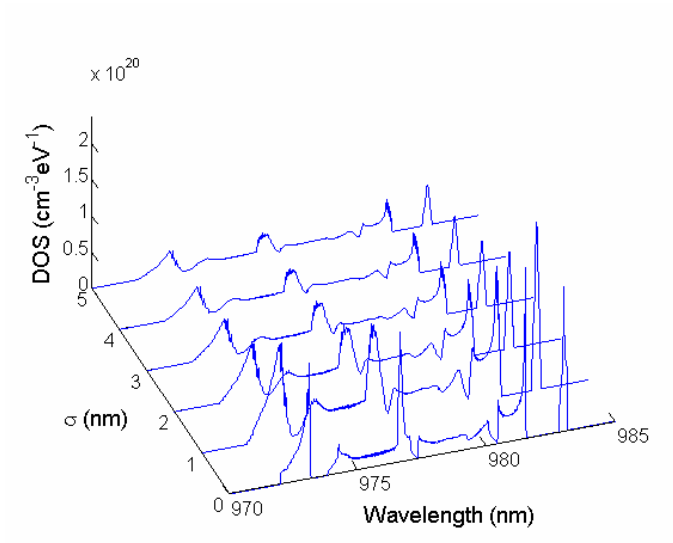

Fig. 4.33 Density of states as a function of sigma, the standard deviation of the Gaussian distribution of pore sizes with truncation points d_{max} = 61 nm, d_{min} = 59 nm.

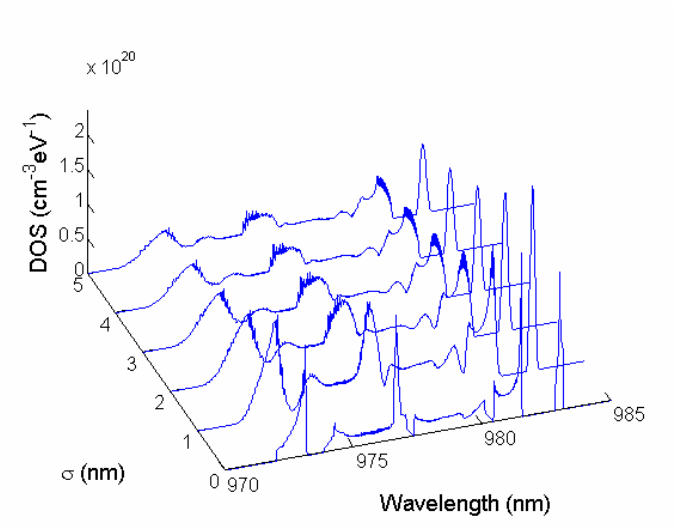

Fig. 4.34 Density of states as a function of sigma, the standard deviation of the Gaussian distribution of pore sizes with truncation points d_{max} = 63 nm, d_{min} = 57 nm.

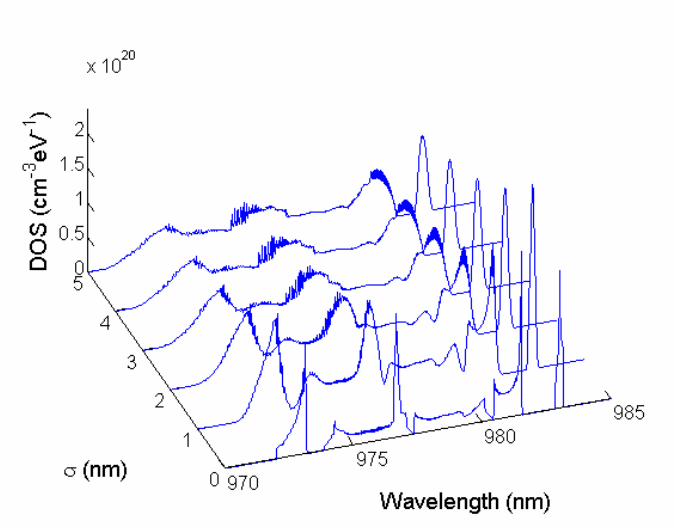

Fig. 4.35 Density of states as a function of sigma, the standard deviation of the Gaussian distribution of pore sizes with truncation points d_{max} = 65 nm, d_{min} = 55 nm.

CHAPTER 5 – NANOPORE LASERS FABRICATED BY WET-ETCHING

In Chapter 2, we outlined a fabrication technique for creating quantum dots which relies on the use of electron beam lithography in combination with wet-etching techniques, followed by regrowth of the barrier and cladding layers. This technique can easily be extended to create three-dimensional nanostructures of virtually any shape and geometry.

In Chapter 4, we showed results from a nanopore laser fabricated using the selective area epitaxy technique. This technique relies on the use of hydrogen silsesquioxane (HSQ) as a negative tone electron beam resist which serves as the growth inhibition mask in the regrowth of the quantum well material. HSQ is notoriously unreliable due to its sensitivity to oxygen and water vapor. Since electron beam lithography is an expensive process, it is highly desirable to have a repeatable process available for exploring the properties of nanopore lasers.

In this chapter, we show the results from nanopore lasers fabricated using the wet-etching technique outlined in Chapter 2. This process uses a standard positive electron beam resist (PMMA) instead of HSQ, and is very robust. Furthermore, we completely eliminate growth enhancement related effects using this technique, in addition to reducing the number of regrowths required in the laser fabrication process since the quantum well is incorporated into the base structure. In Section 5.1, we present the details of the fabrication process. In Section 5.2, we present the experimentally obtained results and compare with theoretical predictions.

5.1 Fabrication

5.1.1 Base structure growth

The base structure used for the nanopore fabrication is very similar to that used for the fabrication of quantum dots using wet etching. The structure is grown on an N+ (100) GaAs substrate, and consists of a 100 nm Si-doped n+ GaAs buffer layer, 2 μm of Si-doped n-type $Al_{0.75}Ga_{0.25}As$, 100 nm of intrinsic GaAs, a 6 nm $In_{0.27}Ga_{0.73}As$ quantum well, and a 4 nm intrinsic GaAs cap. For this experiment we doubled the thickness of the GaAs cap layer from 2 nm to 4 nm to avoid damage to the quantum well to the greatest extent possible. The structure is grown at 800 °C through the $Al_{0.75}Ga_{0.25}As$ layer and a high growth rate is used to reduce carbon incorporation which can compensate the Si dopant. At the beginning of the GaAs lower barrier growth, the temperature is then ramped down to 625 °C for the growth of the $In_{0.27}Ga_{0.73}As$ quantum well and GaAs cap layers.

5.1.2 Quantum well patterning

After growth of the base structure, the bare wafer is carefully cleaved into 12 mm x 16 mm pieces without flipping the wafer over to avoid possible scratching of the surface. Then 5 nm of SiO2 is then deposited on the samples by PECVD. This layer of oxide serves as the wet-etch mask for the underlying quantum well. After a 2 min bakeout at 200 °C, a solution of 2% PMMA in Anisole is spun on the sample at 4000 rpm to obtain a resist thickness of approximately 600 Å. The laser stripes are then patterned using electron beam lithography. The stripes are typically 3 mm long by 10 μm wide, and may consist of a lattice of dots with arbitrary size and geometry which are controlled by the electron beam dose and e-beam pattern files, respectively. Small alignment features

are also patterned using the electron beam for alignment of the ridge waveguides and vias in subsequent optical lithography steps. After exposure, the resist is developed at 10 °C in 1:2 MIBK:IPA for 3 min, followed by a 30 s rinse in IPA and gentle N_2 dry. The dot pattern in the resist is then transferred into the underlying PECVD oxide using a Freon-23 reactive ion etch. The resist is stripped for 10 min in a solution of 1:1 methylene chloride:methanol, followed by 10 min in acetone, 2 min in methanol, 2 min in IPA, and a 10 min descum in an O_2 plasma. At this stage, the sample is ready for transferring the oxide pattern into the quantum well using wet etching.

The oxide mask is very delicate, and care must be taken while handling the sample, especially during the wet-etching process itself. In order to ensure complete mixing of the etching solution while maintaining a laminar flow of reactants over the sample surface, a large 500 mL beaker is used with a magnetic stirrer placed at the bottom. The beaker is placed on a hot plate with a magnetic stirrer control and set to spin at 100 rpm. This is fast enough to ensure even distribution of the reactants while at the same time preventing damage to the delicate SiO_2 film. The sample is held exactly halfway down from the top of the beaker for the entire duration of the etch without agitation.

The wet-etching process begins with a native oxide removal in 1:10 NH_4OH:H_20 for 30 s, followed by a 10 s rinse in H_2O, and a 20 s rinse in a second H_2O bath. This step is crucial to prevent micromasking during the etching. The sample is then immediately dipped into the 500 mL beaker containing the etching solution which consists of 1:4:495 H_3PO_4:H_2O_2:H_2O.

The solution must be left to cool for 15 min before the etch is performed. This etching solution was tested for repeatability of the etch rate and was found to be very stable over the course of an hour. It was also found to yield the best results in terms of the fidelity of the pattern transfer. The etch rate should be calibrated as close to the etch of the actual sample as possible. A calibration can be performed by patterning a small piece of the base structure material with a stripe pattern and etching for a long time (>3 min). The resist can be stripped adequately by spraying with acetone and the height of the etched features can be measured with a profilometer.

After etching, the sample is again rinsed in two water baths for 10 s and 20 s. Typically after the etch there will be some oxide left on the surface from the oxidizing agent in the etching solution (H_2O_2). To obtain a pristine surface we first oxidize the entire surface by dipping the sample in 30% H2O2 for 15 s, followed by water rinses for 10 s and 20 s. The uniform layer of oxide is then removed in a solution of 1:1 HCl:H2O for 15 s, followed by 10 s and 20 s rinses. The SiO_2 mask is then stripped in a buffered hydrofluoric acid solution (BHF) for 30 s.

5.1.3 Regrowth and laser processing

After a solvent clean in acetone, methanol, and IPA, the sample is cleaned in an O_2 plasma at 300 W for 3 min. Regrowth of the upper core of the laser structure is performed at 100 mbar at 625 °C in an AIX 200/4 MOCVD reactor. The upper core consists of 90 nm of intrinsic GaAs grown at a slow growth rate of 0.2 nm/s and a V/III ratio of 50. Immediately before loading the sample into the MOCVD reactor a native oxide removal step is performed in a nitrogen-purged loadlock with a 1:10 NH_4OH:H_2O solution for 30 s, followed by a 10 s rinse in H_2O and a 20 s rinse in IPA.

Ridge waveguides of 4 μm width are then patterned over the 10 μm wide stripes containing the buried QDs using standard optical lithography techniques. The ridge waveguides are etched to a depth of 125 nm in 1:8:80 H_2SO_4:H_2O_2:H_2O. The photoresist is then removed in acetone followed by a 10 min clean in an O_2 plasma at 300 W.

Regrowth of the upper cladding and contact layers is performed at atmospheric pressure in a Thomas Swan MOCVD reactor. A native oxide removal step is performed immediately prior to loading the sample. The final regrowth consists of 10 nm of intrinsic GaAs followed by a 1.5 μm p-type $Al_{0.75}Ga_{0.25}As$ upper cladding and a 100 nm p+ GaAs contact layer, which completes the buried heterostructure laser structure shown in Fig. 3.2.

Following the upper cladding and contact layer regrowth, 3 μm wide stripes aligned over the buried 4 μm wide waveguides are etched into the p+ GaAs contact layer to reduce current spreading. Then 100 nm of SiO_2 is deposited by plasma enhanced chemical vapor deposition (PECVD), followed by optical lithography to define 2 μm wide vias over the 3 μm wide p+ GaAs stripes. The via pattern is transferred into the underlying SiO_2 using a Freon-14 reactive ion etch. P-side metals are then evaporated, followed by lapping and polishing of the substrate to a thickness of approximately 150 μm to facilitate cleaving. Finally, n-side metals are deposited and annealed, and the devices are cleaved into 1 mm long bars for testing.

5.2 Characterization and Results

Figure 5.1 shows a scanning electron micrograph of a nanopore array with a square lattice geometry with a pitch of 100 nm. Careful measurements of the pore size indicate that the pore is slightly asymmetrical and has an elliptical shape due to astigmatism of the electron beam used to write the pattern. The average major and minor axes of the ellipse are 68 nm and 57 nm, respectively.

The devices were tested in pulsed operation with a 2 μs pulse width and 0.3% duty cycle at 77 K in a liquid nitrogen cryostat. The laser emission was collected with an f/10 1 m monochromator and detected with a liquid nitrogen–cooled Ge photodiode. Figure 5.2 shows the amplified spontaneous emission collected from the laser facet from a quantum well laser fabricated as a control device on the same sample as the nanopore lasers. The device demonstrates the expected spectral narrowing near the band edge of the ground state transition at 962 nm when biased close to the threshold current of 4 mA. No emission was observed below 920 nm.

Figure 5.3 shows a plot of the amplified spontaneous emission from the nanopore laser structure shown in Fig. 5.1 at currents between 50 mA and 300 mA in 50 mA steps. We attribute the three discernible peaks to the quantum well ground state and excited state transitions, C1-HH1 (962 nm) and C2-HH2 (870 nm), and the GaAs bulk emission (845 nm). We note that although the quantum well thickness of 6 nm was designed to support only a single conduction band state, indium segregation and intermixing between the InGaAs quantum well material and GaAs barrier material during the subsequent regrowth steps may account for an increase in effective thickness, resulting in the introduction of an additional weakly bound conduction band state denoted by C2. From the plots in Fig. 5.3, it is clear that significant emission from the C2-HH2 transition is

present even before the C1-HH1 emission begins to saturate at 200 mA. Thus the population of C2 is not due to the saturation of C1 states. This suggests that there is another physical mechanism underlying the strong emission observed from the C2-HH2 transition. The reduction of intersubband scattering rates between C2 and C1 is a possible explanation for this behavior, which seems to be supported by preliminary calculations suggesting the reduction of LO phonon scattering rates by two orders of magnitude in this structure.

Figure 5.4 shows the amplified spontaneous emission spectra of the nanopore laser near threshold (320 mA) at currents of 314, 316, and 318 mA. Lasing initiates on the blue side of the spontaneous emission spectrum at 860 nm. Again, this behavior is atypical of an ordinary quantum well laser in which a spectral narrowing occurs near the band edge near threshold as shown in Fig. 5.2. Figure 5.5 shows the nanopore laser emission spectrum as a function of current above the threshold current of 320 mA. As the current is increased, lower energy subbands begin to appear. These subbands are formed within C2 through modification of the in-plane dispersion of carriers due to the two-dimensional superlattice.

If the carrier distribution were described by Fermi statistics, one would expect lasing to initiate on the lowest energy subband, followed by the appearance of high energy subbands with increasing current as the quasi Fermi level difference increases. This suggests that Fermi statistics do not accurately describe the carrier distribution. In addition, initial lasing on high energy subbands would require intersubband scattering times to be greater than the spontaneous emission lifetime which is on the order of 1 ns in a quantum well. The in-plane subbands are separated by only ~1 meV, and intersubband

scattering is dominated in this case by the interactions between carriers and acoustic phonons. Calculations indicate scattering lifetimes between these in-plane subbands of 10s of ns, much longer than the typical spontaneous emission lifetime of 1 ns.

To understand the reason for the reduced intersubband relaxation rates, we consider Fermi's rule which gives the scattering rate in terms of the matrix element of the Hamiltonian describing the interaction between a carrier and a bulk phonon:

$$\frac{1}{\tau}=\frac{2\pi}{\hbar}\sum_{f,q}\alpha^2\left(q\right)\left|\left\langle\psi_f\left|e^{i\mp\mathbf{q}\cdot\mathbf{r}}\right|\psi_i\right\rangle\right|^2\delta\left(E_f-E_i\pm E_q\right)\left[n_B\left(E_q,T_l\right)+\begin{Bmatrix}1\\0\end{Bmatrix}\right], \tag{5.1}$$

where ψ_f, ψ_i are the final and initial state wavefunctions with corresponding energies E_f and E_i, E_q is the phonon energy with wavevector **q**, n_B is the Bose-Einstein distribution for phonons given by

$$n_B(E_q,T_l)=\left[e^{E_q/k_BT_l}-1\right]^{-1}, \tag{5.2}$$

and the upper (lower) signs correspond to emission (absorption) of a phonon. The sum is performed over all possible phonon wavevectors and final states. The function $\alpha^2(q)$ is determined by the type of phonon scattering according to the interaction Hamiltonian of the electron and phonon, which takes the form

$$\alpha^2\left(q\right)=\frac{D^2}{2\rho c_s^2\Omega} \tag{5.3}$$

for acoustic phonon deformation potential scattering and

$$\alpha_i^{\,2}\left(q\right)=\frac{c_i}{\Omega q^2} \tag{5.4}$$

for polar LO phonon scattering with c_i given by

$$c_1 = \frac{2\pi e^2}{\varepsilon_\infty}\left(1-\frac{\omega_{T1}^2}{\omega_{L1}^2}\right)\frac{\omega_{T2}^2-\omega_{L1}^2}{\omega_{L2}^2-\omega_{L1}^2}$$
$$c_2 = \frac{2\pi e^2}{\varepsilon_\infty}\left(1-\frac{\omega_{T2}^2}{\omega_{L2}^2}\right)\frac{\omega_{L2}^2-\omega_{T1}^2}{\omega_{L2}^2-\omega_{L1}^2}, \tag{5.5}$$

which describes the interaction between the electron and two optical phonon branches in InGaAs.

The difference in scattering rates in the nanopore structure and an ordinary quantum well stems from the dependence of the matrix element in Eq. (5.1) on the initial and final wavefunctions. The introduction of the periodic in-plane potential barriers alters the in-plane component of the envelope functions ψ_f and ψ_i, which are no longer plane waves as in an ordinary quantum well. In principle this can give rise to a significant reduction in the magnitude of the matrix element in Eq. (5.1), resulting in a reduced scattering rate between subbands resulting from in-plane quantization. A similar effect has been used in quantum cascade lasers to engineer subband lifetimes for the purpose of achieving intersubband population inversion and efficient carrier extraction. The experimental results we have presented suggest that the same effect is present in a two-dimensional planar superlattice, as opposed to the one-dimensional superlattice used in a quantum cascade laser.

Figure 5.6 shows the conduction band energy dispersion diagram for the square lattice nanopore device with 100 nm pitch in Fig. 5.1. Figure 5.7 shows the joint density of states between the conduction and valence subbands taking into account the selection rules and dipole matrix elements for each transition. The potential barrier height for electrons was fixed at 7 meV for the simulation of the conduction band dispersion diagram. This small potential barrier height results from the close proximity of C2 to the

GaAs conduction band edge, and it is a critical parameter in the simulation since small changes in potential barrier height in this range can significantly alter the in-plane dispersion. The heavy hole potential barrier height is much larger because HH2 is well-confined, and the dispersion is relatively insensitive to small variations in the barrier height. Again, the pores were assumed to be elliptical with major and minor axes of 68 nm and 57 nm, respectively. Figure 5.8 shows the experimentally obtained spectrum at a current of 495 mA measured in pulsed operation at 77 K.

Figure 5.9 shows another nanopore structure with 80 nm diameter pitch and 55 nm diameter pores. Figures 5.10 and 5.11 show the conduction band energy dispersion diagram and joint density of states, respectively, for this particular structure. The potential barrier height for electrons was fixed at 4 meV for the simulation of the conduction band dispersion diagram. The pores were assumed to be perfectly circular, which is supported by the scanning electron micrograph in Fig. 5.9. Figure 5.12 shows the experimentally measured laser spectrum at 410 mA measured in pulsed operation at 77 K. The disparity in the wavelengths of the experimental and theoretical spectra likely results from solid phase mass transport which occurs during the initial heating of the sample for the barrier layer regrowth, in addition to intermixing with the barrier material during the regrowth steps.

From these two examples we have shown that the density of states can be engineered through control over the pitch and pore size in the nanopore lattice geometry.

5.3 Figures

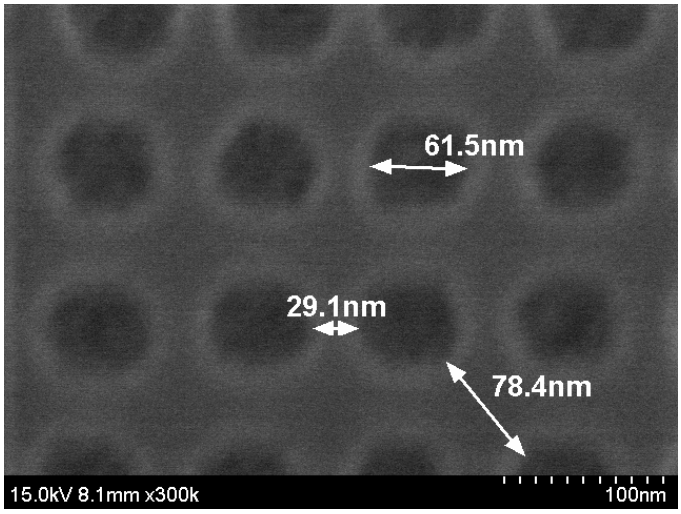

(a)

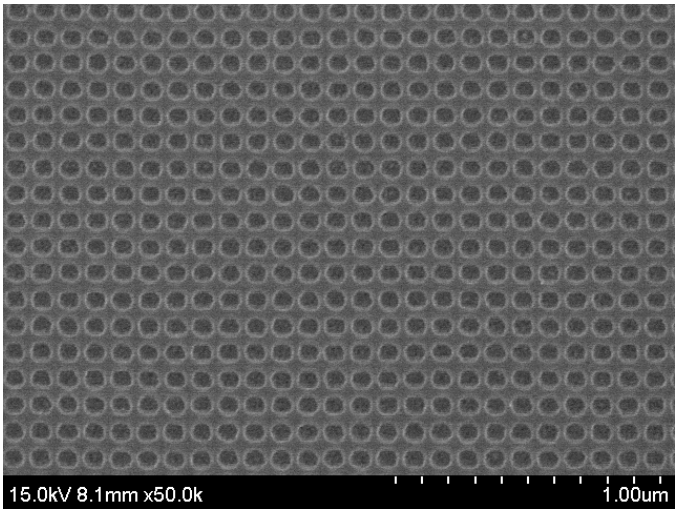

(b)

Fig. 5.1 Scanning electron micrograph of a nanopore array fabricated by wet etching at a magnification of (a) 300k and (b) 50k.

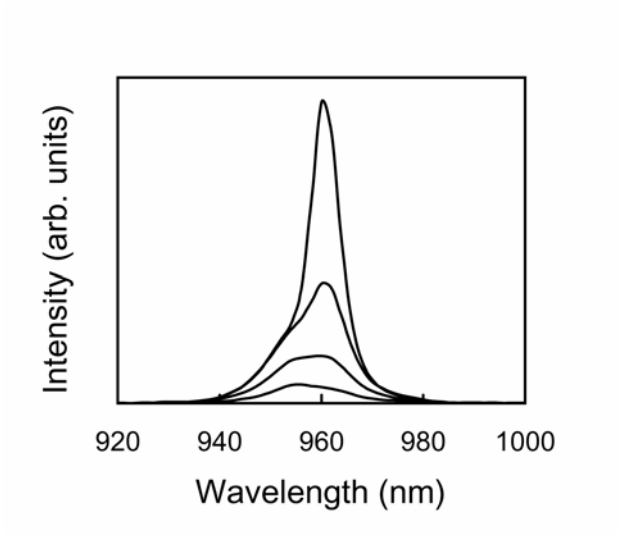

Fig. 5.2 Amplified spontaneous emission spectrum for a quantum well laser fabricated on the same sample as the nanopore lasers between currents of 1 mA and 2.5 mA in 0.5 mA steps.

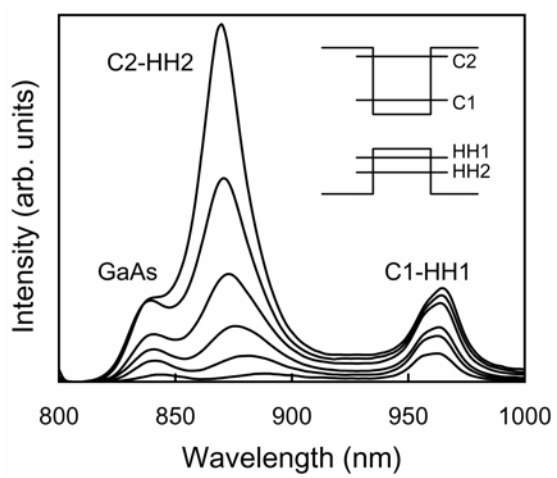

Fig. 5.3 Spontaneous emission spectrum between currents of 50 mA and 300 mA in 50 mA steps from a nanopore laser with geometry shown in Fig. 1. The inset shows a diagram of the quantum well confined states.

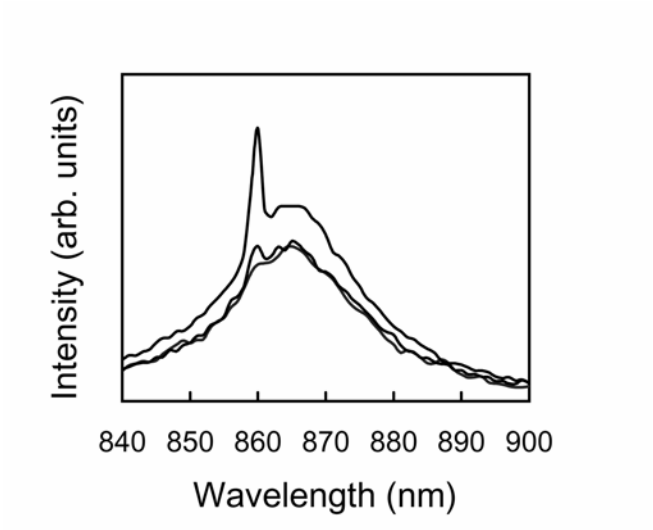

Fig. 5.4 Amplified spontaneous emission spectrum near laser threshold at currents of 314, 316, and 318 mA.

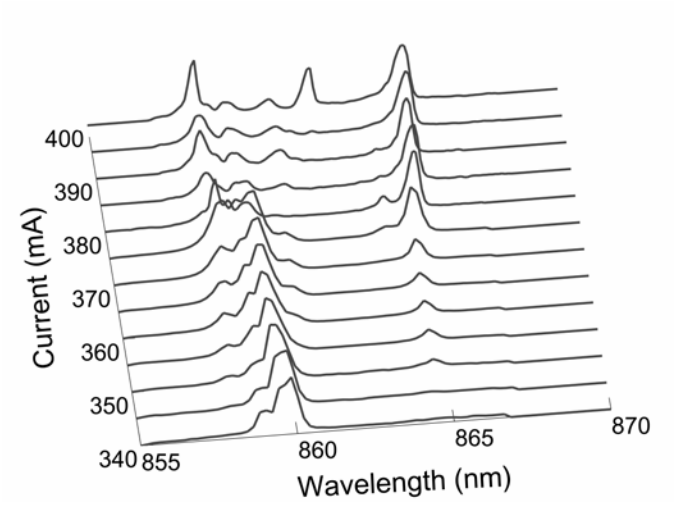

Fig. 5.5 Nanopore laser emission spectrum as a function of current above threshold.

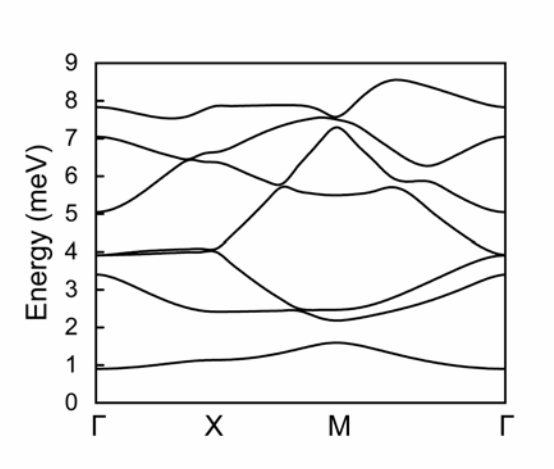

Fig. 5.6 Conduction band dispersion diagram for the nanopore lattice shown in Fig. 5.1.

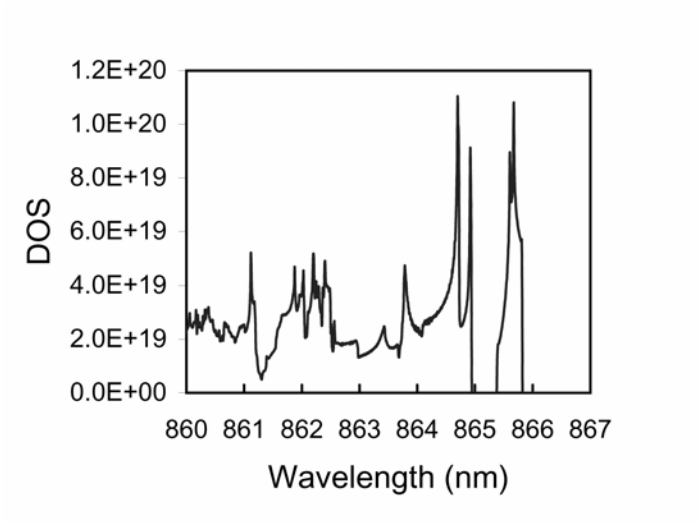

Fig. 5.7 Calculated joint density of states for the nanopore lattice shown in Fig. 5.1.

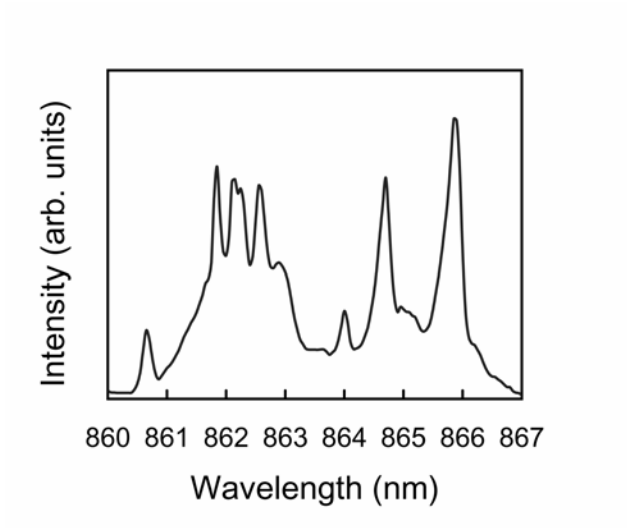

Fig. 5.8 Experimentally measured laser spectrum from the nanopore laser device shown in Fig. 5.1.

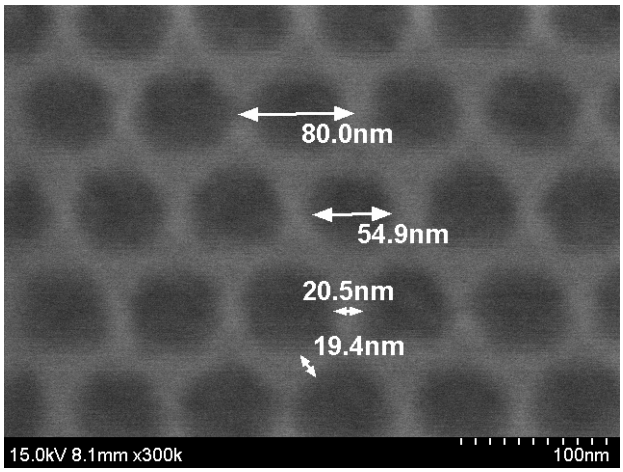

(a)

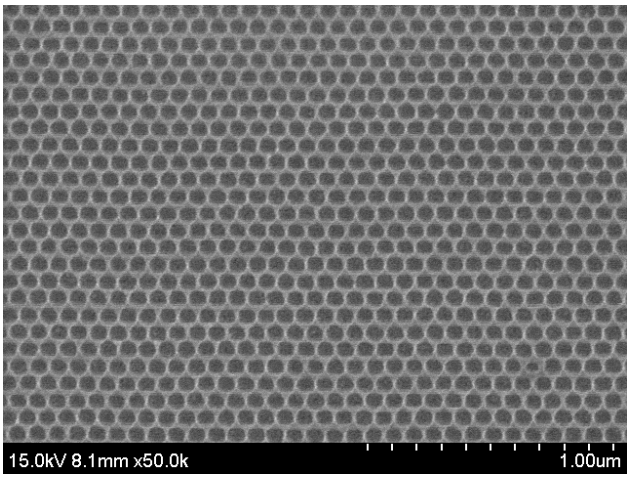

(b)

Fig. 5.9 Scanning electron micrograph of a nanopore array fabricated by wet etching at a magnification of (a) 300k and (b) 50k.

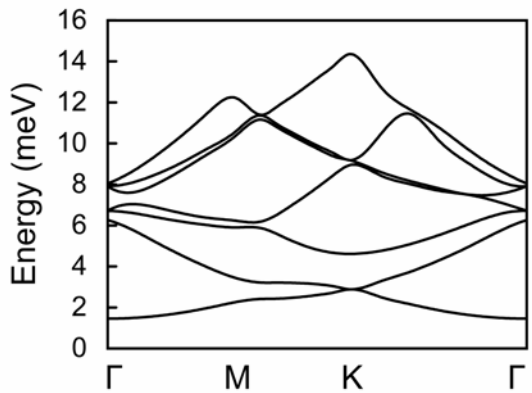

Fig. 5.10 Conduction band dispersion diagram for the nanopore lattice shown in Fig. 5.9.

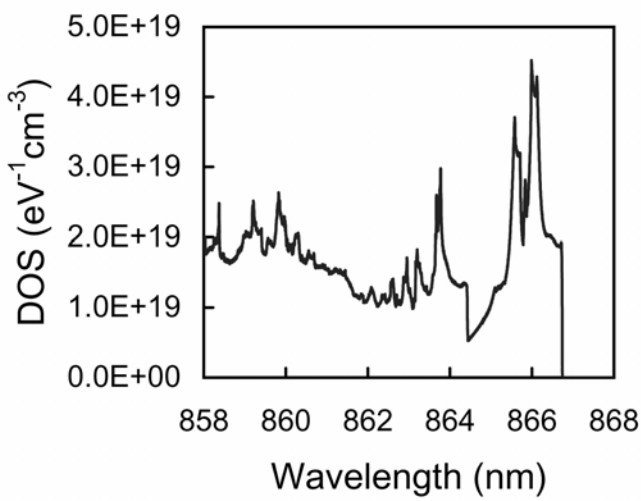

Fig. 5.11 Calculated joint density of states for the nanopore lattice shown in Fig. 5.9.

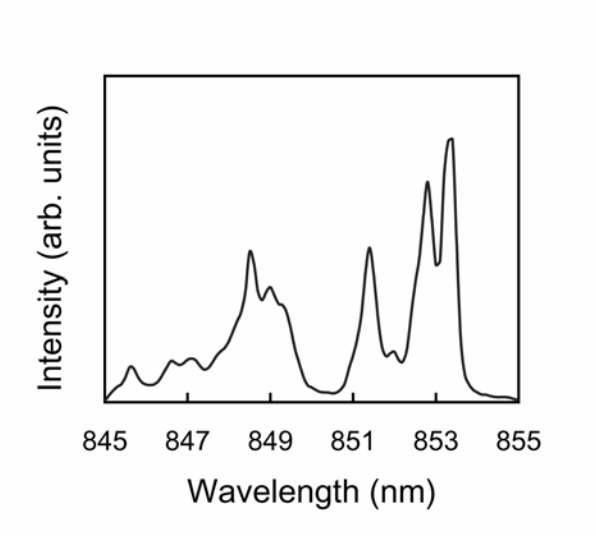

Fig. 5.12 Calculated joint density of states for the nanopore lattice shown in Fig. 5.9.

CHAPTER 6 – CONCLUSION

In this work we have demonstrated a new technique for the fabrication of high optical quality quantum dots. This technique relies on patterning by electron beam lithography and nanoscale wet-etching of a preexisting two-dimensional quantum well. Quantum dots fabricated using this technique have been shown to possess superior characteristics to quantum dots patterned using the selective area growth technique due to a reduction in inhomogeneous broadening caused by growth and composition enhancement effects. The incorporation of these quantum dots into a laser device demonstrates that the dots are of high optical quality and suitable for use in any type of photonic device. The ability to determine a priori the emission wavelength of the quantum dot by tuning the indium composition and thickness of the quantum well prior to etching should prove useful for applications requiring the spectral and spatial alignment of a quantum dot with an optical microcavity. Such systems have been demonstrated as sources of single photons and entangled photons using self-assembled quantum dots with very low yield. The ability to spatially position a quantum dot as outlined in this document could potentially improve the yield of this type of device to 100%.

We have also presented a theoretical model for the nanopore active layer, which appears to accurately reproduce the spectral characteristics of the fabricated devices. These lasers have been shown to possess interesting characteristics such as “top-down” lasing and enhanced emission of excited states relative to the ground state. Although these properties are in general not desirable for an interband laser, they could be very desirable in the utilization of the nanopore active layer in intersubband devices. In addition, we have shown that the wet-etching technique is also capable of producing a

nanopore laser device with the expected spectral characteristics. This process is much more robust and repeatable than the the HSQ-based process.

APPENDIX A - CODE LISTING FOR NANOPORE ANALYSIS

This section contains the computer code used in the analysis of the nanopore active layer. All files were written using MATLAB.

ComputeIMatrixSquare.m

```
%Computes integration over nanopore for square lattice unit cell geometry
%Generates I Matrix used to calculate Hamiltonian in program used
%to calculate bandstructure

clear all;

a = 100; %Lattice constant in x
b = 100; %Lattice constant in y
gamma = a/b;
N = 9; % MUST be an ODD NUMBER
Nz = 9; %MUST be an ODD NUMBER
Ngtot = N^2*Nz;
d = 55; %pore diameter
diameter = d/a;
radius = diameter/2;


%Compute reciprocal space vectors G
mid = (N+1)/2;
for p=1:N
    for q=1:N
        for r=1:Nz
        G(r+((p-1)+(q-1)*N)*Nz,1) = (p-mid);
        G(r+((p-1)+(q-1)*N)*Nz,2) = (mid-q)*gamma;
        G(r+((p-1)+(q-1)*N)*Nz,3) = r;
        end
    end
end



index = 1;
for p=1:Ngtot
  for q=p:Ngtot
        A = 2*pi*(G(q,1)-G(p,1));
        B = 2*pi*(G(q,2)-G(p,2));
        C = sqrt(A^2+B^2);
        if C==0
            I(p,q) = pi*radius^2;
        else
            I(p,q) = 2*pi*radius*besselj(1,radius*C)/C;
        end
  end
end
%extract diagonal elements
v = diag(I,0);

%create a diagonal matrix with these elements
Idiag = diag(v);

%Add I (upper triangular) to its conjugate transpose and subtract the
%diagonal elements to account for adding them twice.
I = I'+I-Idiag;

path = strcat('C:\IM', num2str(a), num2str(b), num2str(d), 'N9Nz9.txt');
save (path, 'I', '-ASCII');
path = strcat('C:\IM', num2str(a), num2str(b), num2str(d), 'N9Nz9.mat');
save (path, 'I', '-mat');
```

ComputeIMatrixHex.m

```
%Computes integration over nanopore for triangular lattice unit cell geometry
%Generates I Matrix used to calculate Hamiltonian in program used
%to calculate bandstructure

clear all;

a = 100; %Lattice constant in x
b = 100; %Lattice constant in y
N = 9; % MUST be an ODD NUMBER
Nz = 9; %MUST be an ODD NUMBER
Ngtot = N^2*Nz;
d = 55; %pore diameter
diameter = d/a;
radius = diameter/2;


%Compute reciprocal space vectors G
mid = (N+1)/2;
for p=1:N
    for q=1:N
        for r=1:Nz
        G(r+((p-1)+(q-1)*N)*Nz,1) = (p-mid);
        G(r+((p-1)+(q-1)*N)*Nz,2) = (mid-q);
        G(r+((p-1)+(q-1)*N)*Nz,3) = r;
        end
    end
end



index = 1;
for p=1:Ngtot
  for q=p:Ngtot
        A = 2*pi*(G(q,1)-G(p,1));
        B = 2*pi*((2/sqrt(3)*(G(q,2)-G(p,2))-1/sqrt(3)*(G(q,1)-G(p,1))));
        C = sqrt(A^2+B^2);
        if C==0
            I(p,q) = 4*pi/sqrt(3)*radius^2/2;
        else
```

```
98                I(p,q) = 4*pi/sqrt(3)*radius*besselj(1,radius*C)/C;
99            end
100     end
101   end
102   %extract diagonal elements
103   v = diag(I,0);
104
105   %create a diagonal matrix with these elements
106   Idiag = diag(v);
107
108   %Add I (upper triangular) to its conjugate transpose and subtract the
109   %diagonal elements to account for adding them twice.
110   I = I'+I-Idiag;
111
112   path = strcat('C:\IM', num2str(a), num2str(b), num2str(d), 'N9Nz9.txt');
113   save (path, 'I', '-ASCII');
114   path = strcat('C:\IM', num2str(a), num2str(b), num2str(d), 'N9Nz9.mat');
115   save (path, 'I', '-mat');
```

Nporehex3De.m

```
1     %nporehex3De.m
2     %Computes system Hamiltonian and eigenvectors, eigenvalues
3     %Takes I Matrix as an input
4
5     clear all;
6
7     %define global variables
8     global mwe;
9     global mwh;
10    global mbe;
11    global mbh;
12    global V0e;
13    global Egw;
14    global Egb;
15    global a;
16    global diameter;
17    global radius;
18    global N;
19    global q;
20    global alphastep;
21    global betastep;
22    global beta;
23    global alpha;
24    global kstepbeta;
25    global kstepalpha;
26    global alphaindex;
27    global betaindex;
28    global Nalpha;
29    global V;
30    global IX;
31    global G;
32    global alphaindex;
33    global betaindex;
34    global L;
35
36    %define constants
37    hbar = 1.054*10^-34;
38    e = 1.6*10^-19;
39    me = 9.11*10^-31;
40    InAsac = -5.08;
41    InAsav = 1.00;
42    InAsb = -1.8;
43    InAsd = -3.6;
44    InAsC11 = 8.329;
45    InAsC12 = 4.526;
46    InAsa0 = 6.0584;
47    GaAsac = -7.17;
48    GaAsav = 1.16;
49    GaAsb = -1.7;
50    GaAsd = -4.55;
51    GaAsC11 = 11.879;
52    GaAsC12 = 5.376;
53    GaAsa0 = 5.6533;
54
55    %define local variables
56    T = 77; %temp
57    c = 0.25; %Indium composition
58    a = 100;  %lattice pitch
59    L= 10;    %QW thickness
60    s = 5*L;  %thickness of unit cell in transverse (z) dimension
61
62    diameter = 40/a; %nanopore diameter
63    s = s/a;         %normalize vars to lattice pitch
64    L=L/a;
65    radius = diameter/2;
66    N = 9; %Number of reciprocal space basis vectors MUST be an ODD NUMBER
67    Nz = 9; %Number of reciprocal space basis vectors MUST be an ODD NUMBER
68
69    %Define dependent variables
70    Ry = hbar^2/(e*me*(a*10^-9)^2); %Energy constant
71    Egb = 1.519-5.405e-4*T^2/(T+204); %barrier material bandgap
72    Egw = 0.42+0.625*(1-c)-(5.8/(T+300)-4.19/(T+273))*0.0001*T*T*(1-c) ...
73        -0.000419*T*T/(T+271)+0.475*(1-c)*(1-c); %QW material bandgap
74    mwe = 0.023+0.037*(1-c)+0.003*(1-c)^2; %electron effective mass in QW
75    mbe = 0.067; %electron effective mass in barrier
76    mwh = 0.41+0.1*(1-c); %hole effective mass in QW
77    mbh = 0.51; %hole effective mass in barrier
78
79    %Calculate strained bandgaps
80    a0 = c*InAsa0+(1-c)*GaAsa0;
81    av = c*InAsav+(1-c)*GaAsav;
82    ac = c*InAsac+(1-c)*GaAsac;
83    b = c*InAsb+(1-c)*GaAsb;
84    d = c*InAsd+(1-c)*GaAsd;
```

```
C11 = c*InAsC11 + (1-c)*GaAsC11;
C12 = c*InAsC12 + (1-c)*GaAsC12;
e0 = (GaAsa0-a0)/GaAsa0;
exxresult = e0;
eyyresult = e0;
ezzresult = -2*C12/C11*e0;
cbresultw = ac*(exxresult+eyyresult+ezzresult);
P = -av*(exxresult+eyyresult+ezzresult);
Q = -b/2*(exxresult+eyyresult-2*ezzresult);
Rsquared = 0.75*b*b*(exxresult-eyyresult)*(exxresult-eyyresult);
if(Q<0)
    sgnQ=-1;
else
    sgnQ=1;
end
hhresultw = -P-sgnQ*sqrt(Q*Q+Rsquared);
Egwstrainedhh = Egw+(cbresultw-hhresultw); %strained QW bandgap
Egbstrained = Egb; %strained barrier bandgap
V0e = (0.6*(Egbstrained-Egwstrainedhh))/Ry; %potential barrier electrons
V0hh = (0.4*(Egbstrained-Egwstrainedhh))/Ry; %potential barrier holes

%Compute reciprocal space vectors G
mid = (N+1)/2;
for p=1:N
    for q=1:N
        for r=1:Nz
        G(r+((p-1)+(q-1)*N)*Nz,1) = 2*pi*(p-mid);
        G(r+((p-1)+(q-1)*N)*Nz,2) = 2*pi*(mid-q);
        G(r+((p-1)+(q-1)*N)*Nz,3) = r;
        end
    end
end
%Load I matrix for computation of Hamiltonian
I = load('C:\IMatrix.txt');

Ngtot = N^2*Nz; %total number of reciprocal space basis vectors
Nalpha = 10; %number of points along the line connecting Gamma->K in BZ
index = 1;
alphaindex = 1;
betaindex = 1;
kstepalpha = (4*pi/3)/(Nalpha-1); % (4*pi/3) is the distance in kspace from Gamma to K.
kstepbeta = kstepalpha*sqrt(3)/2;
alphastep = kstepalpha/(2*pi);
betastep = kstepbeta*sqrt(3)/(4*pi);
%Loop over k-point grid in irreducible wedge of BZ
for alpha = 0:alphastep:(2/3)
    for beta = 0:betastep:0.25*(2-3*alpha)
        kn = 2*pi*(alpha+beta);
        km = 2*pi*0.5*alpha;
 % Compute Hamiltonian
 for p=1:Ngtot
    for q=1:Ngtot
      Iterm = I(p,q);
      elem = (2/3)*(((kn)^2+(km)^2-(km)*(kn))+((G(q,1))^2+(G(q,2))^2-(G(q,2))*(G(q,1)))+((kn)*(2*(G(q,1))-(G(q,2)))+(km)*(2*(G(q,2))-(G(q,1)))))+(1/2)*(G(q,3)*pi/s)^2;
if(G(q,3)==G(p,3))
Zterm = L/s + (sin(pi*G(q,3)*(1-L/s))-sin(pi*G(q,3)*(1+L/s)))/(2*pi*G(q,3));
else
Zterm = (sin((G(q,3)+G(p,3))*pi/2*(1-L/s))-sin((G(q,3)+G(p,3))*pi/2*(1+L/s)))/(pi*(G(q,3)+G(p,3)))-(sin((G(q,3)-G(p,3))*pi/2*(1-L/s))-sin((G(q,3)-G(p,3))*pi/2*(1+L/s)))/(pi*(G(q,3)-G(p,3)));
end
H(p,q) = elem*Zterm*((1/mbe)-(1/mwe))*Iterm+V0e*Zterm*Iterm;
if(G(p,1)==G(q,1) && G(p,2)==G(q,2))
H(p,q) = H(p,q) + elem*Zterm*((1/mwe)-(1/mbe)) - V0e*Zterm;
end
if(p==q)
  H(p,q) = H(p,q) + elem*(1/mbe)+ V0e;
end
end
end
%Compute eigenvectors, eigenvalues of Hamiltonian and save to files
[V,D] = eig(H);
Ddiag = diag(D);
d = real(Ddiag.*1000.*Ry);
[D,IX] = sort(d);
Epath = strcat('C:\EData\E', num2str(index), '.txt');
Hpath = strcat('C:\HData\H',  num2str(index), '.txt');
Vpath = strcat('C:\VData\V',  num2str(index), '.txt');
IXpath = strcat('C:\IXData\IX',  num2str(index), '.txt');

save (Epath, 'D', '-ASCII');
save (Vpath, 'V', '-ASCII');
save (Hpath, 'H', '-ASCII');
save (IXpath, 'IX', '-ASCII');

%write current kx,ky values to an array
kx1(index) = 0.5*kstepalpha*(alphaindex-1);
ky1(index) = kstepbeta*(betaindex-1);
index = index + 1;
betaindex = betaindex + 1;
end
alphaindex = alphaindex+1;
betaindex = alphaindex;
end

%save kx, ky arrays to files
save('C:\KData\', 'kx1', '-ASCII');
save('C:\KData\', 'ky1', '-ASCII');
```

Nporesquare3De.m

```
%nporesquare3De.m
%calculates the eigenvalues of the Hamiltonian for a square lattice
%geometry with arbitrary symmetry

clear all;

global mwe;
global mwh;
global mbe;
global mbh;
global V0e;
global Egw;
global Egb;
global a;
global N;
global q;
global Nalpha;
global V;
global IX;
global G;
global L;

%Constants
hbar = 1.054*10^-34;
e = 1.6*10^-19;
me = 9.11*10^-31;
InAsac = -5.08;
InAsav = 1.00;
InAsb = -1.8;
InAsd = -3.6;
InAsC11 = 8.329;
InAsC12 = 4.526;
InAsa0 = 6.0584;
GaAsac = -7.17;
GaAsav = 1.16;
GaAsb = -1.7;
GaAsd = -4.55;
GaAsC11 = 11.879;
GaAsC12 = 5.376;
GaAsa0 = 5.6533;

%Constants
T = 77;         %temperature
c = 0.265;      %Indium composition

apitch = 80;    %pitch in x dimension
bpitch = 80;    %pitch in y dimension
a = apitch;
minor = 60;     %minor axis dimension of nanopore
major = 60;     %major axis dimension of nanopore
gamma = apitch/bpitch;
L = 8;        %quantum well width
s = 3*L;

s = s/a;
L=L/a;
N = 9;  %MUST be an ODD NUMBER
Nz = 9; %MUST be an ODD NUMBER

Ry = hbar^2/(e*me*(a*10^-9)^2);     %Energy normalization constant
Egb = 1.519-5.405e-4*T^2/(T+204);   %Barrier band gap energy
Egw = 0.42+0.625*(1-c)-(5.8/(T+300)-4.19/(T+273))*0.0001*T*T*(1-c)-0.000419*T*T/(T+271)+0.475*(1-c)*(1-c); %QW bandgap energy
mwe = 0.023+0.037*(1-c)+0.003*(1-c)^2;  %electron mass in QW
mbe = 0.067;                            %electron mass in barrier
mwh = 0.41+0.1*(1-c);                   %heavy hole mass in QW
mbh = 0.51;                             %heavy hole mass in barrier

%Calculate strained bandgaps
a0 = c*InAsa0+(1-c)*GaAsa0;                 %interpolate InGaAs lattice constant
av = c*InAsav+(1-c)*GaAsav;                 %interpolate InGaAs valence band deformation potential
ac = c*InAsac+(1-c)*GaAsac;                 %interpolate InGaAs conduction band deformation potential
b = c*InAsb+(1-c)*GaAsb;                    %interpolate InGaAs shear deformation potential
d = c*InAsd+(1-c)*GaAsd;                    %interpolate InGaAs shear deformation potential
C11 = c*InAsC11 + (1-c)*GaAsC11;            %interpolate InGaAs elastic constant C11
C12 = c*InAsC12 + (1-c)*GaAsC12;            %interpolate InGaAs elastic constant C12
e0 = (GaAsa0-a0)/GaAsa0;                    %compute misfit strain
delEhy = -2*(ac-av)*(C11-C12)/C11*e0;
delEsh = -2*b*(C11+2*C12)/C11*e0;
Egwstrainedhh = Egw-delEhy+0.5*delEsh;      %strained bandgap energy
V0e = (Egb-Egwstrainedhh)*0.6;              %conduction band offset
V0e = V0e/Ry;

%Compute reciprocal space vectors G
mid = (N+1)/2;
for p=1:N
    for q=1:N
        for r=1:Nz
        G(r+((p-1)+(q-1)*N)*Nz,1) = (p-mid);
        G(r+((p-1)+(q-1)*N)*Nz,2) = (mid-q)*gamma;
        G(r+((p-1)+(q-1)*N)*Nz,3) = r;
        end
    end
end

%Load I matrix for computation of Hamiltonian
Ipath = strcat('C:\IME', num2str(apitch),  num2str(minor), num2str(major),'N9Nz9.mat');
I = load(Ipath);
I = I.I;

Ngtot = N^2*Nz;
Nalpha = 10;    %Number of k points to sample between Gamma and M along x dimension
Nbeta = ceil(Nalpha*gamma);
index = 1;
kxmax = pi;
```

```
kymax = pi*gamma;
kxstep = kxmax/(Nalpha-1);
kystep = kymax/(Nbeta-1);

H = zeros(Ngtot);
for kx = 0:kxstep:kxmax
    for ky = 0:kystep:kymax

        kx1(index) = kx;
        ky1(index) = ky;
        kn = kx/(2*pi);
        km = ky/(2*pi);

        % Compute Hamiltonian
        for p=1:Ngtot
            for q=1:Ngtot
                n = G(q,1);
                m = G(q,2);
                j = G(q,3);
                nprime = G(p,1);
                mprime = G(p,2);
                jprime = G(p,3);
                Iterm = I(p,q);
                Wb = 2*pi^2*((kn+n)*(kn+nprime)+(km+m)*(km+mprime))*(1/mbe);
                Ww = 2*pi^2*((kn+n)*(kn+nprime)+(km+m)*(km+mprime))*(1/mwe);
                if(j==jprime)
                 Zterm = L/s + (sin(pi*j*(1-L/s))-sin(pi*j*(1+L/s)))/(2*pi*j);
                 ZprimeUC = (1/2);
                 ZprimeQW = L/(2*s)+(1/(4*pi*j))*((-1)^j)*sin(pi*j*L/s);
                else
                 Zterm = (sin((j+jprime)*pi/2*(1-L/s))-sin((j+jprime)*pi/2*(1+L/s)))/(pi*(j+jprime)) ...
                     -(sin((j-jprime)*pi/2*(1-L/s))-sin((j-jprime)*pi/2*(1+L/s)))/(pi*(j-jprime));
                 ZprimeUC = 0;
                 ZprimeQW = 1/(pi*(j-jprime))*cos((j-jprime)*pi/2)*sin((j-jprime)*pi/2*L/s) ...
                     + 1/(pi*(j+jprime))*cos((j+jprime)*pi/2)*sin((j+jprime)*pi/2*L/s);
                end
                 H(p,q) = Zterm*(Wb-Ww)*Iterm + (pi*j/s)*(pi*jprime/s)*Iterm*ZprimeQW*((1/mbe)-(1/mwe)) + V0e*Zterm*Iterm;
                if(n==nprime && m==mprime)
                  H(p,q) = H(p,q) + Zterm*(Ww-Wb) + (pi*j/s)*(pi*jprime/s)*(ZprimeUC*(1/mbe) + ZprimeQW*((1/mwe)-(1/mbe))) - V0e*Zterm;
                end
                if(p==q)
                  H(p,q) = H(p,q) + Wb + V0e;
                end
            end
        end

        %Compute eigenvectors, eigenvalues of Hamiltonian and save to files
        [V,D] = eig(H);
        d = real(diag(D).*1000.*Ry);
        [D,IX] = sort(d);

        Epath = strcat('C:\E', num2str(apitch),   num2str(minor), num2str(major),'e3D', num2str(index), '.txt');
        Vpath = strcat('C:\V', num2str(apitch),   num2str(minor), num2str(major),'e3D', num2str(index), '.mat');
        IXpath = strcat('C:\IX', num2str(apitch),  num2str(minor), num2str(major),'e3D', num2str(index), '.txt');

        save (Epath, 'D', '-ASCII');
        save (Vpath, 'V', '-MAT');
        save (IXpath, 'IX', '-ASCII');

        index = index + 1;
    end
end

save ('C:\kx1.txt', 'kx1', '-ASCII');
save ('C:\ky1.txt', 'ky1', '-ASCII');
```

PlotBZhex.m

```
%PlotBZ.m
%Plots the 3D energy bandstructure in the BZ

clear all;

N=55; %Total number of points in an irreducible wedge of the BZ
%Load energy eigenvalues at each k-point
for index=1:N
    path = strcat('C:\EData\E', num2str(index), '.txt');
    E(:,index) = load(path);
end

Nbands = 3; %Number of bands to display
Nalpha = 10; %Number of points from Gamma->K in BZ

kx1 = load('C:\KData\kx1.txt');
ky1 = load('C:\KData\ky1.txt');

%Perform transformations to copy the irreducible wedge
%to cover the entire hexagonal BZ

kx2 = -0.5.*kx1+(sqrt(3)/2).*ky1;
ky2 = (sqrt(3)/2).*kx1+0.5.*ky1;

kx3 = 0.5.*kx2+(sqrt(3)/2).*ky2;
ky3 = (sqrt(3)/2).*kx2-0.5.*ky2;

kx = cat(2,kx1,kx2,kx3);
ky = cat(2,ky1,ky2,ky3);
Et = cat(2,E,E,E);

kx = cat(2,-kx,kx);
ky = cat(2,ky,ky);
Et = cat(2,Et,Et);
```

```
kx = cat(2,kx,kx);
ky = cat(2,-ky,ky);
Et = cat(2,Et,Et);

%Perform interpolation
Numpts = 201; %Number of points along x,y axes to use in interpolation
xmin = min(kx);
xmax = max(kx);
ymin = min(ky);
ymax = max(ky);

xres = (xmax-xmin)/(Numpts-1); %mesh resolution in x,y
yres = (ymax-ymin)/(Numpts-1);
xv = xmin:xres:xmax;
yv = ymin:yres:ymax;

for N=1:Nbands
    Etinterp(:,:,N) = gridfit(kx,ky,Et(N,:),xv,yv);
end

%Truncate interpolation to form a hexagon
for p=1:Numpts
    for q=1:Numpts
        m = -ymax/(xmax-(sqrt(3)/3)*ymax);
%applies for x>0, y>0 only
        x = xv(p);
        y = yv(q);
        if(x>0 && y>0)
            ylimit = m*(x-xmax);
            if y>ylimit
                for N=1:Nbands
                    Etinterp(q,p,N) = NaN;
                end
            end
        elseif(x<0 && y>0)
            m = -m;
            ylimit = m*(x-xmin);
            if y>ylimit
              for N=1:Nbands
                    Etinterp(q,p,N) = NaN;
              end
            end
        elseif(x>0 && y<0)
            m = -m;
            ylimit = m*(x-xmax);
            if y<ylimit
               for N=1:Nbands
                    Etinterp(q,p,N) = NaN;
               end
            end
        else
            ylimit = m*(x-xmin);
            if y<ylimit
               for N=1:Nbands
                    Etinterp(q,p,N) = NaN;
               end
            end
        end
    end
end
%plot
for N=1:Nbands
    surf(xv,yv,Etinterp(:,:,N));
    hold on;
End
```

PlotBZsquare.m

```
%eplotBZsquare.m
%Plots the 3D energy bandstructure in the BZ for a square lattice of
%arbitrary symmetry

clear all;

a = 100;
b = 100;
d = 60;
gamma=a/b;
Nbands = 3;  %Number of bands to plot
Nalpha = 10;
Npts = 55;   %Number of total k pts in the BZ

for index=1:Npts
    Epath = strcat('C:\E', num2str(a), num2str(a), num2str(d), 'e3D', num2str(index), '.txt');
    E(:,index) = load(Epath);
end

kxpath = strcat('C:\kx1.txt');
kypath = strcat('C:\ky1.txt');

kx = load(kxpath);
ky = load(kypath);

kx1 = cat(2,kx,ky);
ky1 = cat(2,ky,kx);
Et = cat(2,E,E);

kx2 = cat(2,kx1,-kx1);
ky2 = cat(2,ky1,ky1);
Et = cat(2,Et,Et);

kx = cat(2,kx2,kx2);
ky = cat(2,ky2,-ky2);
```

```
Et = cat(2,Et,Et);

Numpts = 401;
xmin = min(kx);
xmax = max(kx);
ymin = min(ky);
ymax = max(ky);

xres = (xmax-xmin)/(Numpts-1);
yres = (ymax-ymin)/(Numpts-1);
xv = xmin:xres:xmax;
yv = ymin:yres:ymax;

for N=1:Nbands
    Etinterp(:,:,N) = gridfit(kx,ky,Et(N,:),xv,yv);
end

for N=1:Nbands
    surf(xv,yv,Etinterp(:,:,N), 'LineStyle', 'none');
    hold on;
End
```

DOShex.m

```
%eDOS.m
%Computes density of states for electons

clear all;

%define global vars
global a;
global q;
global L;
global T;
global hbar;
global h;
global me;
global pi;
global e;
global eEstep;
global edeltaE;
global epath;

%constants
hbar = 1.054*10^-34;
h = 6.626*10^-34;
me = 9.11*10^-31;
pi = 3.14159;
e = 1.6*10^-19;

%Set vars
T = 77; %temp
q = 0.25; %Indium composition in QW
L = 10e-9; %QW thickness
a = 80e-9; %NP pitch
eEstep = 0.001; %step size in energy
edeltaE = 0.004; %size of each energy bin
Nbands = 3; %number of energy bands

N = 55; %Number of points in irreducible wedge of BZ
%load eigenvalues at each k-point
for p = 1:N
   epath = strcat('C:\E data\E', num2str(p), '.txt');
   Ee(:,p) = load(epath);
end
kx = load('C:\KData\kx1.txt');
ky = load('C:\KData\ky1.txt');

%Perform interpolation of energy bands
Numpts = 401; %Number of points along x,y to use in interpolation
xmin = min(kx);
xmax = max(kx);
ymin = min(ky);
ymax = max(ky);

xres = (xmax-xmin)/(Numpts-1);
yres = (ymax-ymin)/(Numpts-1);
Ak = xres*yres; %Area of each k-point in mesh
xv = xmin:xres:xmax;
yv = ymin:yres:ymax;

for N=1:Nbands
    Einterp(:,:,N) = gridfit(kx,ky,Ee(N,:),xv,yv);
end
Emin = min(min(Einterp(:,:,1)));
Emax = max(max(Einterp(:,:,Nbands)));

%Divide energy space into finite number of bins
Nbins = ceil((Emax-Emin)/eEstep)+1;
Emax = Emin+(Nbins-1)*eEstep;

bins = zeros(1,Nbins);

%Loop over k-points in mesh and add to each bin
i = 1;
numk = 0;
for p=1:Numpts
    for q=1:Numpts
        x = xv(p);
        y = yv(q);
        ycutoff = ymin+sqrt(3)*(x-xmin);
        if (y>ycutoff && x~=0)

            for N=1:Nbands
```

```
586                 lbound = (Einterp(q,p,N)-edeltaE/2);
587                 ubound = (Einterp(q,p,N)+edeltaE/2);
588                 lboundN = ceil((lbound-Emin)/eEstep)+1;
589                 uboundN = floor((ubound-Emin)/eEstep)+1;
590                 for Nb = lboundN:1:uboundN
591                         bins(Nb) = bins(Nb)+1;
592                 end
593                end


594           elseif ((y>ycutoff && x==0) || (y==ycutoff && x>0))
595
596             for N=1:Nbands
597                 lbound = (Einterp(q,p,N)-edeltaE/2);
598                 ubound = (Einterp(q,p,N)+edeltaE/2);
599                 lboundN = ceil((lbound-Emin)/eEstep)+1;
600                  uboundN = floor((ubound-Emin)/eEstep)+1;
601                  for Nb = lboundN:1:uboundN
602                         bins(Nb) = bins(Nb)+0.5;
603                   end
604               end
605
606               elseif (y==0 && x==0)
607                   for N=1:Nbands
608                     lbound = (Einterp(q,p,N)-edeltaE/2);
609                     ubound = (Einterp(q,p,N)+edeltaE/2);
610                     lboundN = ceil((lbound-Emin)/eEstep)+1;
611                     uboundN = floor((ubound-Emin)/eEstep)+1;
612                     for Nb = lboundN:1:uboundN
613                           bins(Nb) = bins(Nb)+(1/12);
614                     end
615                 end
616
617
618             end
619
620           end
621     end
622
623   %compute DOS based on number of k-points in each bin
624   erho = 12*2*bins*Ak/(4*pi^2*(L*100)*(edeltaE/1000)*(a*100)^2); %Multiply by 12 to account for the symmetry of the
      BZ and by 2 for spin degeneracy.
625
626   Evector = Emin:eEstep:Emax;
627
628   erho = erho';
629   Evector = Evector';
630   %save data to files
631   path = strcat('C:\DOS\eDOS.txt');
632   save (path, 'erho', '-ASCII');
633   path = strcat('C:\DOS\Evector.txt');
634   save (path, 'Evector', '-ASCII');
635
636   %plot
637   plot(Evector, erho)
```

DOSsquare.m

```
638   %DOSsquare.m
639   %Calculates the density of states given the interpolated energy
640   %bands. Takes the interpolated bands generated in genInterp.m as input.
641
642   clear all;
643
644   %Set vars
645   apitch = 100;   %pitch in x dimension
646   bpitch = 100;   %pitch in y dimension
647   a = apitch;
648   d = 60;             %pore diameter
649   L=8e-9;             %QW thickness
650   eEstep = 0.001;
651   edeltaE = 0.002;
652   NbandStart = 1;
653   NbandStop = 10;
654   Nbands = NbandStop-NbandStart+1; %Number of bands to use in the calculation
655   gamma =0;
656
657   kxpath = strcat('C:\kx1.txt');
658   kypath = strcat('C:\ky1.txt');
659
660   kx = load(kxpath);
661   ky = load(kypath);
662
663   Numpts = 201;
664   xmin = min(kx);
665   xmax = max(kx);
666   ymin = min(ky);
667   ymax = max(ky);
668
669   xres = (xmax-xmin)/(Numpts-1);
670   yres = (ymax-ymin)/(Numpts-1);
671   Ak = xres*yres;
672   xv = xmin:xres:xmax;
673   yv = ymin:yres:ymax;
674
675   for N=NbandStart:NbandStop
676       Einterppath = strcat('C:\E', num2str(apitch), num2str(bpitch),'e3DInterp', num2str(N), '.mat');
677       E = load(Einterppath);
678       Einterp(:,:,N-NbandStart+1) = E.Einterp;
679   end
680
681   Emin = min(min(Einterp(:,:,1))) - edeltaE/2;
682   Emax = max(max(Einterp(:,:,Nbands))) + edeltaE/2;
683
```

```
Nbins = ceil((Emax-Emin)/eEstep)+1;
Emax = Emin+(Nbins-1)*eEstep;

bins = zeros(1,Nbins);

i = 1;
numk = 0;
    for p=1:Numpts
        for q=1:Numpts
            x = xv(p);
            y = yv(q);
            ycutoff = ymin+(x-xmin);
            if (y~=0 && x~=0)

                for N=1:Nbands
                    lbound = (Einterp(q,p,N)-edeltaE/2);
                    ubound = (Einterp(q,p,N)+edeltaE/2);
                    lboundN = ceil((lbound-Emin)/eEstep)+1;
                    uboundN = ceil((ubound-Emin)/eEstep)+1;
                    for Nb = lboundN:1:uboundN
                        bins(Nb) = bins(Nb)+1;
                    end
                end

            elseif ((y>0 && x==0) || (y==0 && x>0))

                for N=1:Nbands
                    lbound = (Einterp(q,p,N)-edeltaE/2);
                    ubound = (Einterp(q,p,N)+edeltaE/2);
                    lboundN = ceil((lbound-Emin)/eEstep)+1;
                    uboundN = ceil((ubound-Emin)/eEstep)+1;
                    for Nb = lboundN:1:uboundN
                        bins(Nb) = bins(Nb)+0.5;
                    end
                end

            elseif (y==0 && x==0)
                for N=1:Nbands
                    lbound = (Einterp(q,p,N)-edeltaE/2);
                    ubound = (Einterp(q,p,N)+edeltaE/2);
                    lboundN = ceil((lbound-Emin)/eEstep)+1;
                    uboundN = ceil((ubound-Emin)/eEstep)+1;
                    for Nb = lboundN:1:uboundN
                        bins(Nb) = bins(Nb)+(1/4);
                    end
                end


            end

         end
    end


erho = 4*2*bins*Ak/(4*pi^2*(L*100)*(edeltaE/1000)*(a*1e-9*100)^2); %Multiply by 4 to account for the symmetry of the BZ and by 2 for spin degeneracy.

Evector = Emin:eEstep:Emax;
NumE = size(Evector,2);

if gamma>0
  NumE = size(Evector,2);
    Spectrum = zeros(1,NumE);
    for i = 1:NumE
      E = Evector(i);
      Lorentz = ((gamma/(2*pi))./((Evector-E).^2+(gamma/2)^2)); %Lorentzian broadening term
      mat1 = eEstep.*erho;
      dot2 = dot(mat1, Lorentz);
      Spectrum(i) = dot2;
    end
end

path =  strcat('C:\eDOS.txt');
save (path, 'erho', '-ASCII');
path =  strcat('C:\eEvector.txt');
save (path, 'Evector', '-ASCII');

plot(Evector, erho);
```

jDOShex.m

```
%jDOS.m
%Computes joint DOS

clear all;

%global vars
global a;
global q;
global L;
global T;
global Egwstrainedhh;
global hbar;
global h;
global me;
global pi;
global e;
global e0;
global kb;
global epath;
global hpath;

%constants
hbar = 1.054*10^-34;
h = 6.626*10^-34;
me = 9.11*10^-31;
```

```
26    pi = 3.14159;
27    e = 1.6*10^-19;
28    e0 = 8.8542*10^-12;
29    kb = 1.38*10^-23;
30    InAsac = -5.08;
31    InAsav = 1.00;
32    InAsb = -1.8;
33    InAsd = -3.6;
34    InAsC11 = 8.329;
35    InAsC12 = 4.526;
36    InAsa0 = 6.0584;
37    GaAsac = -7.17;
38    GaAsav = 1.16;
39    GaAsb = -1.7;
40    GaAsd = -4.55;
41    GaAsC11 = 11.879;
42    GaAsC12 = 5.376;
43    GaAsa0 = 5.6533;


44    %Set vars
45    T = 77; %temp
46    q = 0.25; %Indium composition in QW
47    L = 8e-9; %QW thickness
48    a = 80e-9; %NP pitch
49    lambdastart = 950;
50    lambdastop = 970;
51    %jEsteplow and jdeltaElow will be used for the first two subbands
52    jEsteplow = 0.0025;
53    jdeltaElow = 0.005;
54    %jEstephigh and jdeltaEhigh will be used for the third subband
55    %Since the third subband is relatively flat we must use a smaller
56    %step size and bin width to accurately compute the joint DOS.
57    jEstephigh = 0.00025;
58    jdeltaEhigh = 0.0005;
59
60    %Compute strained bandgap energy
61    mwe = (0.023+0.037*(1-q)+0.003*(1-q)^2)*me;
62    mbe = 0.063*me;
63    mwhh = (0.41+0.1*(1-q))*me;
64    mbhh = 0.51*me;
65    Egw = 0.42+0.625*(1-q)-(5.8/(T+300)-4.19/(T+273))*0.0001*T*T*(1-q)-0.000419*T*T/(T+271)+0.475*(1-q)*(1-q);
66    Egb = 1.519-5.405e-4*T^2/(T+204);
67    a0 = q*InAsa0+(1-q)*GaAsa0;
68    av = q*InAsav+(1-q)*GaAsav;
69    ac = q*InAsac+(1-q)*GaAsac;
70    b = q*InAsb+(1-q)*GaAsb;
71    d = q*InAsd+(1-q)*GaAsd;
72    C11 = q*InAsC11 + (1-q)*GaAsC11;
73    C12 = q*InAsC12 + (1-q)*GaAsC12;
74    e0 = (GaAsa0-a0)/GaAsa0;
75    Ep = q*22.2+(1-q)*25.7;
76    exxresult = e0;
77    eyyresult = e0;
78    ezzresult = -2*C12/C11*e0;
79    cbresultw = ac*(exxresult+eyyresult+ezzresult);
80    P = -av*(exxresult+eyyresult+ezzresult);
81    Q = -b/2*(exxresult+eyyresult-2*ezzresult);
82    Rsquared = 0.75*b*b*(exxresult-eyyresult)*(exxresult-eyyresult);
83    if(Q<0)
84        sgnQ=-1;
85    else
86        sgnQ=1;
87    end
88    hhresultw = -P-sgnQ*sqrt(Q*Q+Rsquared);
89    lhresultw = -P+sgnQ*sqrt(Q*Q+Rsquared);
90    Egwstrainedhh = Egw+(cbresultw-hhresultw);
91    Egwstrainedlh = Egw+(cbresultw-lhresultw);
92    Egbstrained = Egb;
93    Egwnew = Egwstrainedhh*1000;
94
95    %load energy eigenvalues for electrons and holes
96    for p = 1:55
97       epath = strcat('C:\EData\E', num2str(p), '.txt');
98       hpath = strcat('C:\EData\HH', num2str(p), '.txt');
99       Ee(:,p) = load(epath);
100      Eh(:,p) = load(hpath);
101   end
102   kx = load('N:\KData\kx1.txt');
103   ky = load('N:\KData\ky1.txt');
104
105   %Perform interpolation
106   Numpts = 401;
107   xmin = min(kx);
108   xmax = max(kx);
109   ymin = min(ky);
110   ymax = max(ky);
111
112   xres = (xmax-xmin)/(Numpts-1);
113   yres = (ymax-ymin)/(Numpts-1);
114   Ak = xres*yres;
115   xv = xmin:xres:xmax;
116   yv = ymin:yres:ymax;
117
118   Ee1 = Ee(1,:);
119   Ee2 = Ee(2,:);
120   Ee3 = Ee(3,:);
121
122   Eh1 = Eh(1,:);
123   Eh2 = Eh(2,:);
124   Eh3 = Eh(3,:);
125
126   Ee1interp = gridfit(kx,ky,Ee1,xv,yv);
127   Ee2interp = gridfit(kx,ky,Ee2,xv,yv);
128   Ee3interp = gridfit(kx,ky,Ee3,xv,yv);
129
130   Eh1interp = gridfit(kx,ky,Eh1,xv,yv);
```

```
Eh2interp = gridfit(kx,ky,Eh2,xv,yv);
Eh3interp = gridfit(kx,ky,Eh3,xv,yv);

E1interp = Ee1interp+Eh1interp+Egwnew;
E2interp = Ee2interp+Eh2interp+Egwnew;
E3interp = Ee3interp+Eh3interp+Egwnew;

E1min = min(min(E1interp));
E3min = min(min(E3interp));
E3max = max(max(E3interp));

%Initialize array of energy bins
Nbinslow = floor((E3min-E1min)/jEsteplow);
E3min = E1min+Nbinslow*jEsteplow;
Nbinshigh = ceil((E3max-E3min)/jEstephigh);
E3max = E3min+(Nbinshigh-1)*jEstephigh;

Nbinstotal = Nbinslow+Nbinshigh;

bins = zeros(1,Nbinstotal);
%Eavg arrays store the average energy of electrons/holes within each energy bin
eEavg = zeros(1,Nbinstotal);
hEavg = zeros(1,Nbinstotal);

%Loop over k-points and add to energy bins
i = 1;
numk = 0;
    for p=1:1:Numpts
        for q=1:1:Numpts
            x = xv(p);
            y = yv(q);
            ycutoff = ymin+sqrt(3)*(x-xmin);
            if (y>=ycutoff && x~=0)

                lbound = (E1interp(q,p)-jdeltaElow/2);
                ubound = (E1interp(q,p)+jdeltaElow/2);
                lboundN = ceil((lbound-E1min)/jEsteplow)+1;
                uboundN = floor((ubound-E1min)/jEsteplow)+1;
                for N = lboundN:1:uboundN
                    bins(N) = bins(N)+1;
                    eEavg(N) = eEavg(N)+Ee1interp(q,p);
                    hEavg(N) = hEavg(N)+Eh1interp(q,p);
                end

                lbound = (E2interp(q,p)-jdeltaElow/2);
                ubound = (E2interp(q,p)+jdeltaElow/2);
                lboundN = ceil((lbound-E1min)/jEsteplow)+1;
                uboundN = floor((ubound-E1min)/jEsteplow)+1;
                for N = lboundN:1:uboundN
                    bins(N) = bins(N)+1;
                    eEavg(N) = eEavg(N)+Ee1interp(q,p);
                    hEavg(N) = hEavg(N)+Eh1interp(q,p);
                end

                lbound = (E3interp(q,p)-jdeltaEhigh/2);
                ubound = (E3interp(q,p)+jdeltaEhigh/2);
                lboundN = Nbinslow+ceil((lbound-E3min)/jEstephigh)+1;
                uboundN = Nbinslow+floor((ubound-E3min)/jEstephigh)+1;
                for N = lboundN:1:uboundN
                    bins(N) = bins(N)+1;
                    eEavg(N) = eEavg(N)+Ee1interp(q,p);
                    hEavg(N) = hEavg(N)+Eh1interp(q,p);
                end
            elseif (y>=ycutoff && x==0)

                lbound = (E1interp(q,p)-jdeltaElow/2);
                ubound = (E1interp(q,p)+jdeltaElow/2);
                lboundN = ceil((lbound-E1min)/jEsteplow)+1;
                uboundN = floor((ubound-E1min)/jEsteplow)+1;
                for N = lboundN:1:uboundN
                    bins(N) = bins(N)+0.5;
                    eEavg(N) = eEavg(N)+0.5*Ee1interp(q,p);
                    hEavg(N) = hEavg(N)+0.5*Eh1interp(q,p);
                end

                lbound = (E2interp(q,p)-jdeltaElow/2);
                ubound = (E2interp(q,p)+jdeltaElow/2);
                lboundN = ceil((lbound-E1min)/jEsteplow)+1;
                uboundN = floor((ubound-E1min)/jEsteplow)+1;
                for N = lboundN:1:uboundN
                    bins(N) = bins(N)+0.5;
                    eEavg(N) = eEavg(N)+0.5*Ee1interp(q,p);
                    hEavg(N) = hEavg(N)+0.5*Eh1interp(q,p);
                end


                lbound = (E3interp(q,p)-jdeltaEhigh/2);
                ubound = (E3interp(q,p)+jdeltaEhigh/2);
                lboundN = Nbinslow+ceil((lbound-E3min)/jEstephigh)+1;
                uboundN = Nbinslow+floor((ubound-E3min)/jEstephigh)+1;
                for N = lboundN:1:uboundN
                    bins(N) = bins(N)+0.5;
                    eEavg(N) = eEavg(N)+0.5*Ee1interp(q,p);
                    hEavg(N) = hEavg(N)+0.5*Eh1interp(q,p);
                end

            end

        end
    end

binslow = bins(1:Nbinslow);
binshigh = bins(Nbinslow+1:Nbinslow+Nbinshigh);
jrholow = 12*2*binslow*Ak/(4*pi^2*(L*100)*(jdeltaElow/1000)*(a*100)^2); %Multiply by 12 to account for the symmetry of the BZ and by 2 for spin degeneracy.
jrhohigh = 12*2*binshigh*Ak/(4*pi^2*(L*100)*(jdeltaEhigh/1000)*(a*100)^2);
jrho = cat(2,jrholow,jrhohigh);
```

```
235
236   jEvectorlow = E1min:jEsteplow:E1min+(Nbinslow-1)*jEsteplow;
237   jEvectorhigh = E3min:jEstephigh:E3max;
238   jEvector = cat(2,jEvectorlow,jEvectorhigh);
239
240   jEmin = jEvector(1);
241   jEmax = jEvector(Nbinstotal);
242   Elow = 1242000/lambdastop;
243   Ehigh = 1242000/lambdastart;
244
245   Nlow = ceil((jEmin-Elow)/jEsteplow)+1;
246   Nhigh = ceil((Ehigh-jEmax)/jEsteplow)+1;
247
248   %pad energy vectors with zeros
249   jElow = jEmin-(Nlow)*jEsteplow:jEsteplow:jEmin-jEsteplow;
250   jEhigh = jEmax+jEsteplow:jEsteplow:jEmax+(Nhigh)*jEsteplow;
251   ZerosLow = zeros(1,Nlow);
252   ZerosHigh = zeros(1,Nhigh);
253
254   %Compute average electron and hole energies in each bin
255   for N=1:Nbinstotal
256       if bins(N)==0
257           eEavg(N)=0;
258           hEavg(N)=0;
259       else
260           eEavg(N) = eEavg(N)/bins(N);
261           hEavg(N) = hEavg(N)/bins(N);
262       end
263   end
264
265   jEvector = cat(2,jElow,jEvector,jEhigh);
266   jrho = cat(2,ZerosLow,jrho,ZerosHigh);
267   eEavg = cat(2,ZerosLow,eEavg,ZerosHigh);
268   hEavg = cat(2,ZerosLow,hEavg,ZerosHigh);
269
270   %compute step size arrays
271   StepSizelow = jEsteplow.*ones(1,Nbinslow+Nlow);
272   StepSizemid = jEstephigh.*ones(1,Nbinshigh);
273   StepSizehigh = jEsteplow.*ones(1,Nhigh);
274   StepSize = cat(2, StepSizelow, StepSizemid, StepSizehigh);
275
276   eEavg = eEavg';
277   hEavg = hEavg';
278   jEvector = jEvector';
279   jrho = jrho';
280   StepSize = StepSize';
281
282   %save to files
283   save 'C:\DOS\eEavg.txt' eEavg
284   save 'C:\DOS\hEavg.txt' hEavg
285   save 'C:\DOS\Ejtest.txt' jEvector
286   save 'C:\DOS\jrhotest.txt' jrho
287   save 'C:\DOS\StepSize.txt' StepSize
288
289   %plot
290   plot(jEvector, jrho);
```

jDOSsquare.m

```
291   %jDOSsquare.m
292   %Calculates the joint density of states for a square lattice with
293   %arbitrary symmetry. Takes the interpolated electron and heavy hole
294   %bands as inputs along with the interpolated dipole matrix elements
295   %for each possible transition.
296
297   clear all;
298
299   %Constants
300   T = 77;
301   c = 0.25;
302   a = 100;
303   bd = 100;
304   L=8e-9;
305   diam = 60;
306   eEstep = 0.01;
307   edeltaE = 0.02;
308   gamma = 0; %Lorentzian broadening FWHM (meV)
309   Nemin = 1;
310   Nemax = 10;
311   Nhmin = 1;
312   Nhmax = 10;
313   Nhbands = (Nhmax-Nhmin)+1;
314   lambdastart = 800;
315   lambdastop = 1000;
316   pol = 1;    %polarization 1=x(TE), 2=y (TE), 3=z (TM)
317
318   N = 9;
319   Nz = 9;
320
321   %Constants
322   hbar = 1.054*10^-34;
323   e = 1.6*10^-19;
324   me = 9.11*10^-31;
325   InAsac = -5.08;
326   InAsav = 1.00;
327   InAsb = -1.8;
328   InAsd = -3.6;
329   InAsC11 = 8.329;
330   InAsC12 = 4.526;
331   InAsa0 = 6.0584;
332   GaAsac = -7.17;
333   GaAsav = 1.16;
334   GaAsb = -1.7;
335   GaAsd = -4.55;
336   GaAsC11 = 11.879;
```

```
337   GaAsC12 = 5.376;
338   GaAsa0 = 5.6533;
339
340   %Calculate strained bandgaps
341   a0 = c*InAsa0+(1-c)*GaAsa0;                 %//interpolate InGaAs lattice constant
342   av = c*InAsav+(1-c)*GaAsav;                 %//interpolate InGaAs valence band deformation potential
343   ac = c*InAsac+(1-c)*GaAsac;                 %//interpolate InGaAs conduction band deformation potential
344   b = c*InAsb+(1-c)*GaAsb;                    %//interpolate InGaAs shear deformation potential
345   d = c*InAsd+(1-c)*GaAsd;                    %//interpolate InGaAs shear deformation potential
346   C11 = c*InAsC11 + (1-c)*GaAsC11;            %//interpolate InGaAs elastic constant C11
347   C12 = c*InAsC12 + (1-c)*GaAsC12;            %//interpolate InGaAs elastic constant C12
348   e0 = (GaAsa0-a0)/GaAsa0;                    %//compute misfit strain
349   exxresult = e0;
350   eyyresult = e0;
351   ezzresult = -2*C12/C11*e0;
352   cbresultw = ac*(exxresult+eyyresult+ezzresult);
353   P = -av*(exxresult+eyyresult+ezzresult);
354   Q = -b/2*(exxresult+eyyresult-2*ezzresult);
355   Rsquared = 0.75*b*b*(exxresult-eyyresult)*(exxresult-eyyresult);
356   if(Q<0)
357       sgnQ=-1;
358   else
359       sgnQ=1;
360   end
361   hhresultw = -P-sgnQ*sqrt(Q*Q+Rsquared);
362   Egw = 0.42+0.625*(1-c)-(5.8/(T+300)-4.19/(T+273))*0.0001*T*T*(1-c)-0.000419*T*T/(T+271)+0.475*(1-c)*(1-c);
363   delEhy = -2*(ac-av)*(C11-C12)/C11*e0;
364   cbshift = 2*ac*((C11-C12)/C11)*e0;
365   Egwstrained = (Egw+cbshift-hhresultw)*1000;
366
367   kxpath = strcat('C:\kx1.txt');
368   kypath = strcat('C:\ky1.txt');
369
370   kx = load(kxpath);
371   ky = load(kypath);
372
373   Numpts = 51;
374   xmin = min(kx);
375   xmax = max(kx);
376   ymin = min(ky);
377   ymax = max(ky);
378
379   xres = (xmax-xmin)/(Numpts-1);
380   yres = (ymax-ymin)/(Numpts-1);
381   Ak = xres*yres;
382   xv = xmin:xres:xmax;
383   yv = ymin:yres:ymax;
384
385   Emin = 1242000/lambdastop;
386   Emax = 1242000/lambdastart;
387
388   Nbins = ceil((Emax-Emin)/eEstep)+1;
389   Emax = Emin+(Nbins-1)*eEstep;
390
391   bins = zeros(1,Nbins);
392
393   for enum = Nemin:Nemax
394
395   Eeinterppath = strcat('C:\E', num2str(a), num2str(bd), num2str(diam), 'e3D', num2str(enum), 'Interp.mat');
396   Ee = load(Eeinterppath);
397   Einterp = zeros(Numpts,Numpts,Nhbands);
398   MMEinterpArray = zeros(Numpts,Numpts,Nhbands);
399
400   for j=Nhmin:Nhmax
401
402       Ehinterppath = strcat('C:\E', num2str(a), num2str(bd), num2str(diam), 'h3D', num2str(j), 'Interp.mat');
403       Eh = load(Ehinterppath);
404       Einterp(:,:,j) = (Ee.Einterp + Eh.Einterp + Egwstrained);
405
406       savepath = strcat('C:\MMEinterpP', num2str(pol), 'C', num2str(enum), 'H', num2str(j), '.mat');
407       MMEinterp = load(savepath);
408       MMEinterpArray(:,:,j) = MMEinterp.MMEinterp;
409
410   end
411
412       for p=1:Numpts
413           for q=1:Numpts
414               x = xv(p);
415               y = yv(q);
416               if (y~=0 && x~=0)
417
418                   for j=Nhmin:Nhmax
419                       lbound = (Einterp(q,p,j)-edeltaE/2);
420                       ubound = (Einterp(q,p,j)+edeltaE/2);
421                       lboundN = ceil((lbound-Emin)/eEstep)+1;
422                       uboundN = ceil((ubound-Emin)/eEstep)+1;
423                       for Nb = lboundN:1:uboundN
424                           bins(1,Nb) = bins(1,Nb)+MMEinterpArray(q,p,j);
425                       end
426                   end
427
428               elseif ((y>0 && x==0) || (y==0 && x>0))
429
430                   for j=Nhmin:Nhmax
431                       lbound = (Einterp(q,p,j)-edeltaE/2);
432                       ubound = (Einterp(q,p,j)+edeltaE/2);
433                       lboundN = ceil((lbound-Emin)/eEstep)+1;
434                       uboundN = ceil((ubound-Emin)/eEstep)+1;
435                       for Nb = lboundN:1:uboundN
436                           bins(1,Nb) = bins(1,Nb)+0.5*MMEinterpArray(q,p,j);
437                       end
438                   end
439
440               elseif (y==0 && x==0)
441
442                   for j=Nhmin:Nhmax
443                       lbound = (Einterp(q,p,j)-edeltaE/2);
444                       ubound = (Einterp(q,p,j)+edeltaE/2);
```

```
                        lboundN = ceil((lbound-Emin)/eEstep)+1;
                        uboundN = ceil((ubound-Emin)/eEstep)+1;
                        for Nb = lboundN:1:uboundN
                            bins(1,Nb) = bins(1,Nb)+(1/4)*MMEinterpArray(q,p,j);
                        end
                    end


                end

            end
        end
    end

    jrho = 4.*2.*bins.*Ak./(4.*pi.^2.*(L.*100).*(edeltaE./1000).*(a.*1e-9.*100).^2); %Multiply by 4 to account for
    the symmetry of the BZ and by 2 for spin degeneracy.


    jEvector = Emin:eEstep:Emax;
    jEvector = jEvector' - 0.0*1.6;
    lambdavector = 1242000./jEvector;

    if gamma==0
        jDOSpath = strcat('C:\jDOS', num2str(pol), '.txt');
        jEvectorpath = strcat('C:\jEvector', num2str(pol), '.txt');
        lambdavectorpath = strcat('C:\jlambdavector', num2str(pol), '.txt');

        jrho = jrho';
        jEvector = jEvector';
        lambdavector = lambdavector';
        save (jDOSpath, 'jrho', '-ASCII');
        save (jEvectorpath, 'jEvector', '-ASCII');
        save (lambdavectorpath, 'lambdavector', '-ASCII');
        plot(lambdavector, jrho);
    else
        NumE = size(jEvector,2);
        Spectrum = zeros(1,NumE);
        for i = 1:NumE
          E = jEvector(i);
          Lorentz = ((gamma/(2*pi))./((jEvector-E).^2+(gamma/2)^2)); %Lorentzian broadening term
          mat1 = eEstep.*jrho;
          dot2 = dot(mat1, Lorentz);
          Spectrum(i) = dot2;
        end

        jDOSpath = strcat('C:\jDOSb.txt');
        jEvectorpath = strcat('C:\jEvectorb.txt');
        lambdavectorpath = strcat('C:\lambdavectorb.txt');

        Spectrum = Spectrum';
        jEvector = jEvector';
        lambdavector = lambdavector';
        save (jDOSpath, 'Spectrum', '-ASCII');
        save (jEvectorpath, 'jEvector', '-ASCII');
        save (lambdavectorpath, 'lambdavector', '-ASCII');
        plot(lambdavector, Spectrum);
    end
```

GainCalc.m

```
%gaincalc.m
%Computes gain spectrum
%Takes input files computed in jDOS.m

clear all;

%Declare global variables
global a;
global q;
global L;
global T;
global Fc;
global Fv;
global hbar;
global h;
global me;
global pi;
global e;
global e0;
global kb;

%Set constants
hbar = 4.135*10^-15;
h = 6.626*10^-34;
me = 9.11*10^-31;
pi = 3.14159;
e = 1.6*10^-19;
e0 = 8.8542*10^-12;
kb = 1.38*10^-23;
nr = 3.3;
c = 3e8;
Ep = 25.7;
C0 = 1e4*pi*hbar*e^2/(nr*c*e0*me^2);
MME = (3/2)*(me/6)*Ep;

%Set vars
T = 77; %temp
q = 0.25; %In composition
L = 8e-9; %QW thickness
a = 80e-9; %NP pitch
Ntarget = 1e18; %target carrier density
gamma = 1; %broadening in meV

eEvector = load('C:\DOS\Eevector.txt');
hhEvector = load('C:\DOS\Ehvector.txt');
eRho = load('C:\DOS\erho.txt');
```

```
hhRho = load('C:\DOS\hrho.txt');
load('C:\DOS\jrho.txt');
load('C:\DOS\StepSize.txt');
load('C:\DOS\eEavg.txt');
load('C:\DOS\hEavg.txt');

%compute carrier concentration based on Fc
Fc = calcFc(eRho, Ntarget, eEvector);

%compute Fv (quasi Fermi level for holes)
Fv = calcFv(hhRho, Ntarget, hhEvector);

i = 1;
NumE = size(jEvector,1);

%Compute gain spectrum
for i = 1:NumE
  result = 0;
  E = jEvector(i);
  f = ((1./(1+exp((eEavg-Fc)./(1000*kb*T/e))))-(1./(1+exp((-hEavg-Fv)./(1000*kb*T/e))))); %difference in quasi fermi levels
  Lorentz = ((gamma/(2*pi))./((jEvector-E).^2+(gamma/2)^2)); %Lorentzian broadening term
  mat1 = StepSize.*jrho.*f;
  dot2 = dot(mat1, Lorentz);
  Spectrum(i) = C0*MME*(1000/E)*dot2;
  i = i+1;
end
imax = i-1;

lambdavector = 1242000./jEvector;
Spectrum = fliplr(Spectrum);
lambdavector = flipud(lambdavector);

%plot
plot(lambdavector,Spectrum);
```

ComputeMME.m

```
%ComputeMME.m
%Calculates the dipole matrix elements for vertical transitions for all
%possible combinations of conduction and valence bands

clear all;

N = 9;
Nz = 9;
Ngtot = N^2*Nz;
TotalH = 10;
NumE = 10;
Nkpts = 1;

a = 100;
b = 100;
diam = 60;
gamma = a/b;
L = 8; %QW thickness
T = 77; %Temp
q = 0.25; %Indium composition
s = 3*L;
L = L/a;
s = s/a;

kxpath = strcat('C:\kx1.txt');
kypath = strcat('C:\ky1.txt');

kx1 = load(kxpath);
ky1 = load(kypath);

%Compute reciprocal space vectors G
mid = (N+1)/2;
for p=1:N
    for q=1:N
        for r=1:Nz
        G(r+((p-1)+(q-1)*N)*Nz,1) = (p-mid);
        G(r+((p-1)+(q-1)*N)*Nz,2) = gamma*(mid-q);
        G(r+((p-1)+(q-1)*N)*Nz,3) = r;
        end
    end
end

%Compute MME at each k point

for kindex = 1:Nkpts
kindex
eEpath = strcat('C:\E10060e3D', num2str(kindex), '.txt');
eIXpath = strcat('C:\IX10060e3D', num2str(kindex), '.txt');
eVpath = strcat('C:\V10060e3D', num2str(kindex), '.txt');
hEpath = strcat('C:\E10060h3D', num2str(kindex), '.txt');
hIXpath = strcat('C:\IX10060h3D', num2str(kindex), '.txt');
hVpath = strcat('C:\V10060h3D', num2str(kindex), '.txt');

eEvector = load(eEpath);
eIX = load(eIXpath);
eV = load(eVpath);
eV = eV.V;

hEvector = load(hEpath);
hIX = load(hIXpath);
hV = load(hVpath);
hV = hV.V;

for enum=1:NumE

eE = eEvector(enum);
eRef = eIX(enum,1);
```

```
eVector = eV(:,eRef);

kx = kx1(kindex);
ky = ky1(kindex);


MMEPath =  strcat('C:\', 'MME10060_', num2str(enum), '_', num2str(kindex),'.mat');

MMESup = zeros(TotalH,1);
MMESdown = zeros(TotalH,1);
MMEStot = zeros(TotalH,1);
eVector = eVector';
for hnum = 1:TotalH

    hE = hEvector(hnum);
    hRef = hIX(hnum,1);
    hVector = hV(:,hRef);

    hVector1 = hVector(1:Ngtot);
    eh1 = eVector*hVector1;

    MMESup(hnum,1) = eh1;
    MMEStot(hnum,1) = (abs(MMESup(hnum,1)).^2);

end
save (MMEPath, 'MMEStot', '-MAT');

end

End
```

CalcFc.m

```
%calcFc.m
%computes position of conduction band quasi-Fermi level based on target carrier density

function Fc = calcFc(rho, Ntarget, Evector)
%declare global variables
global T;
global Fc;
global e;
global kb;
global eEstep;

%compute Fc
Fc = 0;
Fmax=10;
Fmin=-10;
error=1;
imax = size(Evector,1);
eEstep = Evector(2)-Evector(1);
while(error>0.0001)
    Fc = (Fmin+Fmax)/2;
    N = 0;
    for i = 1:imax
        N = N + (eEstep/1000)*rho(i)*1/(1+exp(((Evector(i))/1000-Fc)/(kb*T/e)));
    end
    error = abs((N-Ntarget)/Ntarget);
    if(N<Ntarget)
        Fmin = Fc;
    else
        Fmax = Fc;
    end
end

Fc = Fc*1000;
end
```

CalcFv.m

```
%calcFv.m
%Computes position of valence band quasi-Fermi level based on target
%carrier density
function Fv = calcFv(rho, Ntarget, Evector)

%declare global variables
global q;
global T;
global Fv;
global e;
global kb;
global hhEstep;

%compute Fv
Fv = 0;
Fmax=10;
Fmin=-10;
error=1;
q = 1;
imax = size(Evector,1);
hhEstep = Evector(2)-Evector(1);
while(error>0.0001)
    Fv = (Fmin+Fmax)/2;
    N = 0;
    for i = 1:imax
        N = N + (hhEstep/1000)*rho(i)*(1-(1/(1+exp(((-Evector(i))/1000-Fv)/(kb*T/e)))));
    end
    error = abs((N-Ntarget)/Ntarget);
    if(N<Ntarget)
        Fmax = Fv;
    else
        Fmin = Fv;
```

```
33          end
34
35      end
36      Fv = Fv*1000;
37
38      End
```

Egeninterpsquare.m

```
39      %Egeninterpsquare
40      %Interpolate energy bands for a square lattice geometry
41      %Takes eigenvalues computed in Nporesquare3De.m as input
42
43      clear all;
44
45      apitch = 100;
46      bpitch = 100;
47      diam = 60;
48      BandStart = 1;
49      BandStop = 10;
50      Nkpts = 55;
51
52      N = 9;
53      Nz = 9;
54
55      kxpath = strcat('C:\kx1.txt');
56      kypath = strcat('C:\ky1.txt');
57
58      kx = load(kxpath);
59      ky = load(kypath);
60
61      for index=1:Nkpts
62          epath = strcat('C:\E', num2str(apitch), num2str(diam), 'e3D', num2str(index), '.txt');
63          E(:,index) = load(epath);
64      end
65
66      Numpts = 401;
67      xmin = min(kx);
68      xmax = max(kx);
69      ymin = min(ky);
70      ymax = max(ky);
71
72      xres = (xmax-xmin)/(Numpts-1);
73      yres = (ymax-ymin)/(Numpts-1);
74      xv = xmin:xres:xmax;
75      yv = ymin:yres:ymax;
76
77      for j=BandStart:1:BandStop
78          clear Einterp;
79          Einterp = gridfit(kx,ky,E(j,:),xv,yv);
80          savepath = strcat('C:\E', num2str(apitch),  num2str(diam), 'e3DInterp', num2str(j), '.mat');
81          save (savepath, 'Einterp');
82      end
```

ISBscatteringAcoustic.m

```
83      %ISBscatteringAcoustic.m
84      %Calculates the acoustic phonon scattering rate from a single
85      %k-point in some initial band into all k-points in the final band
86
87      clear all;
88      e = 1.6e-19;
89      e0 = 8.854e-12;
90      hbar = 1.054e-34;
91      kb = 1.38e-23;
92      D = 7.2;
93      cs = 3400;
94      rho = 5500;
95      %karray defines the number of each k point to calculate the
96      %scattering rate into in the final band
97      karray = [1,4,7,10,20,22,25,27,35,38,40,46,49,55];
98
99      kindex1 = 1;
100     kindex2 = 1;
101     bandindex1 = 2;
102     bandindex2 = 1;
103     NumK = size(karray,2);
104
105
106     delnm = 0;
107     a = 100;
108     b = 100;
109     q = 0.275;
110     T = 77;
111     gamma = a/b;
112     L = 8;
113     L = L/a;
114     kz = 1*pi/L/(2*pi);
115     kzprime = 1*pi/L/(2*pi);
116
117     eEpath1 = strcat('C:\E10010060e3D', num2str(kindex1), '.txt');
118     E = load(eEpath1);
119     E1 = E(bandindex1);
120     eEpath2 = strcat('C:\','E10010060e3D', num2str(kindex2), '.txt');
121     E = load(eEpath2);
122     E2 = E(bandindex2);
123
124     Eq = (E1-E2)*0.001*e;
125     nb = 1/(exp(Eq/(kb*T))-1);
126
127     alphasquared = (2*pi/hbar)*e^2*D^2/(2*rho*cs^2*(a*1e-9)^3*L)*(nb+1);
128
129     N = 9;
130     Ntot = N^2;
131
```

```
132   kxpath = strcat('C:\kx1.txt');
133   kypath = strcat('C:\ky1.txt');
134
135   kxarray = load(kxpath);
136   kyarray = load(kypath);
137
138   kn = kxarray(kindex1)/(2*pi);
139   km = kyarray(kindex1)/(2*pi);
140
141
142   eIXpath1 = strcat('C:\IX10010060e3D', num2str(kindex1), '.txt');
143   eVpath1 = strcat('C:\V10010060e3D', num2str(kindex1), '.mat');
144   eEpath1 = strcat('C:\E10010060e3D', num2str(kindex1), '.txt');
145
146   IX1 = load(eIXpath1);
147   V = load(eVpath1);
148   V1 = V.V;
149   Aj1 = V1(:,IX1(bandindex1));
150   E = load(eEpath1);
151   E1 = E(bandindex1);
152
153   %Compute reciprocal space vectors G
154   mid = (N+1)/2;
155   for p=1:N
156       for q=1:N
157           G((p+(q-1)*N),1) = (p-mid);
158           G((p+(q-1)*N),2) = (mid-q)*gamma;
159       end
160   end
161
162   lboundx = -0.5;
163   uboundx = 0.5;
164   lboundy = -0.5;
165   uboundy = 0.5;
166
167   stepx = 0.1;
168   stepy = 0.1;
169
170   Numptsxy = 401;
171
172   xres = (uboundx-lboundx)/(Numptsxy-1);
173   yres = (uboundy-lboundy)/(Numptsxy-1);
174   xv = lboundx:xres:uboundx;
175   yv = lboundy:yres:uboundy;
176   xyArea = xres*yres;
177
178   thetastep = pi/10;
179   phistep = pi/10;
180
181   lboundtheta = 0;
182   uboundtheta = pi;
183   lboundphi = 0;
184   uboundphi = 2*pi;
185
186   Numptsq = 401;
187
188   thetares = (uboundtheta-lboundtheta)/(Numptsq-1);
189   phires = (uboundphi-lboundphi)/(Numptsq-1);
190   thetav = lboundtheta:thetares:uboundtheta;
191   phiv = lboundphi:phires:uboundphi;
192   qArea = thetares*phires;
193
194   for kindex = 2:NumK
195   kindex2 = karray(kindex);
196
197   clear Integrand
198   clear xarray
199   clear yarray
200   clear Iinterp
201   clear qIntegrand
202   clear qnarray
203   clear qmarray
204   clear qnA
205   clear qmA
206
207
208   kmprime = kyarray(kindex2)/(2*pi);
209   knprime = kxarray(kindex2)/(2*pi);
210
211
212   eIXpath2 = strcat('C:\IX10010060e3D', num2str(kindex2), '.txt');
213   eVpath2 = strcat('C:\V10010060e3D', num2str(kindex2), '.mat');
214   eEpath2 = strcat('C:\E10010060e3D', num2str(kindex2), '.txt');
215
216   IX2 = load(eIXpath2);
217   V = load(eVpath2);
218   V2 = V.V;
219   E = load(eEpath2);
220   E2 = E(bandindex2);
221   Aj2 = V2(:,IX2(bandindex2));
222
223   q = (E1-E2)*.001*e*a*1e-9/(2*pi*hbar*cs);
224
225   qindex = 1;
226   for theta = lboundtheta:thetastep:uboundtheta
227       for phi = lboundphi:phistep:uboundphi
228
229       qn = q*sin(theta)*cos(phi);
230       qm = q*sin(theta)*sin(phi);
231       qz = q*cos(theta);
232
233       xyindex = 1;
234       for x=lboundx:stepx:uboundx
235           for y=lboundy:stepy:uboundy
236
237                 result = 0;
238                 for p = 1:Ntot
239                     for q = 1:Ntot
```

```
                        n = G(q,1);
                        m = G(q,2);
                        nprime = G(p,1);
                        mprime = G(p,2);

                        result = result + Aj2(p)'*Aj1(q)*exp(2*pi*i*(((kn-knprime)+(n-nprime)+qn)*x + ((km-kmprime)+(m-mprime)+qm)*y));
                    end
                end
                Integrand(xyindex) = result;
                xarray(xyindex) = x;
                yarray(xyindex) = y;
                xyindex = xyindex + 1;
            end
        end
        Gzsquared = (abs(0.5*(sin((qz+kzprime-kz)*L/2)/((qz+kzprime-kz)*L/2)*exp(i*(qz+kzprime-kz)*L/2)+sin((qz-kzprime+kz)*L/2)/((qz-kzprime+kz)*L/2)*exp(i*(qz-kzprime+kz)*L/2) ...
            -sin((qz+kzprime+kz)*L/2)/((qz+kzprime+kz)*L/2)*exp(i*(qz+kzprime+kz)*L/2)-sin((qz-kzprime-kz)*L/2)/((qz-kzprime-kz)*L/2)*exp(i*(qz-kzprime-kz)*L/2))))^2;

        Iinterp = gridfit(xarray,yarray,Integrand,xv,yv);

        qIntegrand(qindex) = Gzsquared*(abs(xyArea*sum(sum(Iinterp))))^2;
        thetaarray(qindex) = theta;
        phiarray(qindex) = phi;

        qIntegrand(qindex)

        qindex = qindex + 1;
        end
    end

    thetaA = cat(2,thetaarray,thetaarray);
    phiA = cat(2,phiarray,phiarray);
    qIntegrand = cat(2,qIntegrand,qIntegrand);

    qInterpPath = strcat('C:\qInterp', num2str(kindex1), '_', num2str(kindex2), '.mat');
    qIinterp = gridfit(thetaA,phiA,qIntegrand,thetav,phiv);
    save(qInterpPath, 'qIinterp');

    Answer(kindex) = qArea*sum(sum(qIinterp));
    kindex = kindex+1;
    end
    AnswerPath = strcat('C:\Answer.txt');
    save(AnswerPath, 'Answer', '-ASCII');
```

ISBscatteringLO.m

```
%ISBscatterinLO.m
%Calculates the intersubband LO phonon scattering rate

clear all;
e = 1.6e-19;
e0 = 8.854e-12;
hbar = 1.054e-34;
WL1 = 28.9;
WL2 = 33.6;
WT1 = 28.2;
WT2 = 31.9;
kb = 1.38e-23;

kindex1 = 1;
bandindex1 = 24;
bandindex2 = 2;

kptarray = [1,10,55];
NumKpts = size(kptarray,2);

delnm = 1;
a = 100;
b = 100;
q = 0.275;
T = 77;
gamma = a/b;
L = 8;
L = L/a;
kz = 1*pi/L/(2*pi);
kzprime = 1*pi/L/(2*pi);

epsiloninf = (12.3-1.4*(1-q))*e0;

c1 = (2*pi*e^2/epsiloninf)*(1-(WT1^2/WL1^2))*((WT2^2-WL1^2)/(WL2^2-WL1^2));
c2 = (2*pi*e^2/epsiloninf)*(1-(WT2^2/WL2^2))*((WL2^2-WT1^2)/(WL2^2-WL1^2));

Eq = 0.0289*e;
nb = 1/(exp(Eq/(kb*T))-1);

alpha1squared = (2*pi/hbar)*c1/((a*1e-9)^3*L)*(a*1e-9)^2*(nb+1);
alpha2squared = (2*pi/hbar)*c2/((a*1e-9)^3*L)*(a*1e-9)^2*(nb+1);

N = 9;
Ntot = N^2;

kxpath = strcat('C:\kx1.txt');
kypath = strcat('C:\ky1.txt');

kxarray = load(kxpath);
kyarray = load(kypath);

kn = kxarray(kindex1)/(2*pi);
km = kyarray(kindex1)/(2*pi);


eIXpath1 = strcat('C:\IX10010060e3D', num2str(kindex1), '.txt');
```

```
339   eVpath1 = strcat('C:\V10010060e3D', num2str(kindex1), '.mat');
340
341   IX1 = load(eIXpath1);
342   V = load(eVpath1);
343   V1 = V.V;
344
345   Aj1 = V1(:,IX1(bandindex1));
346
347   %Compute reciprocal space vectors G
348   mid = (N+1)/2;
349   for p=1:N
350       for q=1:N
351           G((p+(q-1)*N),1) = (p-mid);
352           G((p+(q-1)*N),2) = (mid-q)*gamma;
353       end
354   end
355
356   lboundx = -0.5;
357   uboundx = 0.5;
358   lboundy = -0.5;
359   uboundy = 0.5;
360
361   stepx = 0.05;
362   stepy = 0.05;
363
364   Numptsxy = 401;
365
366   xres = (uboundx-lboundx)/(Numptsxy-1);
367   yres = (uboundy-lboundy)/(Numptsxy-1);
368   xv = lboundx:xres:uboundx;
369   yv = lboundy:yres:uboundy;
370   xyArea = xres*yres;
371
372   qnstep = 0.25;
373   qmstep = 0.25;
374
375   lboundqn = 0;
376   uboundqn = 6;
377   lboundqm = 0;
378   uboundqm = 6;
379
380   Numptsq = 401;
381
382   qnres = (uboundqn-lboundqn)/(Numptsq-1);
383   qmres = (uboundqm-lboundqm)/(Numptsq-1);
384   qnv = lboundqn:qnres:uboundqn;
385   qmv = lboundqm:qmres:uboundqm;
386   qArea = qnres*qmres;
387
388   for kindex2 = 1:NumKpts
389   kindex = kptarray(kindex2);
390
391   knprime = kxarray(kindex)/(2*pi);
392   kmprime = kyarray(kindex)/(2*pi);
393
394   clear Integrand
395   clear xarray
396   clear yarray
397   clear Iinterp
398   clear qIntegrand
399   clear qnarray
400   clear qmarray
401   clear qnA
402   clear qmA
403   clear Aj2
404   clear IX2
405   clear V2
406   clear V
407
408   eIXpath2 = strcat('C:\IX10010060e3D', num2str(kindex), '.txt');
409   eVpath2 = strcat('C:\V10010060e3D', num2str(kindex), '.mat');
410
411   IX2 = load(eIXpath2);
412   V = load(eVpath2);
413   V2 = V.V;
414
415   Aj2 = V2(:,IX2(bandindex2));
416
417   qindex = 1;
418   for qn = lboundqn:qnstep:uboundqn
419       for qm = qn:qmstep:uboundqm
420
421       if (qn==0 && qm==0)
422
423           qIntegrand(qindex) = (abs(Aj2'*Aj1))^2;
424           qnarray(qindex) = qn;
425           qmarray(qindex) = qm;
426           qindex = qindex+1;
427       else
428
429       xyindex = 1;
430       for x=lboundx:stepx:uboundx
431           for y=lboundy:stepy:uboundy
432
433                 result = 0;
434                 for p = 1:Ntot
435                     for q = 1:Ntot
436
437                         n = G(q,1);
438                         m = G(q,2);
439                         nprime = G(p,1);
440                         mprime = G(p,2);
441
442                         result = result + Aj2(p)'*Aj1(q)*exp(2*pi*i*(((kn-knprime)+(n-nprime)+qn)*x + ((km-
      kmprime)+(m-mprime)+qm)*y));
443                     end
444                 end
445                 Integrand(xyindex) = result;
```

```
446                 xarray(xyindex) = x;
447                 yarray(xyindex) = y;
448                 xyindex = xyindex + 1;
449             end
450         end
451         qsquared = qn^2+qm^2;
452         q = sqrt(qsquared);
453         Term = 0.5*((1+delnm)/(q^2+(kzprime-kz)^2)+1/(q^2+(kzprime+kz)^2)-2*q/L*(1-exp(-q*L)*cos((kzprime-kz)*L))*
    ...
454          (1/(q^2+(kzprime-kz)^2)-1/(q^2+(kzprime+kz)^2))^2);
455         Integrand = Integrand.*Term;
456
457         Iinterp = gridfit(xarray,yarray,Integrand,xv,yv);
458
459         qIntegrand(qindex) = (abs(xyArea*sum(sum(Iinterp))))^2;
460         qnarray(qindex) = qn;
461         qmarray(qindex) = qm;
462
463         qindex = qindex + 1;
464         end
465         end
466     end
467
468     qnA = cat(2,qnarray,qmarray);
469     qmA = cat(2,qmarray,qnarray);
470     qIntegrand = cat(2,qIntegrand,qIntegrand);
471     qIntegrand = qIntegrand*alpha1squared;
472     qIntegrandPath = strcat('C:\qIntegrand', num2str(bandindex1), '_', num2str(bandindex2), '_', num2str(kindex),
    '.mat');
473     save(qIntegrandPath, 'qIntegrand');
474
475     qInterpPath = strcat('C:\qInterp', num2str(bandindex1), '_', num2str(bandindex2), '_', num2str(kindex), '.mat');
476     qIinterp = gridfit(qnA,qmA,qIntegrand,qnv,qmv);
477     save(qInterpPath, 'qIinterp');
478     % surf(qnv,qmv,qIinterp, 'LineStyle', 'none');
479     Answer(kindex2) = 4*qArea*sum(sum(qIinterp));
480     end
481     AnswerPath = strcat('C:\Answer_', num2str(bandindex1), '_', num2str(bandindex2), '_', num2str(kindex), '.txt');
482     save(AnswerPath, 'Answer', '-ASCII');
```

REFERENCES

[1] D. Bimberg, N. Kirstaedter, N. N. Ledentsov, Z. I. Alferov, P. S. Kop'ev, and V. M. Ustinov, IEEE Journal on Selected Topics in Quantum Electronics **3**, 196 (1997).

[2] V. C. Elarde, Ph.D. dissertation, University of Illinois at Urbana-Champaign, 2007.

[3] D. Leonard, M. Krishnamurthy, C. M. Reaves, S. P. DenBaars, and P. M. Petroff, Appl. Phys. Lett. **63**, 3203 (1993).

[4] D. Bimberg, in QUEST Workshop on Quantum Structures, Colloquium Abstracts, Santa Barbara, CA, 1994, p.15.

[5] A. Madhukar, Q. Xie, P. Chen, and A. Konkar, Appl. Phys. Lett. **64**, 2727 (1994).

[6] J. M. Moison, F. Houzay, F. Barthe, L. Leprince, E. Andre, and O. Vatel, Appl. Phys. Lett. **64**, 196 (1994).

[7] F. Heinrichsdorff, A. Krost, M. Grundmann, R. Heitz, D. Bimberg, A. Kosogov, P. Werner, F. Bertram, and J. Christen, in *Proceedings of 23rd International Conference on the Physics of Semiconductors*, Berlin, Germany, 1996, edited by M. Scheffler and R. Zimmermann, World Scientific, Singapore, vol. 2, p. 1321.

[8] K. Mukai, N. Ohtsuka, M. Sugawara, and S. Yamazaki, Jpn. J. Appl. Phys. **33**, L1710 (1994).

[9] J. Oshinowo, M. Nishioka, S. Ishida, and Y. Arakawa, Appl. Phys. Lett. **65**, 1421 (1994).

[10] N. N. Ledentsov, J. Bohrer, D. Bimberg, I. V. Kochnev, M. V. Maximov, P. S. Kop'ev, Z. I. Alferov, A. O. Kosogov, S. S. Ruvimov, P. Werner, and U. Gosele, Appl. Phys. Lett. **69**, 1095 (1996).

[11] M. Geiger, A. Bauknecht, F. Adler, H. Schweizer, and F. Scholz, J. Crystal Growth **170**, 558 (1997).

[12] E. C. Le Ru, P. Howe, T. S. Jones, and R. Murray, Phys. Rev. B **67**, 165303 (2003).

[13] M. J. da Silva, A. A. Quivy, S. Martini, T. E. Lamas, E. C. F. da Silva, and J. R. Leite, Appl. Phys. Lett. **82**, 2646 (2003).

[14] X. D. Wang, Z. C. Niu, S. L. Feng, Z. H. Miao, Chin. Phys. Lett. **18**, 608 (2001).

[15] Y. Q. Wei, S. M. Wang, F. Ferdos, J. Vukusic, Q. X. Zhao, M. Sadeghi, and A. Larsson, J. Cryst. Growth **251**, 172 (2003).

[16] Y. Nagamune, M. Nishioka, S. Tsukamoto, and Y. Arakawa, Appl. Phys. Lett. **64,** 2495 (1994).

[17] S. C. Lee, A. Stintz, and S. R. J. Brueck, J. Appl. Phys. **91**, 3282 (2002).

[18] T. S. Yeoh, C. P. Liu, R. B. Swint, A. E. Huber, S. D. Roh, C. Y. Woo, K. E. Lee, and J. J. Coleman, Appl. Phys. Lett. **79**, 221 (2001).

[19] T. S. Yeoh, R. B. Swint, A. Gaur, V. C. Elarde, and J. J. Coleman, IEEE Journal on Selected Topics in Quantum Electronics **8**, 833 (2002).

[20] S. Watanabe, E. Pelucchi, B. Dwir, M. H. Baier, K. Leifer, and E. Kapon, Appl. Phys. Lett. **84**, 2907 (2004).

[21] C.-K. Hahn, J. Motohisa, and T. Fukui, J. Crystal Growth **221**, 599 (2000).

[22] C.-K. Hahn, J. Motohisa, and T. Fukui, Appl. Phys. Lett. **76**, 3947 (2000).

[23] T. Ishikawa, S. Kohmoto, and K. Asakawa, Appl. Phys. Lett. **73**, 1712 (1998).

[24] T. Ishikawa, T. Nishimura, S. Kohmoto, and K. Asakawa, Appl. Phys. Lett. **76**, 167 (2000).

[25] A. Scherer and H. G. Craighead, Appl. Phys. Lett. **49**, 1284 (1986).

[26] E. M. Clausen, Jr., H. G. Craighead, J. M. Worlock, J. P. Harbison, L. M. Schiavone, L. Florez, and B. Van der Gaag, Appl. Phys. Lett. **55**, 1427 (1989).

[27] A. Forchel, H. Leier, B. E. Maile, and R. Germann, Advances in Solid State Physics **28**, 99 (1988).

[28] P. M. Petroff, A. C. Gossard, R. A. Logan, and W. Wiegmann, Appl. Phys. Lett. **41**, 635 (1982).

[29] A. Forchel, R. Steffen, T. Koch, M. Michel, M. Albrecht, and T. L. Reinecke, Semicond. Sci. Technol. **11**, 1529 (1996).

[30] R. Steffen, Th. Koch, J. Oshinowo, F. Faller, and A. Forchel, Appl. Phys. Lett. **68**, 223 (1996).

[31] V. C. Elarde, R. Rangarajan, J. J. Borchardt, and J. J. Coleman, IEEE Photon. Technol. Lett. **17**, 935 (2005).

[32] V. B. Verma, U. Reddy, N. L. Dias, K. P. Bassett, X. Li, and J. J. Coleman, Journal of Quantum Electronics (submitted).

[33] J. J. Coleman, R. B. Swint, T. S. Yeoh, and V. C. Elarde, presented at *Optoelectronic and Microelectronic Materials and Devices,* Sydney, Australia, 2002, pp. 241-246.

[34] R. B. Swint, A. E. Huber, T. S. Yeoh, C. Y. Woo, J. J. Coleman, B. O. Faircloth, and M. S. Zediker, IEEE Photonics Technology Letters **14**, 441-443 (2002).

[35] R. B. Swint, V. C. Elarde, S. Raychaudhuri, and J. J. Coleman, Electronics Letters **38**, 794-795 (2002).

[36] T. Van Caenegem, D. Van Thourhout, M. Galarza, S. Verstuyft, I. Moerman, P. Van Daele, R. Baets, P. Demeester, C. G. P. Herben, X. J. M. Leijten, and M. K. Smit, Electronics Letters **37,** 296-298 (2001).

[37] R. B. Swint, J. J. Coleman, B. O. Faircloth, and M. S. Zediker, presented at *The 14th Annual Meeting of the Lasers and Electro-Optics Society*, San Diego, CA, 2001, pp. 879-880.

[38] V.C. Elarde and J.J. Coleman, IEEE Photonics Technology Lett. **20**, 240 (2008).

[39] J. Lee, W.-C. Chou, C.-S. Yang, and G. J. Jan, Chinese J. Phys. **42**, 102 (2004).

[40] J. R. Downes, D. A. Faux, and E. P. O'Reilly, J. Appl. Phys. **81**, 6700 (1997).

[41] V. B. Verma, M.S. thesis, University of Illinois at Urbana-Champaign, 2005.

[42] S. Sanguinetti, M. Padovani, M. Fuioli, E. Grilli, M. Guzzi, A. Vinattieri, M. Colocci, P. Frigeri, S. Fanchi, L. Lazzarini, and G. Salviati, Thin Solid Films **380**, 224 (2000).

[43] H. S. Kim, J. H. Suh, C. G. Park, S. J. Lee, S. K. Noh, J. D. Song, Y. J. Park, W. J. Choi, and J. I. Lee, Journal of Crystal Growth **311**, 258 (2009).

[44] T. Benabbas, Y. Androussi, and A. Lefebvre, J. Appl. Phys. **86**, 1945 (1999).

[45] K. C. Wijesundara, M. Garrido, S. Ramanathan, E. A. Stinaff, M. Scheibner, A. S. Bracker, and D. Gammon, Mater. Res. Soc. Symp. Proc. **1117** (2009).

[46] E. A. Stinaff, M. Scheibner, A. S. Bracker, I. V. Ponomarev, V. L. Korenev, M. E. Ware, M. F. Doty, T. L. Reinecke, and D. Gammon, Science, **311**, 636 (2006).

[47] G. D. Sanders, K. W. Kim, and W. C. Holton, Phys. Rev. B **61**, 11 (2000).

[48] V. C. Elarde and J. J. Coleman, Physica Status Solidi (c) **3**, 508-511 (2006).

[49] V. C. Elarde, A. C. Bryce, and J. J. Coleman, Electronics Letters **41**, 1122-1124 (2005).

[50] V. C. Elarde, T. S. Yeoh, R. Rangarajan, and J. J. Coleman, Journal of Crystal Growth **272,** 148 (2004).

[51] Y. Arakawa and H. Sakaki, Appl. Phys. Lett. **40**, 939 (1982).

[52] O. B. Shchekin, P. Gyoungwon, D. L. Huffaker, and D. G. Deppe, Applied Physics Letters **77,** 466 (2000).

[53] P. Blood, IEEE Journal of Quantum Electronics **36**, 354 (2000).

[54] L. V. Asryan and R. A. Suris, Semiconductors **38**, 3-25 (2004).

[55] M. Asada, Y. Miyamoto, and Y. Suematsu*,* IEEE J. Quantum Electron*.* **22**, 1915 (1986).

[56] K. J. Vahala, IEEE J. Quantum Electron*.* **24**, 523 (1988).

[57] Y. Miyamoto, Y. Miyake, M. Asada, and Y. Suematsu, IEEE J. Quantum Electron. **25**, 2001 (1989).

[58] O. Stier, M. Grundmann, and D. Bimberg, Phys. Rev. B **59**, 5688-5701 (1999).

[59] J. Lee, W. Chou, C. Yang, and G. J. Jan, Chinese Journal of Physics **42**, 102-115 (2004).

[60] F. E. Prins, S. Yu. Nikitin, G. Lehr, and H. Schweizer, Phys. Rev. B **49,** 8109-8112 (1994).

[61] D. El-Moghraby, R. G. Johnson, and P. Harrison, Computer Physics Communications **150**, 235-246 (2003).

[62] Y. Li, O. Voskoboynikov, C. P. Lee, and S. M. Sze, Computer Physics Communications **141**, 66-72 (2001).

[63] S. Shi, C. Chen, and D. W. Prather, J. Opt. Soc. Am. A **21**, 1769-1775 (2004).

[64] M. Plihal and A. A. Maradudin, Phys. Rev. B **44**, 8565-8571 (1991).

[65] P. R. Villeneuve and M. Piché, Phys. Rev. B **46**, 4969-4972 (1992).

[66] R. D. Meade, K. D. Brommer, A. M. Rappe, and J. D. Joannopoulos, Appl. Phys. Lett. **61**, 495-497 (1992).

[67] K. M. Ho, C. T. Chan, and C. M. Soukoulis, Phys. Rev. Lett. **65**, 3152-3155 (1990).

[68] S. G. Johnson and J. D. Joannopoulos, Optics Express **8,** 173-190 (2001).

[69] S. L. Chuang, *Physics of Optoelectronic Devices* (John Wiley and Sons, Inc., New York, 1995).

[70] R. Ferreira and G. Bastard, Phys. Rev. B **40**, 1074 (1989).

[71] A. Seilmeier, H. J. Hubner, G. Abstreiter, G. Weimann, and W. Schlapp, Phys. Rev. Lett. **59**, 1345 (1987).

[72] S. I. Borenstain and J. Katz, Appl. Phys. Lett. **55**, 654-656 (1989).

[73] Q. Hu and S. Feng, Appl. Phys. Lett. **59**, 2923-2925 (1991).

[74] R. Köhler et al., Nature **417**, 156-159 (2002).

[75] M. Rochat et al., Appl. Phys. Lett. **81**, 1381-1383 (2002).

[76] B. S. Williams, H. Callebaut, S. Kumar, Q. Hu, and J. L. Reno, Appl. Phys. Lett. **82**, 1015-1017 (2003).

[77] P. C. Sercel and K. J. Vahala, Phys. Rev. B **44**, 5681-5691 (1991).

[78] B. F. Levine, J. Appl. Phys. **74**, R1 (1993).

[79] E. Costard, J. P. Truffer, O. Huet, L. Dua, A. Nedeleu, J. A. Robo, X. Mareadet, N. B. De l'Isle, and P. Bois, Proc. SPIE **6361**, p. 636117 (2006).

[80] J. Phillips, J. Appl. Phys. **91**, 4590 (2002).

[81] J. Campbell and A. Madhukar, Proc. IEEE **95**, 1815 (2007).

[82] V. Ryzhii, Semicond. Sci. Technol. **11**, 759 (1996).

[83] D. Pan, E. Towe, and S. Kennerly, Appl. Phys. Lett. **73**, 1937 (1998).

[84] A. Weber, O. Gauthier-Lafaye, F. H. Julien, J. Brault, M. Gendry, Y. Desieres, and T. Benyattou, Appl. Phys. Lett. **74**, 413 (1999).

[85] L. Chu, A. Zrenner, G. Böhm, and G. Abstreiter, Appl. Phys. Lett. **75**, 3599 (1999).

[86] P. Vines, C. H. Tan, J. P. R. David, R. S. Attaluri, T. E. Vandervelde, and S. Krishna, Proc. SPIE **7113**, 71130J (2008).

[87] H. Friedrich, *Theoretical Atomic Physics* (Springer-Verlag, Berlin, 1990), p. 111.

[88] V. B. Verma, V. C. Elarde, and J. J. Coleman, IEEE J. Quantum Electron. **45**, 10 (2009).

[89] F. M. Peeters, A. Matulis, M. Helm, T. Fromherz, and W. Hilber, Phys. Rev. B **48**, 12008 (1993).

[90] C. J. Chen, K. K. Choi, L. Rokhinson, W. H. Chang, and D. C. Tsui, Appl. Phys. Lett. **74**, 862 (1999).

[91] J. J. Coleman, R. M. Lammert, M. L. Osowski, and A.M. Jones, IEEE J. Sel. Top. in Quantum Elec. **3**, 874-884 (1997).

[92] K. Yamaguchi, M. Ogasawara, and K. Okamoto, J. Appl. Phys. **72**, 5919-5925 (1991).

[93] R. Bhat, J. Crystal Growth **120**, 362-368 (1992).

[94] O. Kayser, J. Cryst. Growth **107**, 989-998 (1991).

[95] K. Yamaguchi, M. Ogasawara, and K. Okamoto, J. Appl. Phys. **72**, 5919-5925 (1991).

[96] K. Yamaguchi and K. Okamoto, Jpn. J. Appl. Phys. **32,** 1523-1527 (1993).

[97] C. Caneau, R. Bhat, M. R. Frei, C. C. Chang, R. J. Deri, and M. A. Koza, J. Cryst. Growth **124**, 243-248 (1992).

[98] J. Finders, J. Geurts, A. Kohl, M. Weyers, B. Opitz, O. Kayser, and P. Balk, J. Cryst. Growth **107**, 151-155 (1991).

[99] J. W. Mathews and A. E. Blakeslee, J. Cryst. Growth **27**, 118-125 (1974).